The Pennsylvania State University
The Graduate School
College of Earth and Mineral Sciences

EVALUATION OF A DUAL-FREQUENCY RADAR CLOUD LIQUID WATER CONTENT RETRIEVAL ALGORITHM

A Thesis in
Meteorology
by
Courtney D. Laughlin

© 2014 Courtney D. Laughlin

Submitted in Partial Fulfillment
of the Requirements
for the Degree of

Master of Science

August 2014

The thesis of Courtney D. Laughlin was reviewed and approved* by the following:

Eugene E. Clothiaux
Professor of Meteorology
Thesis Advisor

Johannes Verlinde
Professor of Meteorology
Associate Head of the Department of Meteorology Graduate Program

Kültegin Aydin
Professor of Electrical Engineering
Head of the Department of Electrical Engineering

*Signatures are on file in the Graduate School.

Abstract

Cloud microphysical properties, including liquid water content, greatly impact the Earth's radiation budget but have high uncertainties in global climate models. Although today's three-channel microwave radiometers provide the most trusted liquid water path retrievals, reliable liquid water content retrievals are not yet available. New efforts to improve the retrieval of cloud liquid water contents are underway. One such effort that retrieves cloud liquid water content using a dual-frequency radar differential absorption approach with total variation regularization techniques is evaluated here.

One benefit of this method is that it only depends on differences in attenuation between the two frequency radars so there is no need for the radars to be calibrated. Differences in attenuation are proportional to the path-integrated liquid in the cloud and, therefore, can be used to retrieve liquid water contents at every height inside a cloud. This method is unreliable when ice particles or large drops with maximum dimensions greater than one third of the W-band wavelength of approximately 3 mm are present because the attenuation can appear to increase due to resonant scattering and not by absorption. Therefore, we limit the test cases in this study to low-level clouds consisting of only liquid water drops with diameters less than one third of the W-band wavelength.

Using 65 test cases obtained from four different Department of Energy Atmospheric Radiation Measurement Climate Program Research Facilities, we were able to reproduce the results of an earlier study based on a single case study period in which the radar-retrieved cloud liquid water paths fall within ± 0.3 mm of those retrieved from microwave radiometer measurements. The standard deviation of the differences between the radar- and microwave radiometer-retrieved cloud liquid water paths was 0.12 mm once outliers were removed. Analyzing the differences of the radar- and microwave radiometer-retrieved cloud liquid water paths as a function of the microwave radiometer-retrieved cloud liquid water paths, we found

that the standard deviation of 0.12 mm was relatively constant for differences partitioned by microwave radiometer-retrieved cloud liquid water path. This implies that relative errors in radar-retrieved cloud liquid water paths were much larger for small values than for large ones. As a result, these retrievals are not sufficient for radiation studies in low liquid water path clouds but may be sufficient for some studies of clouds with large cloud liquid water paths.

We found that radar-retrieved cloud liquid water contents were sensitive to the a priori profiles of cloud liquid water content used to initialize the retrieval. Several unphysical features in the radar-retrieved cloud liquid water content fields can be attributed to these a priori estimates and methods for removing them are discussed. Finally, this retrieval approach highlights the deleterious effects of errors in beam pointing. Improving the pointing accuracy of the W- and Ka-band radars would lead to the greatest improvements in the accuracy of the radar-retrieved cloud liquid water contents.

Contents

List of Figures **vii**

List of Tables **xi**

Chapter 1 Introduction and Motivation **1**
1.1 Methods of Retrieving Cloud LWP 2
1.2 Methods of Retrieving Cloud LWC 3

Chapter 2 Methodology **6**
2.1 Dual-frequency Radar Cloud LWC Retrieval Algorithm 6
2.1.1 Implementation of Total Variation Regularization Technique 9
2.2 Assessment of Dual-frequency Radar LWC Retrievals 11
2.2.1 Comparison of Dual-frequency Radar-Retrieved LWPs to MWR-retrieved LWPs 11
2.2.2 Implementation of Temporal Averaging and Spatial Filtering 12

Chapter 3 Instruments and Observational Data **14**
3.1 Instruments and Data for Dual-frequency Radar Retrieval 14
3.2 Instruments and Data for Assessment of Dual-frequency Radar Retrieval 15
3.3 Case Study Periods 16

Chapter 4 Results **21**
4.1 Nine Four-hour Case Study Periods 22
4.2 Comparison of Dual-frequency Radar-retrieved LWP to MWR-retrieved LWP 22
4.3 Impact of Temporal Resolution and Spatial Filtering 28

Chapter 5 Discussion and Conclusions **36**
5.1 Dual-frequency Radar Cloud LWC Retrieval Algorithm Performance 37
5.2 Sources of Error in the Dual-frequency Radar Cloud LWC Retrieval Algorithm 48

Chapter 6 Summary and Future Work **51**

Appendix A Figures **55**

Bibliography **86**

List of Figures

1.1 A geographical depiction of the locations of each ACRF used in this study. 5

4.1 TCAP (a, c) KASACR and (b, d) WSACR height versus time reflectivities from (a, b) 13:00-17:00 UTC on 4 September 2012 and (c, d) 15:00-19:00 UTC on 14 November 2012. The black and red dotted lines are the first cloud base height and the second cloud base height, respectively, retrieved from Vaisala ceilometer measurements. 23

4.2 SGP (a, c, e) KASACR and (b, d, f) WSACR height versus time reflectivities from (a, b) 13:00-17:00 UTC on 5 October 2012, (c, d) 13:00-17:00 UTC on 2 April 2013, and (e, f) 15:00-19:00 UTC on 18 April 2013. The black and red dotted lines are the first cloud base height and the second cloud base height, respectively, retrieved from Vaisala ceilometer measurements. 24

4.3 NSA (a, c) KASACR and (b, d) WSACR height versus time reflectivities from (a, b) 16:00-20:00 UTC on 25 July 2012 and (c, d) 16:00-20:00 UTC on 18 October 2012. The black and red dotted lines are the first cloud base height and the second cloud base height, respectively, retrieved from Vaisala ceilometer measurements. 25

4.4 MAGIC (a, c) KAZR and (b, d) MWACR height versus time reflectivities from (a, b) 14:00-18:00 UTC on 26 November 2012 and (c, d) 14:00-18:00 UTC on 8 July 2013. The black and red dotted lines are the first cloud base height and the second cloud base height, respectively, retrieved from Vaisala ceilometer measurements. 26

4.5 Frequency of occurrence LWP differences for all 10-s averaged data in Tables 3.1 and 3.2. 27

4.6 Frequency of occurrence LWP differences for all case 10-s averaged data in Table 3.3. 28

4.7 Frequency of occurrence histograms of radar- and MWR-retrieved LWP differences versus MWR-retrieved LWPs for the 0.4 s temporal resolution data for (a) all of the case data in Tables 3.1 and 3.2 and (b) the nine case study periods in Table 3.3. 30
4.8 Same as Fig. 4.7 but for the 2.5 s temporal resolution data. 30
4.9 Same as Fig. 4.7 but for the 5.0 s temporal resolution data. 31
4.10 Same as Fig. 4.7 but for the 10.0 s temporal resolution data. 31
4.11 Same as Fig. 4.7 but for the 20.0 s temporal resolution data. 32
4.12 Same as Fig. 4.7 but for the 60.0 s temporal resolution data. 32
4.13 Frequency of occurrence histograms of radar-retrieved LWPs with spatial filtering versus those without filtering for time resolutions of (a) 0.4 s, (b) 2.5 s, (c) 5.0 s, (d) 10.0 s, (e) 20.0 s, and (f) 60.0 s. 33
4.14 Same as Fig. A.1 but for the MAGIC period from 14:00-18:00 UTC on 26 November 2012. The black dotted line is the first cloud base height and the red dotted line is the second cloud base height retrieved from Vaisala ceilometer measurements. 34
4.15 Same as Fig. A.1 but for the MAGIC period from 14:00-18:00 UTC on 26 November 2012 with the application of spatial filtering to DFR data. The black and red dotted lines are the first cloud base height and the second cloud base height, respectively, retrieved from Vaisala ceilometer measurements. 35

5.1 (a) LWC profiles from 16:00-16:10 UTC on 26 November 2012 during MAGIC using 10-s time resolution. (b) Radar- and MWR-retrieved LWPs for the same time period as in (a). 38
5.2 Retrieved LWP (in blue) and the beam angle offset of the KAZR from vertical (in green) with each data point plotted in black for the MAGIC case from 14:13-14:14 UTC on 26 November 2012. . . 40
5.3 Same as Fig. 5.2 but from 14:37-14:38 UTC on 26 November 2012. 40
5.4 The observed b (blue lines), the filtered vector df (green lines), the first-guess LWC profiles x_{b} (black lines), and the retrieved LWCs (red lines) for each 10-s profile from 16:01-16:02 UTC on 26 November 2012 during MAGIC. Note that x_{b} and LWC are expressed in g m^{-3} whereas b and df are expressed in arbitrary units and must be multiplied by $1000/2[\Delta h(\kappa_{95} - \kappa_{35})]$, or approximately 5.21, to convert them to g m^{-3}. 41
5.5 Same as Fig. 5.4 but from 15:30-15:31 UTC on 26 November 2012 during MAGIC. 43
5.6 Same as Fig. 5.4 but from 15:30-15:31 UTC on 26 November 2012 during MAGIC and for a-c) the 20-s data and d) the 60-s data. . . 44

5.7 (a) Means of the first guess LWC profiles x_b and (b) the radar-retrieved LWPs versus temporal resolution for the original (blue) and spatially filtered (green) DFR data from 15:25-15:35 UTC on 26 November 2012 during MAGIC. 45
5.8 Same as Fig. 5.4 but from 16:02-16:03 UTC on 26 November 2012 during MAGIC. 46
5.9 Same as Fig. 5.6 but from 16:02-16:03 UTC on 26 November 2012 during MAGIC. 47
5.10 Same as Fig. 5.7 but from 16:00-16:10 UTC on 26 November 2012 during MAGIC. 49

A.1 TCAP LWC fields for the case study period from 13:00-17:00 UTC on 4 September 2012.The black and red lines are the MWR-retrieved LWPs and radar-retrieved LWPS, respectively. 56
A.2 TCAP time series of radar- and MWR-retrieved LWPs for the case study period from 13:00-17:00 UTC on 4 September 2012. 57
A.3 TCAP histogram of differences between the radar- and MWR-retrieved LWPs for the case study period from 13:00-17:00 UTC on 4 September 2012. 58
A.4 Same as Fig. A.1 but for the TCAP period from 15:00-19:00 UTC on 14 November 2012. 59
A.5 Same as Fig. A.2 but for the TCAP period from 15:00-19:00 UTC on 14 November 2012. 60
A.6 Same as Fig. A.3 but for the TCAP period from 15:00-19:00 UTC on 14 November 2012. 61
A.7 Same as Fig. A.1 but for the SGP period from 13:00-17:00 UTC on 5 October 2012. 62
A.8 Same as Fig. A.2 but for the SGP period from 13:00-17:00 UTC on 5 October 2012. 63
A.9 Same as Fig. A.3 but for the SGP period from 13:00-17:00 UTC on 5 October 2012. 64
A.10 Same as Fig. A.1 but for the SGP period from 13:00-17:00 UTC on 2 April 2013. 65
A.11 Same as Fig. A.2 but for the SGP period from 13:00-17:00 UTC on 2 April 2013. 66
A.12 Same as Fig. A.3 but for the SGP period from 13:00-17:00 UTC on 2 April 2013. 67
A.13 Same as Fig. A.1 but for the SGP period from 15:00-19:00 UTC on 18 April 2013. 68

A.14 Same as Fig. A.2 but for the SGP period from 15:00-19:00 UTC on 18 April 2013. 69
A.15 Same as Fig. A.3 but for the SGP period from 15:00-19:00 UTC on 18 April 2013. 70
A.16 Same as Fig. A.1 but for the NSA period from 16:00-20:00 UTC on 25 July 2012. 71
A.17 Same as Fig. A.2 but for the NSA period from 16:00-20:00 UTC on 25 July 2012. 72
A.18 Same as Fig. A.3 but for the NSA period from 16:00-20:00 UTC on 25 July 2012. 73
A.19 Same as Fig. A.1 but for the NSA period from 16:00-20:00 UTC on 18 October 2012. 74
A.20 Same as Fig. A.2 but for the NSA period from 16:00-20:00 UTC on 18 October 2012. 75
A.21 Same as Fig. A.3 but for the NSA period from 16:00-20:00 UTC on 18 October 2012. 76
A.22 Same as Fig. A.1 but for the MAGIC period from 14:00-18:00 UTC on 26 November 2012. 77
A.23 Same as Fig. A.2 but for the MAGIC period from 14:00-18:00 UTC on 26 November 2012. 78
A.24 Same as Fig. A.3 but for the MAGIC period from 14:00-18:00 UTC on 26 November 2012. 79
A.25 Same as Fig. A.1 but for the MAGIC period from 14:00-18:00 UTC on 8 July 2013. 80
A.26 Same as Fig. A.2 but for the MAGIC period from 14:00-18:00 UTC on 8 July 2013. 81
A.27 Same as Fig. A.3 but for the MAGIC period from 14:00-18:00 UTC on 8 July 2013. 82
A.28 Same as Fig. A.1 but for the MAGIC period from 14:00-18:00 UTC on 26 November 2012 with the application of spatial filtering to DFR data. 83
A.29 Same as Fig. A.2 but for the MAGIC period from 14:00-18:00 UTC on 26 November 2012 with the application of spatial filtering to DFR data. 84
A.30 Same as Fig. A.3 but for the MAGIC period from 14:00-18:00 UTC on 26 November 2012 with the application of spatial filtering to DFR data. 85

List of Tables

3.1 Listing of the 65 hours of available W- and Ka-band radar data during periods of predominately liquid water clouds only. Each period is listed by site, date, time, the Ka-band radar, the W-band radar, the MWR, and the time of the SONDE data used in the radar retrieval. 18
3.2 Table 2.1 continued. 19
3.3 Same as Tables 2.1-2.2, but for the nine case study periods selected for detailed analyses of the performance of the dual-frequency radar retrieval algorithm. 20

Chapter 1

Introduction and Motivation

Of the numerous physical processes involved in Earths climate, those related to clouds have some of the largest impacts on it. Because many of these cloud-related physical processes are not well understood, their impacts on future climate are uncertain (IPCC, 2013). In order to properly characterize the impacts of clouds on global climate, the quantification of cloud microphysical and cloud radiative properties is required (Turner et al., 2007). In this study, we focus on retrieving two key cloud-microphysical properties: cloud liquid water content (LWC) and cloud liquid water path (LWP).

Cloud LWC (units of g m^{-3}) is defined as the sum of the masses of all cloud liquid water drops per unit volume. Cloud LWP (units of g m^{-2}) is defined as the sum of LWCs over the depth of cloud in a vertical column multiplied by the cross sectional area of the column. LWP provides a measure of the total amount of liquid water through the entire depth of a cloud.

In situ measurements of cloud drop size distributions and cloud LWCs are available through airborne instrumentation. However, aircraft measurements are expensive, not practical in terms of long-term observations required for cloud and climate studies, and difficult to obtain in a vertical column over a short period of time. Ground- and satellite-based remote sensing instrumentation can provide a long-term record of these quantities using a variety of techniques. However, existing techniques do not provide sufficiently accurate retrievals of LWC at temporal and

spatial resolutions required for the study of cloud and radiation interactions.

1.1 Methods of Retrieving Cloud LWP

The United States (US) Department of Energy (DOE) Atmospheric Radiation Measurement (ARM) Program Climate Research Facility (ACRF) currently operates a network of ground-based two-channel microwave radiometers (MWRs) specifically designed to provide reliable, calibrated radiometric data and achieve high accuracy retrievals of cloud LWP and precipitable water vapor with well-characterized uncertainties (Cadeddu et al., 2013). MWR data from the ACRF and retrievals using these data have now been publicly available to the scientific community for about 20 years. These data are commonly used in the science community because they cover a wide range of cloud LWPs and they do not require any knowledge of cloud drop size.

Over the past decade, an alternative method for characterizing cloud LWP that uses a combination of microwave radiometry and infrared interferometry has been developed (Liljegren et al., 2001, Turner, 2007). These studies led to improvements in the accuracies of cloud LWP retrievals and pointed to additional measurements necessary for further improvement, thus motivating acquisition of three-channel MWRs (MWR3Cs). The MWR3Cs are the latest addition to the DOE ACRF and are in the early stage of deployment at all ACRFs. They extend the two-channel MWR radiance measurements at 23.8 GHz and 31.4 GHz to a third channel at 89 GHz with an increase in temporal resolution from 20 s to 10 s. The calibration algorithm for the MWR3Cs operates in a similar fashion to that of the two-channel MWRs but is self-calibrating. The MWR3C was designed to achieve increased accuracy of retrieved precipitable water vapor and cloud LWP. With the introduction of a higher frequency, MWR3Cs are able to attain cloud LWP retrievals with uncertainties of 15-20 g m^{-2}, less than those attained by the two-channel MWRs (Cadeddu et al., 2013).

Although the MWR3Cs provide todays most trusted cloud LWP measurements, their retrievals still have uncertainties due to radiometric uncertainties, gas spectroscopy of both water vapor and oxygen, liquid water dielectric constants used by the microwave absorption models, and the retrieval method itself.

1.2 Methods of Retrieving Cloud LWC

Although relatively accurate cloud LWP retrievals are now available, accurate cloud LWC retrievals are not. The DOE ARM program has attempted various methods to retrieve cloud LWC for much of the past decade. One approach to retrieve LWC uses the combination of cloud base and cloud top measurements from lidar and radar together with MWR-retrieved cloud LWPs. With an assumed adiabatic profile, cloud LWC can be inferred. In another approach, Frisch et al. (1998) proposed a method for determining stratus cloud LWC profiles using a MWR and a cloud radar. This method is independent of radar calibration and cloud-droplet size distribution provided that the sixth moment of the size distribution can be related to the square of the third moment. However, this method is limited to non-drizzle cases because the common occurrence of drizzle drops greater than 50 μm in stratus clouds can dominate the radar reflectivity yet contribute little to the cloud LWC. These existing techniques make strong assumptions about cloud LWC that are not readily verified and, as a result, their accuracies are not well characterized.

The attenuation of microwave radiation by liquid drops, provided that the drop diameters are one third or less than the wavelength of the radiation, is directly proportional to cloud LWC and increases with frequency in a known way. Therefore, the difference in reflectivities measured at two different microwave frequencies can be used to deduce cloud LWC. Atlas (1954) first proposed this use of differential attenuation with the intention of measuring the water content of rain. However, lack of adequate instrumentation limited implementation of the approach at the time. Sekelsky (2000) demonstrated the use of this differential absorption technique with two attenuating radar frequencies, 35- and 95-GHz, to determine microphysical properties of liquid clouds, including LWC. Selection of the higher frequency is a trade-off between better sensitivity to small drops and cloud attenuation, while the lower frequency is a trade-off between sensitivity to small drops, cloud attenuation, and system portability (Sekelsky and McIntosh, 1996).

Hogan et al. (2005) tested the Sekelsky (2000) differential attenuation method using 35- and 95-GHz radar measurements. Retrieval of cloud LWC can be ob-

tained, even in the presence of drizzle, provided that all of the liquid water drop diameters are less than a third of the wavelengths at the two frequencies. Hogan et al. (2005) found that high-resolution retrievals of cloud LWC are very sensitive to both random and non-random errors in reflectivity measurements and concluded that long dwell times, high signal-to-noise ratios and averaging over many range gates are necessary to reduce random errors in reflectivity, thereby improving the accuracy of cloud LWC retrievals but degrading their spatial and temporal resolution.

To reduce noise impacts on the retrievals without degrading their temporal or spatial resolution, Huang et al. (2009) incorporated total variation regularization techniques into the dual-frequency radar retrieval approach. They introduced smoothness, non-negativity, and double-sided data constraints to decrease the uncertainties due to errors in the reflectivity measurements. This technique is similar to those used in image processing to recover corrupted noisy digital images and is relevant to diverse applications.

Benefits of a dual-frequency radar retrieval approach are several-fold. Absolute calibrations of the individual radars and assumptions of cloud drop size distributions are not required in the approach, though the assumption of the liquid drops being small relative to the radar wavelength is (Hogan et al., 2005). Cloud bases of drizzling clouds can be retrieved using this approach and assessed using cloud base height measurements provided by ceilometers located at each ACRF. These benefits are not realizable with previous methods of retrieving cloud LWC. Despite the many advantages of this retrieval, this approach does have some disadvantages as well. The retrieved cloud LWC is sensitive to radar measurement noise, range gate offsets, beam pointing errors, beam width differences, amount of cloud LWC present, and cloud liquid water drop diameters greater than a third of the wavelength.

In this thesis, we evaluate the accuracy of cloud LWCs retrieved via the dual-frequency radar approach developed by Huang et al. (2009). We test multiple boundary-layer liquid only cloud cases containing various amounts of liquid water during 2012-2013 across four climatologically different locations (Fig. 1.1). The observational data for the cases that we selected were obtained from the 35-GHz (Ka-band) and 95-GHz (W-band) cloud radars located at the North Slope of Alaska

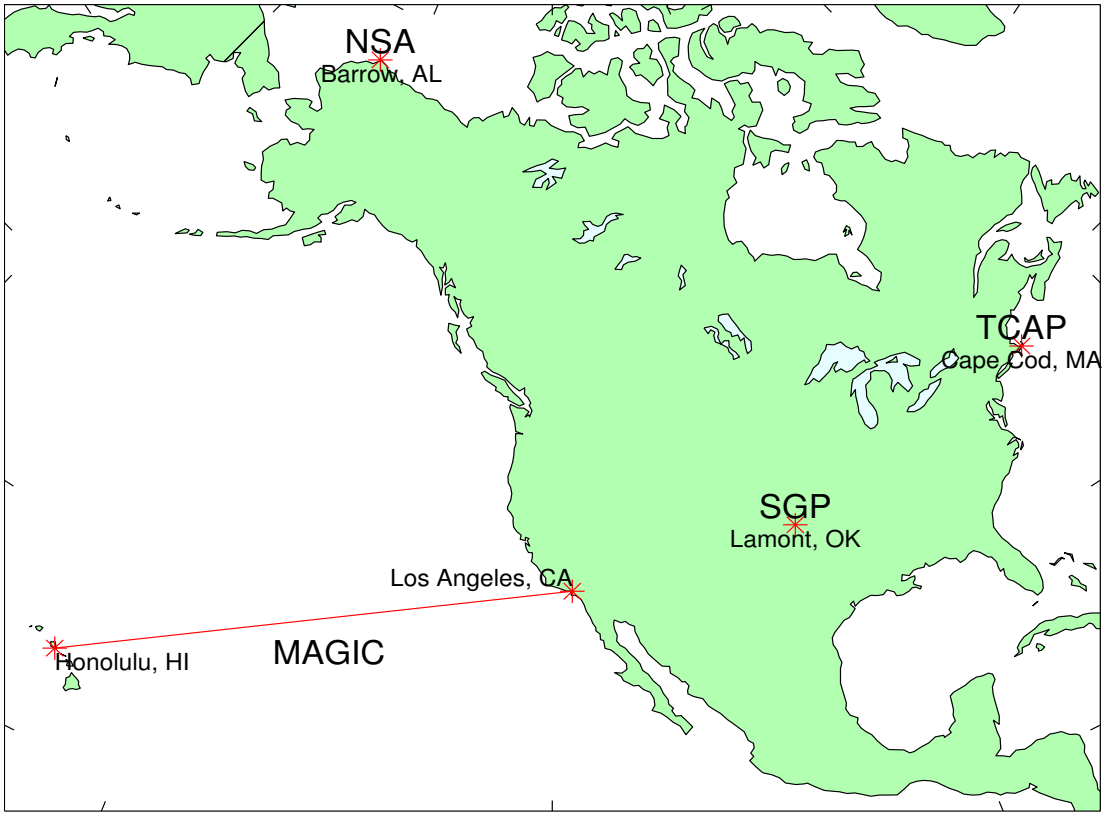

Figure 1.1: A geographical depiction of the locations of each ACRF used in this study.

(NSA) and Southern Great Plains (SGP) permanent ACRFs, the first ARM mobile facility (AMF1) deployed to the Two Column Aerosol Project (TCAP) and the second ARM mobile facility (AMF2) deployed to the Marine ARM GCPI Investigation of Clouds (MAGIC) campaign.

In Chapter 2 of this thesis, we explain the methodology of the dual-frequency radar retrieval approach developed by Huang et al. (2009) and our methods for assessing the LWC retrievals from it. Chapter 3 includes the case selection criteria and a summary of selected case periods from each site as well as the observational data and instrumentation used. In Chapter 4, we present the results and in Chapter 5 we discuss the results and draw conclusions from them. Finally, in Chapter 6, we summarize this study and consider future work that follows from this study.

Chapter 2

Methodology

This chapter describes the methodology behind the dual-frequency radar cloud LWC retrieval algorithm. It also contains explanations on how the retrieval algorithm results are generated, how various sensitivity tests are implemented to evaluate the performance of the retrieval algorithm, and how results are evaluated through comparisons with other DOE ARM data products.

2.1 Dual-frequency Radar Cloud LWC Retrieval Algorithm

The dual-frequency radar cloud LWC retrieval algorithm is based on the principle that electromagnetic radiation is absorbed and scattered by all of the constituents in the atmosphere. Radars transmit radiation at a specific wavelength and measure the attenuated radiation scattered by atmospheric particles back to the radar, which is converted to radar reflectivity. In all of our cases, the radiatively important atmospheric constituents are oxygen, water vapor, and cloud liquid water drops. Scattering of microwave radiation by both gases (as well as all other gases) is negligible, whereas absorption by them is not. While scattering of microwave radiation by small (compared to the wavelength) cloud liquid water drops is what leads to the signals measured by the radar, the contribution of scattering to overall attenuation is negligible compared to absorption by oxygen, water vapor and the cloud liquid water drops. Absorption of radiation by the gases and cloud

liquid water drops is stronger at 95 GHz than at 35 GHz so a signal transmitted by a 95-GHz (W-band) radar will increasingly be absorbed more with height by them than a signal transmitted by a 35-GHz (Ka-band) radar. Therefore, 95-GHz radar reflectivity measurements decrease faster with height in a liquid cloud and the ratio of the 35- to 95-GHz radar reflectivities should, based on this differential absorption, increase monotonically with height.

If any ice particles or drizzle drops greater than about one-third the wavelength transmitted by the W-band radar are present, then the differences in radar reflectivity between the W- and Ka-bands can also increase because of a drop (resonance) in W-band scattering, and not only because of differential absorption between the two radars. Therefore, this retrieval is viable only when the clouds drops are smaller in diameter than one-third of both the 35- and 95-GHz radar wavelengths.

Assuming there are no ice particles or large drizzle drops present, the attenuated radar reflectivity $Z_f(h)$ (in dBZ) at height h and frequency f can be calculated from the unattenuated reflectivity $Z^{\mathrm{u}}(h)$ at the same height and the atmospheric absorption coefficient, a_f (in meters; (Huang et al., 2009)). The relationship can be written as Hogan et al. (2005)

$$Z_f(h) = Z^{\mathrm{u}}(h) - 2\int_0^h \alpha_f(z)dz. \tag{2.1}$$

The unattenuated reflectivity $Z^{\mathrm{u}}(h)$ is not a function of radar frequency f provided that the particle size is less than a third of the radar wavelength so that the radar scattering is in the small particle regime. The attenuation of the radar signal is mainly due to absorption by cloud liquid water drops with the attenuation coefficient

$$\alpha_f^{\mathrm{liq}}(h) = \kappa_f x(h), \tag{2.2}$$

where h is height (in m), κ_f is the temperature-dependent absorption efficiency coefficient (in m^2 g^{-1}) of liquid water at frequency f and $x(h)$ is the cloud LWC

(in g m^{-3}). The radar attenuation coefficient α_f at height h is a linear function of the cloud LWC $x(h)$ at the same level:

$$\alpha_f(h) = \kappa_f x(h) + \alpha^{\text{other}}(h), \tag{2.3}$$

where α^{other} is the attenuation by water vapor and oxygen. Assuming f is 35 GHz and 95 GHz, Eq. 2.1 leads to

$$Z_{35}(h) - Z_{95}(h) = -2\int_0^h [\alpha_{95}(z) - \alpha_{35}(z)]dz. \tag{2.4}$$

For simplicity, we define the dual-frequency ratio DFR in logarithmic units as

$$DFR(h)[\text{dB}] = Z_{35}(h)[\text{dBZ}] - Z_{95}(h)[\text{dBZ}]. \tag{2.5}$$

By substituting Eqs. 2.3 and 2.5 into Eq. 2.4 we obtain

$$DFR(h) = -2\int_0^h [\kappa_{35}(z)x(z) + \alpha_{35}^{\text{other}}(z) - \kappa_{95}(z)x(z) - \alpha_{95}^{\text{other}}(z)]dz. \tag{2.6}$$

From Eq. 2.5, the mean cloud LWC in a layer between heights h_{i-1} and h_i can be determined from the DFR measured at the top, DFR_i, and bottom, DFR_{i-1}, of the layer:

$$x = \frac{1}{\kappa_{35} - \kappa_{95}}[\frac{DFR_i - DFR_{i-1} - b_i}{-2(h_i - h_{i-1})}], \tag{2.7}$$

where

$$b_i = (h_i - h_{i-1})[\alpha_{95}^{\text{other}}(h_i) + \alpha_{95}^{\text{other}}(h_{i-1}) - \alpha_{35}^{\text{other}}(h_i) - \alpha_{35}^{\text{other}}(h_{i-1})] \tag{2.8}$$

represents the difference in radar reflectivity due to absorption by cloud liquid

water after having accounted for absorption by oxygen and water vapor (Hogan et al., 2005, Huang et al., 2009). This direct approach can be solved analytically given that the radar reflectivities can be measured at each height at 35 GHz and 95 GHz by dual-frequency radars. However, many studies have shown that this direct solution is very sensitive to error in the radar reflectivity measurements (Hogan et al., 2005, Huang et al., 2009, Sekelsky, 2000).

2.1.1 Implementation of Total Variation Regularization Technique

The method proposed by Huang et al. (2009) converts the retrieval problem for a dual-frequency radar into an inversion matrix equation so that constrained approaches can be used to improve the uncertainties in LWC retrievals due to noisy radar data:

$$\mathbf{Ax} = \mathbf{b}, \tag{2.9}$$

where $x^T = (x_1, x_2, ..., x_n)$ is the vector of cloud LWC, $b^T = (b_1, b_2, ..., b_n)$ is the radar differential attenuation, and $A = (a_{ij})$ is the triangular matrix

$$\alpha_{ij} = \begin{cases} 2\Delta h(\kappa_{95} - \kappa_{35}), & i \geq j \\ 0, & \text{otherwise} \end{cases} \tag{2.10}$$

Equation 2.9 is solved using the total variation regularization approach that is widely used in ill-posed inversion problems with solutions sensitive to noise. Instead of minimizing the root-mean-square difference between predictions ($\mathbf{Ax}$) and observations ($\mathbf{b}$), Huang et al. (2009) minimizes the total variation of the retrieval through the addition of smoothness, nonnegativity, and double-sided data constraints.

The smoothness constraint leads to smoother LWCs with height while allowing for discontinuities in the profile. The smoothness constraint is implemented using the Tikhonov regularization method so that additional constraints can be incorpo-

rated (Tikhonov, 1963). The Non-Negative Least Squares (NNLS) algorithm was introduced by Lawson and Hanson (1974) and imposes a non-negativity constraint as LWCs are intrinsically positive values, thereby forcing the solution to always be positive. With a priori knowledge of the solution's range, "double-side" constraints can be used to bound the solution. One such method used here was developed by Pierce and Rust (1985). The double-side constraints (i.e. a bounding box $\mathbf{B}$ in an n-dimensional space) are defined by a vector $\mathbf{x}_\mathrm{b}$ of the prior estimate (the center of the box) and a matrix $\mathbf{Q} \equiv \mathrm{diag}\ (q_1, q_2, \Lambda, q_n)/2$, where q_i denotes the width of the bounding box in the ith dimension (Huang et al., 2008a, Pierce and Rust, 1985). Huang et al. (2008a) combined all of these methods into a new Double-Side Constrained Smoothness-constrained Non-Negative Least Squares (DSCNNLS) algorithm which solves the following minimization problem:

$$\min_x \{\|\mathbf{x}\|_1\},\ \text{subject to}\ \|\mathbf{A}'x - \mathbf{b}'\|_2^2 \leq \varepsilon,\ \text{and}\ \mathbf{x} \leq 0, \tag{2.11}$$

where

$$\mathbf{A}' \equiv \mathbf{A}^T\mathbf{A} + \lambda\mathbf{L}^T\mathbf{L} + \tau\mathbf{Q}^{-2}$$

$$\mathbf{b}' \equiv \mathbf{A}^T\mathbf{b} + \tau\mathbf{Q}^{-2}\mathbf{x}_b$$

and λ is the regularization parameter determining the amount of smoothness imposed on the retrievals, $\mathbf{L}$ is chosen as an approximation of the two-dimensional first derivative operator, $\mathbf{x}_\mathrm{b}$ is the first-guess estimate of LWC, τ is the variance of the measurement error, which determines the contribution from the first-guess estimate to the solution, and ε denotes the error tolerance determined by the measurement error (Huang et al., 2008a). Here, ε is set to be $\sqrt{2} \times 0.5n$ (in dBZ), where n is the dimension of the observation vector $\mathbf{b}$ and 0.5 dBZ represents the uncertainty in the measured radar equivalent reflectivity factor for both range gates with and without precipitation (Huang et al., 2009). This retrieval algorithm is iterative and finds the solution that satisfies the constraints within ε when moving towards the direction of the smallest total variation.

2.2 Assessment of Dual-frequency Radar LWC Retrievals

Assessment of the dual-frequency radar cloud LWC retrieval algorithm requires reliable data products to serve as the "truth" for comparison. Here, we calculate radar-retrieved cloud LWPs from the radar-retrieved cloud LWCs and compare them to MWR-retrieved LWPs. We evaluate how the dual-frequency radar retrieval handles radar noise, as this is one of the primary limitations to the retrieval. To do this, we temporally average and spatially filter the radar data, apply the radar retrieval to these data, and assess the LWC results via comparisons to ceilometer cloud base heights and to MWR-retrieved cloud LWPs.

2.2.1 Comparison of Dual-frequency Radar-Retrieved LWPs to MWR-retrieved LWPs

Comparable absorption physics in both the radar retrieval and the MWR retrievals of cloud LWP is necessary for proper comparison. The dual-frequency radar retrieval and the MWR LWP retrievals utilize atmospheric gas and liquid water absorption models in their algorithms. In order to properly assess our results and determine their accuracy, the oxygen, water vapor, and liquid water absorption models used within the radar retrieval algorithm should be consistent with those used in the MWR retrieval algorithms.

The radar retrieval originally computed water vapor and oxygen absorption at both frequencies using the Rosenkranz 1998 gas absorption model (Rosenkranz, 1998) while the MWRs use a model more akin to the MonoRTMv5 gas absorption model (Turner et al., 2009). Therefore, we updated the radar retrieval to use the latest MonoRTM gas absorption model so errors do not arise from differences in gas absorption calculations. The radar retrieval originally computed liquid water absorption at both frequencies using the Liebe 1991 model (Liebe et al., 1991) for the complex permittivity of water while the MWR retrievals use the Liebe 1993 model (Liebe et al., 1993). Cadeddu and Turner (2011) evaluated the effects of the Liebe 1991, Liebe 1993, Stogryn 1995 (Strogryn et al., 1995) and Ellison 2006 (Ellison, 2006) models on absorption calculations at temperatures between -30 °C

and 10 °C at 23.8 GHz, 31.4 GHz, 90 GHz, 150 GHz, and 170 GHz frequencies. At temperatures below approximately -5 °C, significant differences are seen between model liquid water absorption coefficients at 90 GHz, 150 GHz, and 170 GHz and at temperatures below approximately -20 °C significant differences are seen at 23.8 GHz and 31.4 GHz (see Figure 4 of Cadeddu and Turner (2011)). Because the dual-frequency radar retrieval of cloud LWC works only for liquid water clouds, we selected cases with temperatures near or above 0 °C. Based on the study of Cadeddu and Turner (2011), the Liebe 1991 and Liebe 1993 models show nearly no difference between their liquid water absorption coefficients in this temperature range. Therefore, the Liebe 1991 liquid water absorption model is acceptable in the radar retrieval for this study.

Once cloud LWC profiles are retrieved first using 10-s temporally averaged radar data, they are summed over all heights for each 10-s period to provide corresponding cloud LWPs that are compared to LWPs retrieved by the MWR3C or the GVR. We consider the radiometer values as "truth" and determine the accuracies of the retrieval results through the evaluation of differences between the radar- and MWR-retrieved LWPs. The mean and standard deviation of these differences are computed with and without erroneous values less than or equal to -0.5 mm and greater than or equal to 0.5 mm.

2.2.2 Implementation of Temporal Averaging and Spatial Filtering

Many dual-frequency radar attenuation studies have found that noisy radar data can produce large errors in retrieved LWC (Hogan et al., 2005, Huang et al., 2008b, Sekelsky, 2000). To reduce radar noise, one can transmit more power or build quieter receivers, but this is not currently possible. One can also use techniques designed to handle noise in the retrieval, which is exactly what Huang et al. (2009) developed to reduce the influence of radar noise. The main focus of our evaluation is assessing how well the dual-frequency radar retrieval, with total variation regularization techniques included, handles radar noise by investigating how temporal averaging and spatial filtering impacts the retrieval results.

We first import 10-s temporally averaged radar data to the radar retrieval and

assess the resulting radar-retrieved LWPs via comparisons with MWR-retrieved LWPs. Additional 0.4-s, 2.5-s, 5.0-s, 20.0-s, and 60.0-s temporally averaged radar data are calculated, imported to the radar retrieval, and assessed in the same manner. We also inspected the physical reasonableness of the spatial patterns within the LWC profiles and subsequently applied a spatial median filtering scheme (Johannes Verlinde, personal communication) to the DFR data. The spatial median filter smoothens the radar data by replacing each value with the median calculated using a 3 by 3 box of values centered on it. The radar data is temporally averaged across each time resolution and the spatial median filter is applied to the subsequent DFR data. The filtered DFR data is applied to the radar retrieval and the retrieved LWC results are assessed via comparison to those retrieved without any spatial filtering.

Finally, we compare radar reflectivities to cloud base height measurements obtained from ARM ceilometers and assess where cloud base is located and if there is drizzle present below the cloud. Then we indirectly evaluate how the radar retrieval captures drizzle and cloud structure near cloud base. For instance, if there is drizzle below cloud base, the radar-retrieved LWCs should noticeably increase from just below to just above cloud base. In other cases where there is no drizzle present, the radar-retrieved LWCs should first occur near lidar-detected cloud base. Finally, if there are no cloud base heights measured by the ceilometer, we infer that there are no clouds present and the sky is clear. In this case, the radar should retrieve zero LWC and zero LWP while the MWR will potentially retrieve very small LWPs, even in clear sky conditions.

Chapter 3

Instruments and Observational Data

The reflectivity and signal-to-noise-ratio measurements from Ka-band (35-GHz) and W-band (95-GHz) ARM cloud radars and the pressure, temperature, and relative humidity measurements from ARM Balloon-Borne Sounding Systems (SONDEs) are all directly incorporated into the dual-frequency radar retrieval algorithm of cloud LWC. We assess LWP results from the radar retrieval using LWPs retrieved from MWRs as a comparison. Moreover, estimates of cloud base height obtained from the radar retrieval are directly compared with those retrieved from Vaisala ceilometers.

3.1 Instruments and Data for Dual-frequency Radar Retrieval

The Ka/W-SACR is a dual-frequency Scanning ARM Cloud Radar (SACR) with the Ka-band SACR (KASACR) and the W-band SACR (WSACR) placed on a single pedestal. The temporal and spatial resolutions of the two radars are 2.06 s and 25 m, respectively. The current scan strategies and other characteristics for all the SACRs are provided in Bharadwaj et al. (2012). Sampling intervals of the KASACR and the WSACR in the vertical pointing mode (elevation angle of 90) are variable. The beamwidths of the KASACR and the KASACR are 0.33° and 0.30°, respectively. The SACR systems are calibrated using a novel approach with a corner reflector that is located approximately 500 m from the SACR. At this

time the calibration sequence has been applied only to SGP SACR data and for only a limited period of time.

During the AMF2 deployment aboard the Horizon Lines ship, *Spirit*, which traveled between Los Angeles, California and Honolulu, Hawaii from October 2012 to September 2013, Ka-band Zenith Radar (KAZR) and the Marine W-band ARM Cloud Radar (MWACR) constantly took measurements of marine boundary layer clouds. The MWACR was placed on a stabilized platform and pointed in the zenith direction regardless of ship movement. The KAZR was not placed on a stabilized platform because of its large size and weight and, therefore, moved with the ship causing beam-pointing errors. The KAZR and MWACR have temporal resolutions of 0.37 s and 2.0 s, respectively, and radar sample volume vertical resolutions of 30 m. The KAZR beamwidth is 0.30° and the MWACR beamwidth is 0.29°.

The SONDE at each ACRF provides vertical profiles of the thermodynamic state of the atmosphere, the wind speed and wind direction. We specifically utilize measurements of pressure, temperature, and relative humidity to determine the amount of attenuation (absorption) due to oxygen and water vapor via the MonoRTMv5 model. SONDE data are available for certain times of the day, depending on time of year and location of the ACRF. SONDE data are available two times a day at the NSA and SGP ACRFs and four times per day at the TCAP and MAGIC AMFs.

3.2 Instruments and Data for Assessment of Dual-frequency Radar Retrieval

We assess the radar-retrieved LWP results through comparison to available LWPs retrieved from the MWR located at each ACRF. The ACRF MWR3C provides time-series measurements of brightness temperatures for three channels centered at 23.8 GHz, 30 GHz and 89 GHz. Water vapor emission dominates the signal in the 23.8-GHz channel, which is on the wing of the 22.2-GHz water vapor absorption line while liquid water emission dominates in the 30 GHz channel and even more so in the 89 GHz channel (Cadeddu et al., 2013).

No retrieval is perfect. In the case of MWR-retrieved LWPs small amounts

are retrieved even during clear sky periods. Because of this and other reasons the gas and liquid water absorption coefficient models that are currently used in the MWR retrievals are undergoing tests for accuracy and have been shown to be less effective at lower (super-cooled) temperatures, especially at the higher frequencies (Cadeddu and Turner, 2011, Turner et al., 2009). Another issue with MWR-retrieved LWPs occurs during periods of precipitation, when water on the MWR window causes scattering by larger liquid drops and leads to errors. The newly acquired MWR3Cs have built in mechanisms to quickly dry the instrument lenses, improving the accuracy of retrievals during light precipitation but not all precipitating events (Cadeddu et al., 2013).

The G-band Vapor Radiometer (GVR) provides time-series measurements of brightness temperatures from four double sideband channels 1 GHz, 3 GHz, 7 GHz and 14 GHz around the water vapor line at 183.31-GHz. Atmospheric emission in this spectral region is primarily due to water vapor, with some influence from liquid water (Cadeddu et al., 2007). This instrument was placed at the NSA ACRF because of the generally low humidity conditions at the location of this site and the GVR's high sensitivity to liquid water in dry conditions. More information about the GVR can be found in Cadeddu et al. (2007). GVR data products are not yet available for the public and were provided to us by Maria Cadeddu.

The Vaisala Ceilometer is a ground-based, active, remote sensing device that measures cloud base height, vertical visibility, and backscattering signals by aerosols. The transmitter emits near-infrared pulses of light and the receiver detects light scattered back by aerosols, clouds and precipitation. If there are no clouds above the instrument, no retrieval of cloud base height should be made. We compare these cloud base height measurements obtained from each ACRFs Vaisala Ceilometer to the radar-retrieved LWC and evaluate the capability of the radar retrieval in the detection of cloud structure and any drizzle below cloud base.

3.3 Case Study Periods

We searched for cases of liquid only stratus/stratocumulus clouds located within the boundary layer and the lower free troposphere (below 6 km). Because the KASACR and the WSACR are new instruments, they are going through growing

pains and are often off-line. Therefore, we searched all available W- and Ka-band radar data from the NSA and SGP ACRFs, and the TCAP and MAGIC AMFs for suitable periods during which the radars were on-line and the two-frequency radar retrieval of LWC could be evaluated. We found cases representing a large range of cloud LWPs (from 0.02-5.00 mm) and various cloud types and characteristics including, but not limited to, broken, uniform, single-layer, multilayer, drizzling, and non-drizzling.

Tables 3.1 and 3.2 show a complete list of the dates and times of our selected cases and the particular instruments that were available during them. They were selected manually inspecting the Ka- and W-band data, finding a total of 65 hours from all sites: 7 hours over 4 days from NSA; 19 hours over 7 days from SGP; 7 hours over 4 days from TCAP; and 32 hours over 2 days from MAGIC. Furthermore, we selected nine four-hour case study periods (Table 3.3) that appeared to be representative of all of the data in terms of retrieval performance and atmospheric environments to use in subsequent analyses of the radar retrieval.

Site	Date	Time (UTC)	Ka-Band	W-Band	MWR	SONDE (UTC)
TCAP	9/4/12	11:43 - 12:09	KASACR	WSACR	MWR3C	11:30
TCAP	9/4/12	12:57 - 13:23	KASACR	WSACR	MWR3C	11:30
TCAP	9/4/12	14:08 - 14:33	KASACR	WSACR	MWR3C	11:30
TCAP	9/4/12	15:20 - 15:45	KASACR	WSACR	MWR3C	11:30
TCAP	9/4/12	16:32 - 16:57	KASACR	WSACR	MWR3C	11:30
TCAP	9/30/12	20:53 - 21:28	KASACR	WSACR	MWR3C	17:19
TCAP	11/5/12	21:06 - 21:31	KASACR	WSACR	MWR3C	23:14
TCAP	11/5/12	22:54 - 23:19	KASACR	WSACR	MWR3C	23:14
TCAP	11/14/12	15:09 - 15:34	KASACR	WSACR	MWR3C	17:46
TCAP	11/14/12	16:15 - 16:40	KASACR	WSACR	MWR3C	17:46
TCAP	11/14/12	27:27 - 17:52	KASACR	WSACR	MWR3C	17:46
TCAP	11/14/12	18:38 - 19:03	KASACR	WSACR	MWR3C	17:46
TCAP	11/14/12	19:49 - 20:14	KASACR	WSACR	MWR3C	17:46
TCAP	11/14/12	21:01 - 21:26	KASACR	WSACR	MWR3C	17:46
SGP	10/4/12	16:18 - 16:48	KASACR	WSACR	MWR3C	17:32
SGP	10/4/12	21:04 - 21:29	KASACR	WSACR	MWR3C	17:32
SGP	10/5/12	01:46 - 02:11	KASACR	WSACR	MWR3C	11:29
SGP	10/5/12	04:10 - 04:35	KASACR	WSACR	MWR3C	11:29
SGP	10/5/12	06:33 - 06:58	KASACR	WSACR	MWR3C	11:29
SGP	10/5/12	08:55 - 09:20	KASACR	WSACR	MWR3C	11:29
SGP	10/5/12	11:20 - 11:45	KASACR	WSACR	MWR3C	11:29
SGP	10/5/12	13:41 - 14:06	KASACR	WSACR	MWR3C	11:29
SGP	10/5/12	16:01 - 16:26	KASACR	WSACR	MWR3C	11:29
SGP	10/5/12	18:23 - 18:48	KASACR	WSACR	MWR3C	11:29
SGP	10/11/12	04:08 - 04:33	KASACR	WSACR	MWR3C	11:34
SGP	10/11/12	06:31 - 06:56	KASACR	WSACR	MWR3C	11:34
SGP	10/11/12	08:55 - 09:20	KASACR	WSACR	MWR3C	11:34
SGP	10/11/12	11:19 - 11:44	KASACR	WSACR	MWR3C	11:34
SGP	10/13/12	13:53 - 14:18	KASACR	WSACR	MWR3C	11:25
SGP	4/2/13	16:10 - 16:35	KASACR	WSACR	MWR3C	17:28
SGP	4/2/13	18:33 - 18:58	KASACR	WSACR	MWR3C	17:28

Table 3.1: Listing of the 65 hours of available W- and Ka-band radar data during periods of predominately liquid water clouds only. Each period is listed by site, date, time, the Ka-band radar, the W-band radar, the MWR, and the time of the SONDE data used in the radar retrieval.

Site	Date	Time (UTC)	Ka-Band	W-Band	MWR	SONDE (UTC)
SGP	4/2/13	9:02 - 09:27	KASACR	WSACR	MWR3C	17:28
SGP	4/2/13	11:24 - 11:49	KASACR	WSACR	MWR3C	17:28
SGP	4/2/13	13:48 - 14:13	KASACR	WSACR	MWR3C	17:28
SGP	4/2/13	21:22 - 21:47	KASACR	WSACR	MWR3C	17:28
SGP	4/3/13	02:14 - 02:39	KASACR	WSACR	MWR3C	11:31
SGP	4/3/13	04:39 - 05:04	KASACR	WSACR	MWR3C	11:31
SGP	4/3/13	07:02 - 07:27	KASACR	WSACR	MWR3C	11:31
SGP	4/3/13	09:46 - 10:11	KASACR	WSACR	MWR3C	11:31
SGP	4/3/13	12:09 - 12:34	KASACR	WSACR	MWR3C	11:31
SGP	4/3/13	14:34 - 14:59	KASACR	WSACR	MWR3C	11:31
SGP	4/3/13	17:00 - 17:25	KASACR	WSACR	MWR3C	11:31
SGP	4/3/13	19:25 - 19:50	KASACR	WSACR	MWR3C	11:31
SGP	4/3/13	22:12 - 22:37	KASACR	WSACR	MWR3C	11:31
SGP	4/18/13	05:10 - 05:35	KASACR	WSACR	MWR3C	11:30
SGP	4/18/13	07:34 - 07:59	KASACR	WSACR	MWR3C	11:30
SGP	4/18/13	10:02 - 10:27	KASACR	WSACR	MWR3C	11:30
SGP	4/18/13	12:26 - 12:51	KASACR	WSACR	MWR3C	11:30
SGP	4/18/13	15:12 - 15:37	KASACR	WSACR	MWR3C	11:30
SGP	4/18/13	17:38 - 18:03	KASACR	WSACR	MWR3C	11:30
SGP	4/18/13	20:03 - 20:28	KASACR	WSACR	MWR3C	11:30
SGP	4/18/13	22:29 - 22:54	KASACR	WSACR	MWR3C	11:30
NSA	7/25/12	15:31 20:31	KASACR	WSACR	GVR	17:30
NSA	10/1/12	04:00 - 14:00	KASACR	WSACR	GVR	17:30
NSA	10/1/12	17:00 - 18:00	KASACR	WSACR	GVR	17:30
NSA	10/1/12	20:00 - 23:00	KASACR	WSACR	GVR	17:30
NSA	10/18/12	16:26 - 16:47	KASACR	WSACR	GVR	17:30
NSA	10/18/12	18:48 - 19:13	KASACR	WSACR	GVR	17:30
NSA	10/18/12	21:12 - 21:37	KASACR	WSACR	GVR	17:30
NSA	10/18/12	23:34 - 23:59	KASACR	WSACR	GVR	17:30
NSA	10/19/12	18:42 - 19:07	KASACR	WSACR	GVR	21:48
MAGIC	11/26/12	14:00 - 22:00	KAZR	MWACR	MWR3C	17:45
MAGIC	7/8/13	00:00 - 24:00	KAZR	MWACR	MWR3C	14:32

Table 3.2: Table 2.1 continued.

Site	Date	Time (UTC)	Ka-Band	W-Band	MWR	SONDE (UTC)
TCAP	9/4/12	12:57 - 13:23	KASACR	WSACR	MWR3C	11:30
TCAP	9/4/12	14:08 - 14:33	KASACR	WSACR	MWR3C	11:30
TCAP	9/4/12	15:20 - 15:45	KASACR	WSACR	MWR3C	11:30
TCAP	9/4/12	16:32 - 16:57	KASACR	WSACR	MWR3C	11:30
TCAP	11/14/12	15:09 - 15:34	KASACR	WSACR	MWR3C	17:46
TCAP	11/14/12	16:15 - 16:40	KASACR	WSACR	MWR3C	17:46
TCAP	11/14/12	27:27 - 17:52	KASACR	WSACR	MWR3C	17:46
TCAP	11/14/12	18:38 - 19:03	KASACR	WSACR	MWR3C	17:46
SGP	10/5/12	13:41 - 14:06	KASACR	WSACR	MWR3C	11:29
SGP	10/5/12	16:01 - 16:26	KASACR	WSACR	MWR3C	11:29
SGP	4/2/13	13:48 - 14:13	KASACR	WSACR	MWR3C	17:28
SGP	4/2/13	16:10 - 16:35	KASACR	WSACR	MWR3C	17:28
SGP	4/18/13	15:12 - 15:37	KASACR	WSACR	MWR3C	11:30
SGP	4/18/13	17:38 - 18:03	KASACR	WSACR	MWR3C	11:30
NSA	7/25/12	15:31 - 19:31	KASACR	WSACR	GVR	17:30
NSA	10/18/12	16:26 - 16:47	KASACR	WSACR	GVR	17:30
NSA	10/18/12	18:48 - 19:13	KASACR	WSACR	GVR	17:30
MAGIC	11/26/12	14:00 - 18:00	KAZR	MWACR	MWR3C	17:45
MAGIC	7/8/13	14:00 - 18:00	KAZR	MWACR	MWR3C	14:32

Table 3.3: Same as Tables 2.1-2.2, but for the nine case study periods selected for detailed analyses of the performance of the dual-frequency radar retrieval algorithm.

Chapter 4

Results

We applied the dual-frequency radar cloud LWC retrieval algorithm developed by Huang et al. (2009) to all of the 10-s averaged radar reflectivity data collected at the NSA ACRF, SGP ACRF, during the AMF1 TCAP field campaign and during the AMF2 MAGIC field campaign and listed in Tables 3.1, 3.2 and 3.3.

We first present the W- and Ka-band radar reflectivity data at their original temporal resolutions that comprise the chosen nine case study periods listed in Table 3.3. These data provide a view on the types of clouds that were used in the study. Next, we apply the dual-frequency radar retrieval algorithm to all of the 10-s temporally averaged radar data. Vertical profiles of cloud LWC that result are summed and subsequently compared to the cloud LWPs retrieved from MWR radiance measurements. Comparisons are done for all of the data listed in Tables 3.1 and 3.2 and separately for the nine case study periods listed in Table 3.3.

To test the sensitivity of the retrieval algorithm to temporal averaging, we also applied it to 0.4-s, 2.5-s, 5.0-s, 20.0-s and 60.0-s temporally averaged radar data for the nine case study periods. We again compared LWPs created from the LWC profiles to MWR-retrieved LWPs and investigate the effects each time resolution has on the retrieval. Temporal consistency in the LWC retrievals is investigated as a function of temporal averaging. Moreover, a spatial smoothing scheme is applied to the radar data before applying the Huang et al. (2009) retrieval algorithm to test if smoother data lead to changes in algorithm performance.

4.1 Nine Four-hour Case Study Periods

To illustrate the kinds of radar data used in the current study we first present height versus time plots of W- and Ka-band reflectivity for the nine four-hour case study periods listed in Table 3.3. The case study periods include two from TCAP (Fig. 4.1), three from SGP (Fig. 4.2), two from NSA (Fig. 4.3), and two from MAGIC (Fig. 4.4).

The first TCAP case (Fig. 4.1) contains a thick cloud layer, a convective system and then multiple layers of various thicknesses, whereas the second TCAP case is composed of a small thin broken stratocumulus cloud layer. The first SGP case (Fig. 4.2) shows multiple stratus/stratocumulus cloud layers followed by a single thin continuous stratus cloud layer around 2 km. The second SGP case contains thicker, higher LWC clouds than the first case along with probable precipitation. The third SGP case is intermediate between the first two in terms of LWC and contains light drizzle. The two NSA cases (Fig. 4.3) consist of extremely low LWC clouds with the second case containing light precipitation. The particles falling from the cloud in the second NSA case could be drizzle or ice because the SONDE measured temperatures below 0 °C within the cloud. This case tests the retrievals capability at low temperatures. The two MAGIC cases (Fig. 4.4) illustrate stratus cloud layers that change thickness and often have drizzle falling from cloud base. These two case study periods are typical of the cloud structures observed at other times during MAGIC.

4.2 Comparison of Dual-frequency Radar-retrieved LWP to MWR-retrieved LWP

Once LWC profiles are retrieved using the 10-s temporally averaged data the LWC values at all heights are summed for each profile to compute a corresponding LWP. These LWPs are then compared to the LWPs retrieved from the MWR3C for TCAP, SGP and MAGIC and the GVR for NSA. We consider the MWR retrievals as "truth" and treat differences as errors in the dual-frequency radar retrievals. Any exceptions to this assumption are stated explicitly in the discussion that follows.

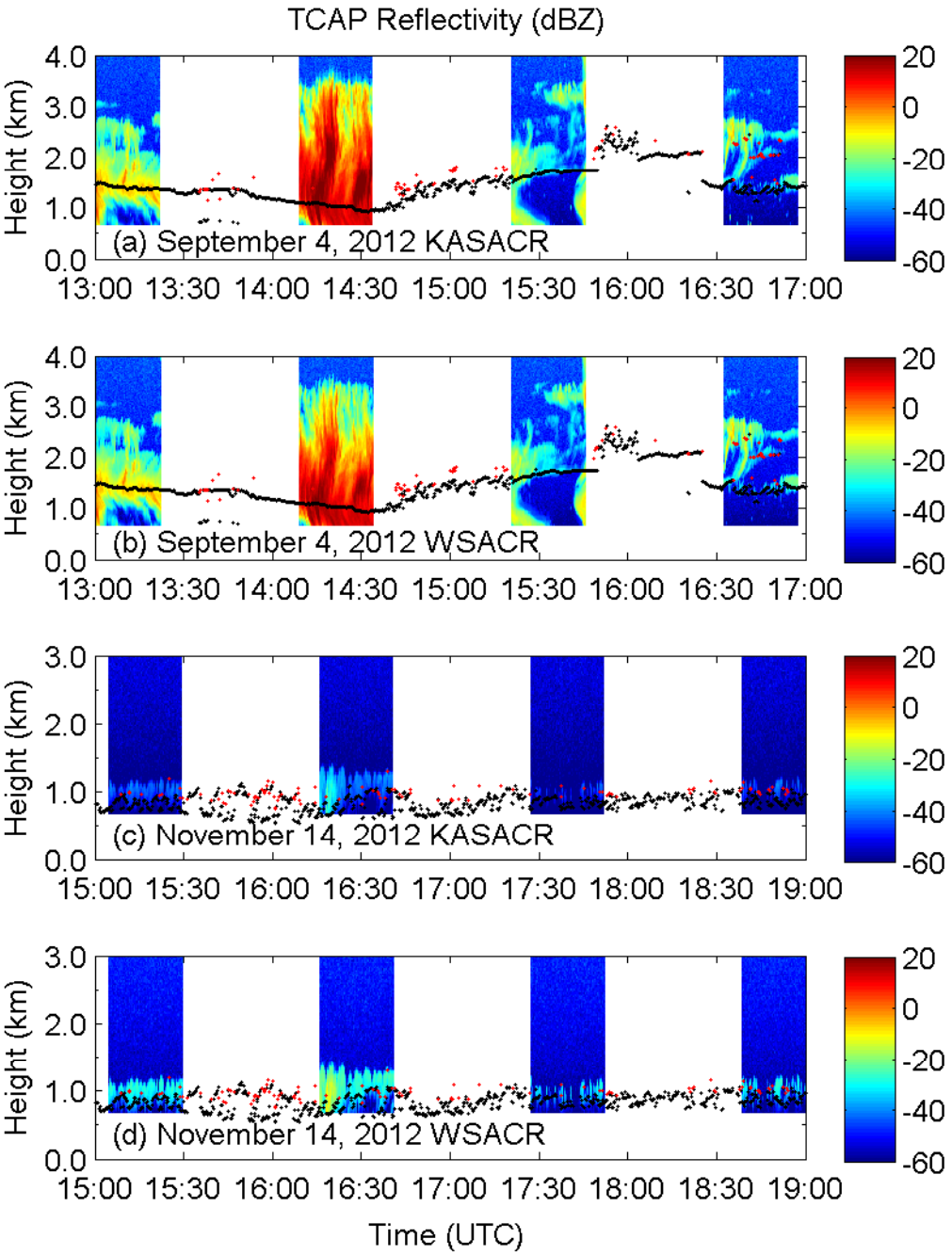

Figure 4.1: TCAP (a, c) KASACR and (b, d) WSACR height versus time reflectivities from (a, b) 13:00-17:00 UTC on 4 September 2012 and (c, d) 15:00-19:00 UTC on 14 November 2012. The black and red dotted lines are the first cloud base height and the second cloud base height, respectively, retrieved from Vaisala ceilometer measurements.

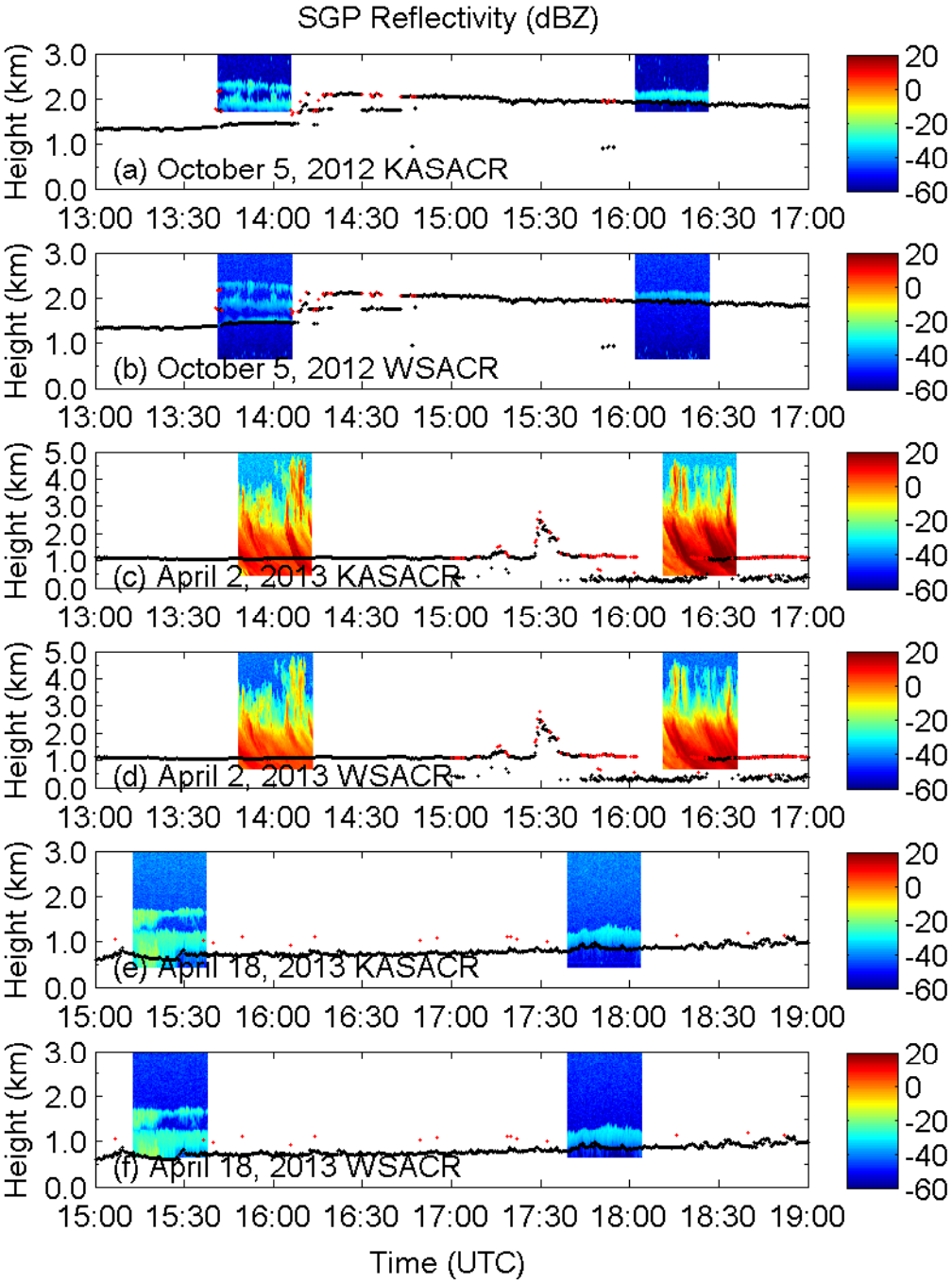

Figure 4.2: SGP (a, c, e) KASACR and (b, d, f) WSACR height versus time reflectivities from (a, b) 13:00-17:00 UTC on 5 October 2012, (c, d) 13:00-17:00 UTC on 2 April 2013, and (e, f) 15:00-19:00 UTC on 18 April 2013. The black and red dotted lines are the first cloud base height and the second cloud base height, respectively, retrieved from Vaisala ceilometer measurements.

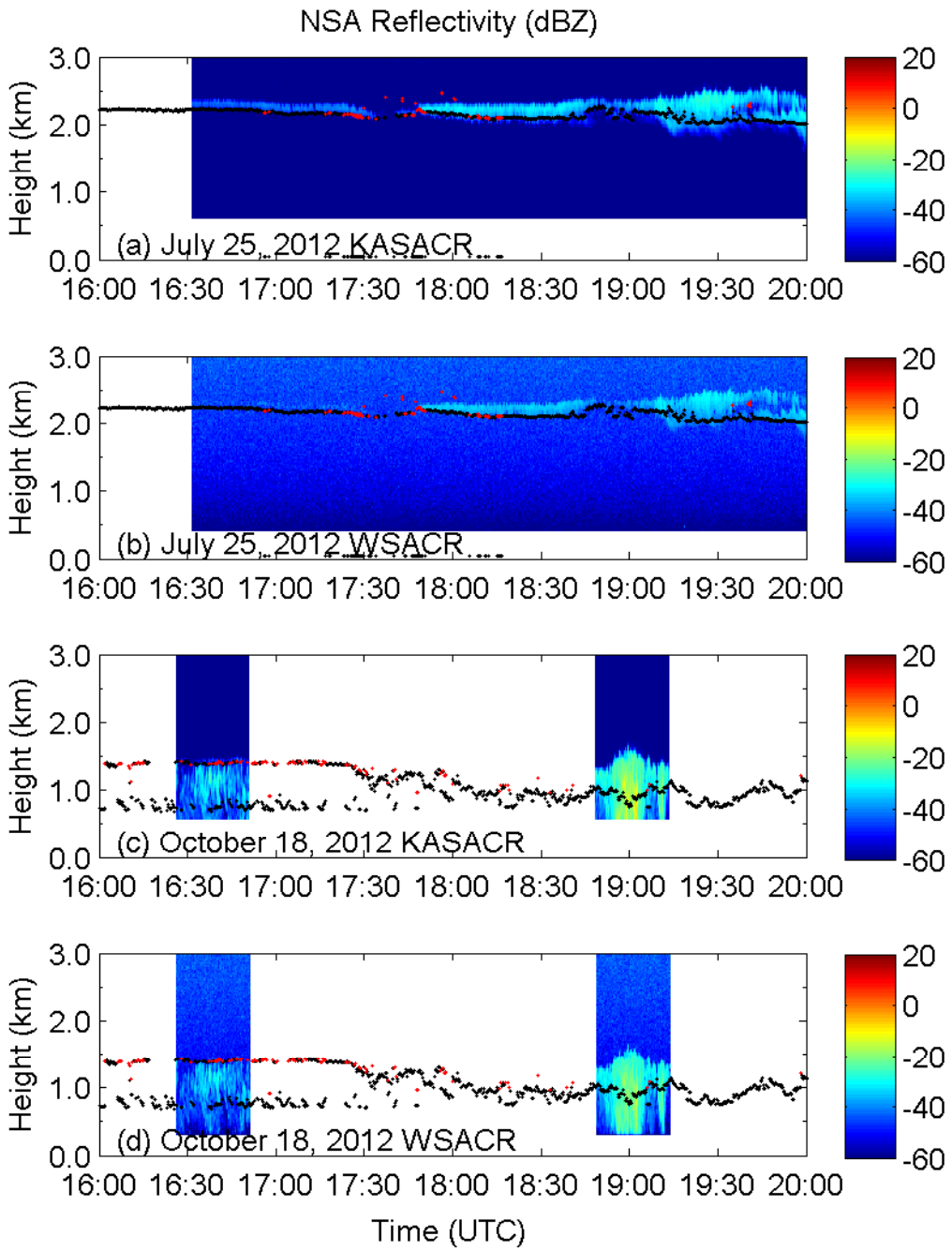

Figure 4.3: NSA (a, c) KASACR and (b, d) WSACR height versus time reflectivities from (a, b) 16:00-20:00 UTC on 25 July 2012 and (c, d) 16:00-20:00 UTC on 18 October 2012. The black and red dotted lines are the first cloud base height and the second cloud base height, respectively, retrieved from Vaisala ceilometer measurements.

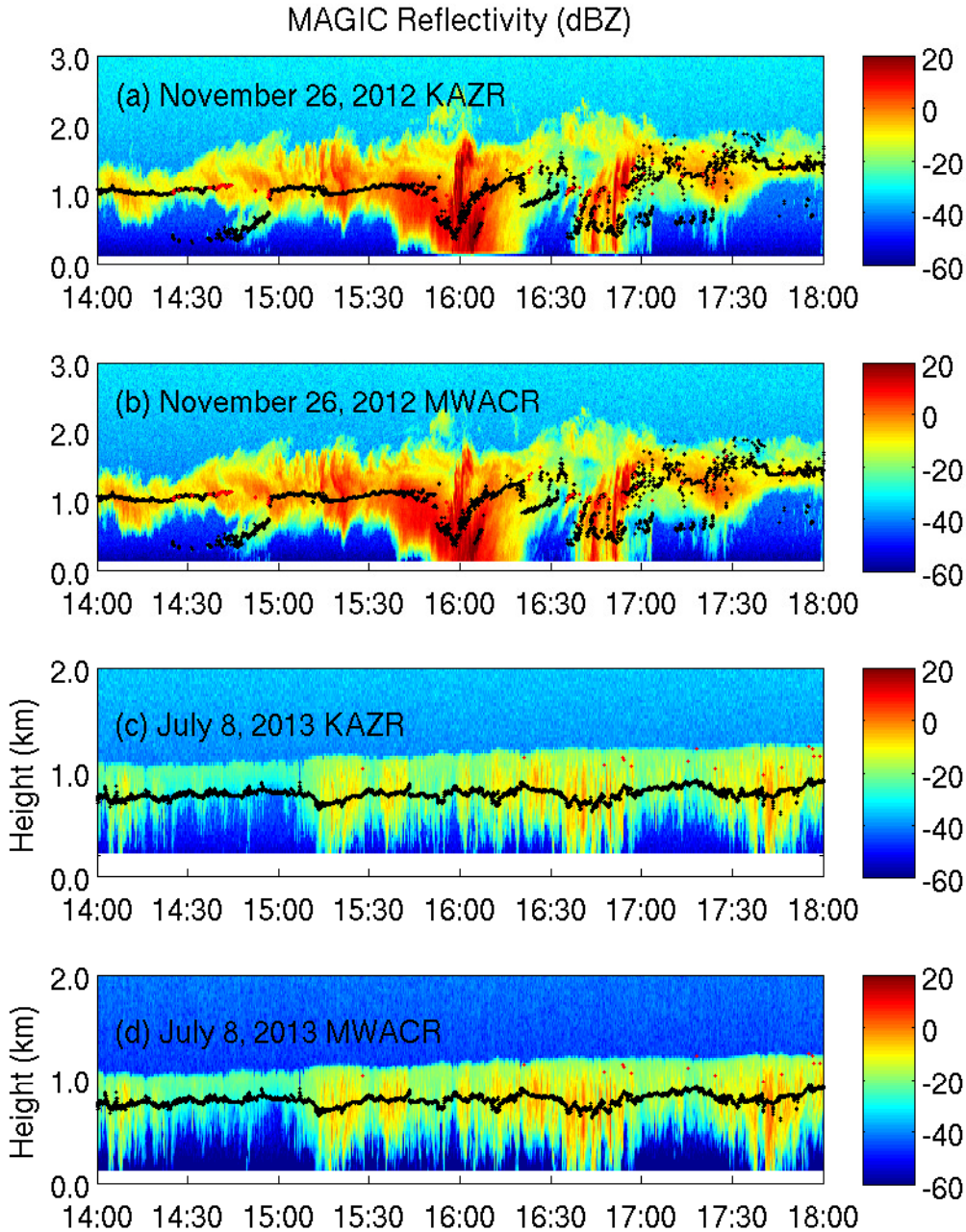

Figure 4.4: MAGIC (a, c) KAZR and (b, d) MWACR height versus time reflectivities from (a, b) 14:00-18:00 UTC on 26 November 2012 and (c, d) 14:00-18:00 UTC on 8 July 2013. The black and red dotted lines are the first cloud base height and the second cloud base height, respectively, retrieved from Vaisala ceilometer measurements.

Figures 4.5 and 4.6 contain frequency of occurrence histograms of the differences between the MWR-retrieved LWPs and LWPs retrieved using 10-s temporally averaged radar data. The means and standard deviations not in parentheses are calculated using all of the case data whereas the values in parentheses are calculated using differences that fall within -0.5 - 0.5 mm, exclusive. For visualization purposes, LWC differences less than or equal to -0.5 mm and greater than or equal to 0.5 mm are set to -0.5 mm and 0.5 mm, respectively, so one has information on the number of outliers. In Fig. **??** the frequency of occurrence histograms for the 10-s data are extended to LWP differences versus MWR-derived LWPs. Figure 4.10a displays LWP differences versus MWR-retrieved LWPs for all of the case periods in Tables 3.1 and 3.2, whereas Fig. 4.10b displays the same information but only for the nine case study periods in Table 3.3.

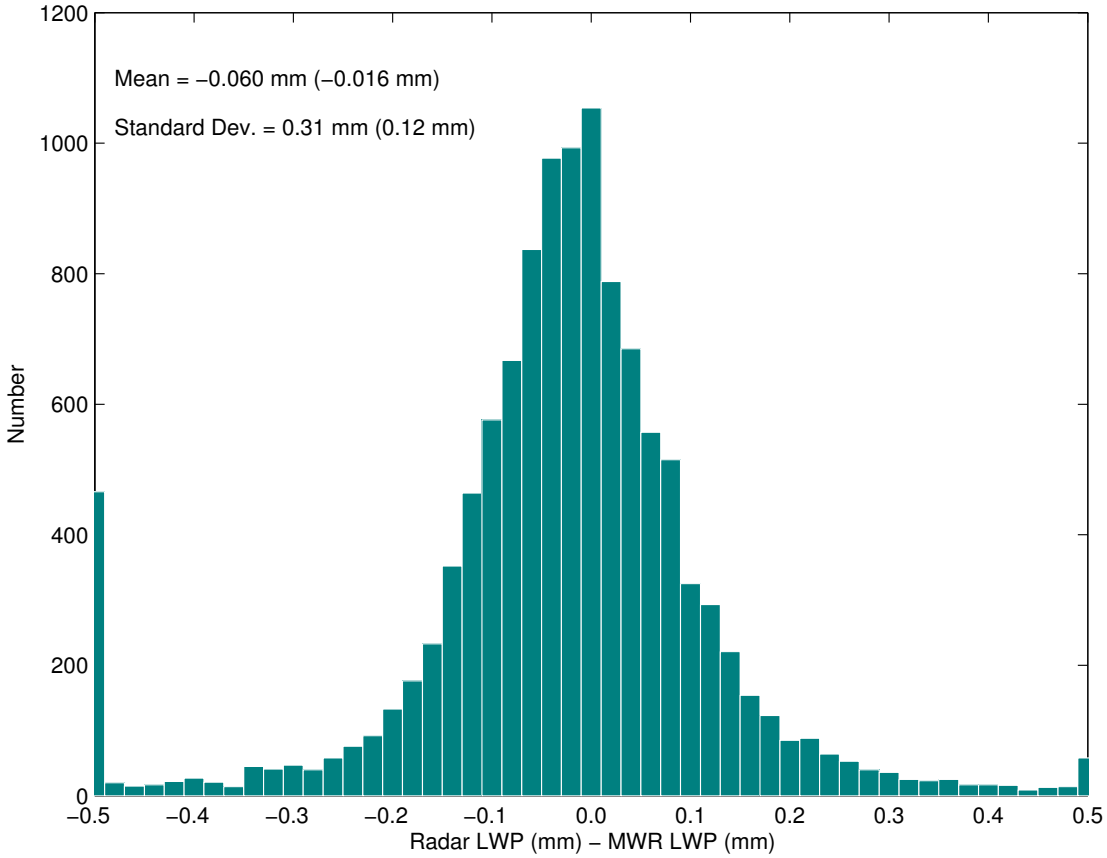

Figure 4.5: Frequency of occurrence LWP differences for all 10-s averaged data in Tables 3.1 and 3.2.

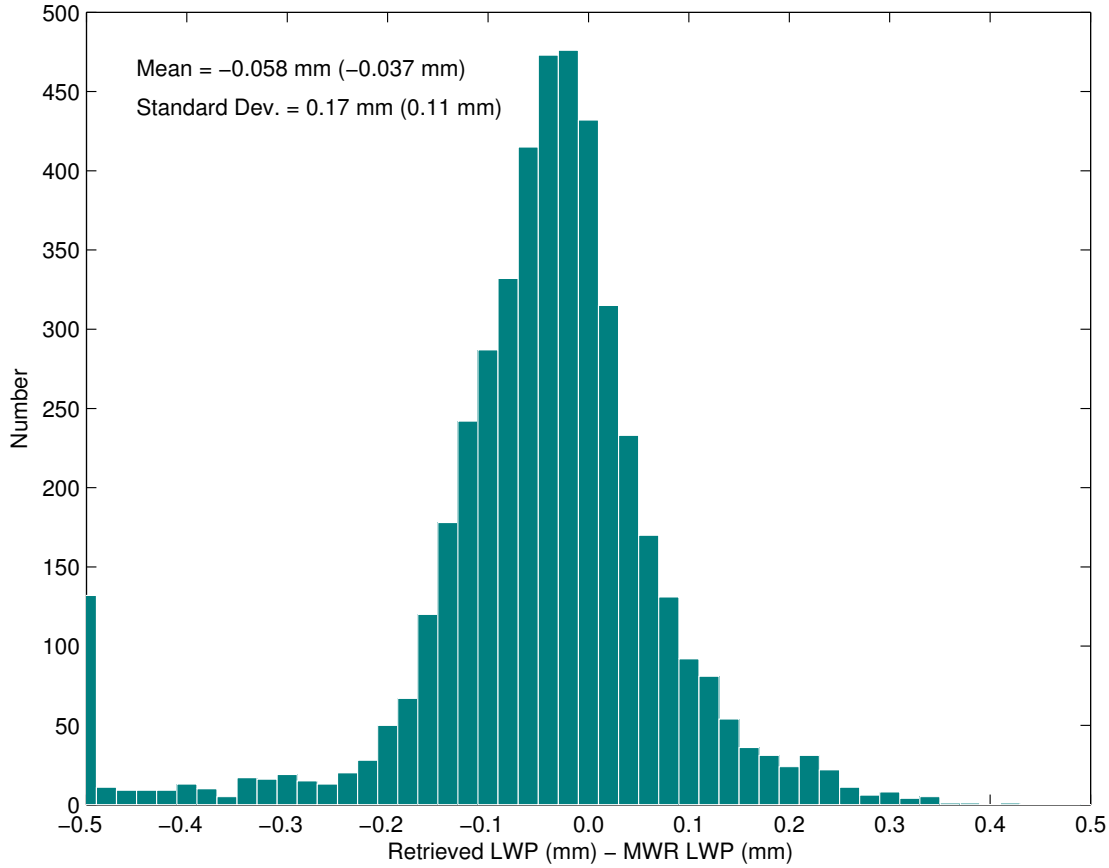

Figure 4.6: Frequency of occurrence LWP differences for all case 10-s averaged data in Table 3.3.

4.3 Impact of Temporal Resolution and Spatial Filtering

Assessing how well the radar retrieval handles radar noise is the core of our evaluation. This is one of the retrievals primary limitations according to Sekelsky (2000), Hogan et al. (2005), and Huang et al. (2008b). As explained in Chapter 2, we applied various temporal averaging to the radar data that compose the nine case study periods and applied the Huang et al. (2009) retrieval to them. Results from each of the nine case study periods are shown in a set of three consecutive figures, ranging from the LWC profiles for the first TCAP case (Fig. A.1 in the Appendix) to the histogram of the radar- and MWR-retrieved LWP differences for the last MAGIC case (Fig. A.27 in the Appendix). The first figure in each

set of three shows radar-retrieved LWC profiles. The second figure in each set shows time series of radar- and MWR-retrieved LWPs, whereas the third figure in each set contains frequency of occurrence histograms of the differences between the radar- and MWR-retrieved LWPs, just as in Figs. 4.5 and 4.6. Each set of three figures shows the results obtained using radar data that were averaged to the time resolutions of (a) 0.4 s, (b) 2.5 s, (c) 5.0 s, (d) 10.0 s, (e) 20.0 s, and (f) 60.0 s. These results in the Appendix are compactly represented here by Figs. 4.7, 4.8, 4.9, 4.11, and 4.12, which contain results identical to those for Fig. **??** but for temporal resolutions other than 10 s.

We evaluate the impact of noise and temporal consistency further by investigating the effects of spatial filtering of the LWC fields. We apply a spatial median filter to one of the MAGIC case study periods to assess retrieval sensitivity to smoothness of the MAGIC DFR data for each of the different time resolutions. The results of these sensitivity tests are assessed via comparisons to MWR-retrieved LWPs. The results from this test applied to the case from MAGIC are shown in Figs. A.28-A.30 of the Appendix. Frequency of occurrence histograms that succinctly summarize these results are presented in Fig. 4.13, in which we plot the frequency of occurrences of radar-retrieved LWPs with filtering versus radar-retrieved LWPs without filtering.

The same MAGIC example is shown in Fig. 4.14 with the cloud base heights measured from the Vaisala ceilometer plotted against the temporally averaged radar-retrieved LWCs. Figure 4.15 contains results similar to Fig. 4.14 but with spatial filtering of the DFR data. The capability of the radar retrieval to detect cloud base is illustrated by comparing Figs. 4.14 and 4.15 to the reflectivities and cloud base heights plotted for this same MAGIC case in Fig. 4.4.

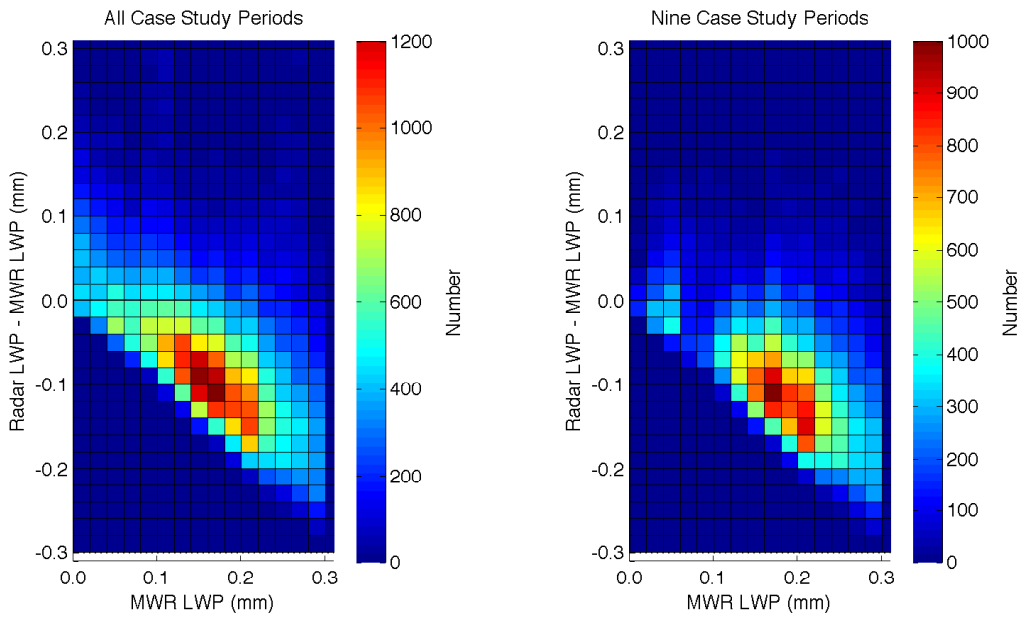

(a) (b)

Figure 4.7: Frequency of occurrence histograms of radar- and MWR-retrieved LWP differences versus MWR-retrieved LWPs for the 0.4 s temporal resolution data for (a) all of the case data in Tables 3.1 and 3.2 and (b) the nine case study periods in Table 3.3.

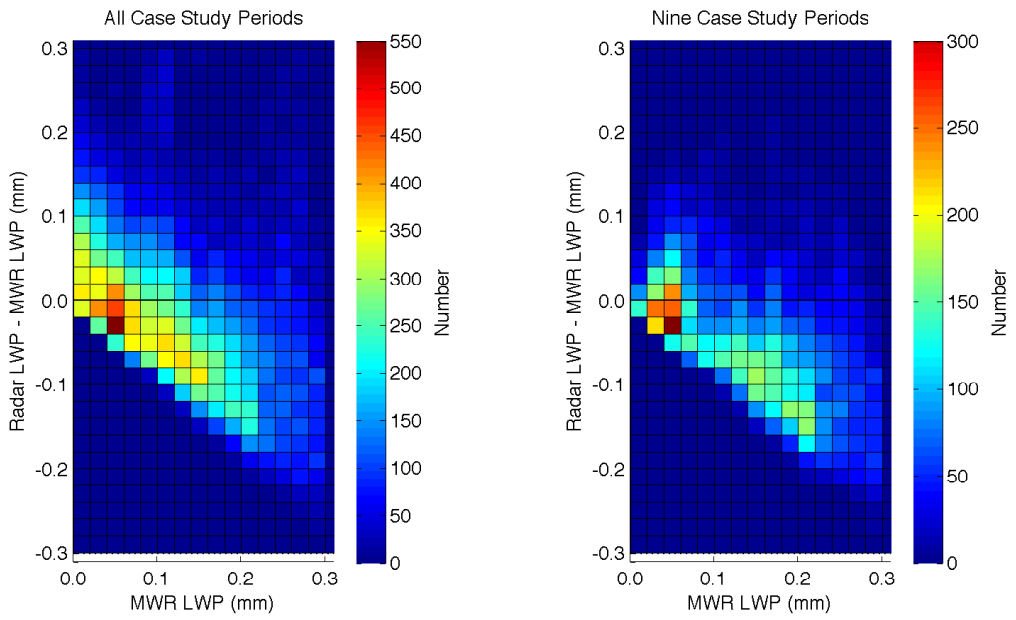

(a) (b)

Figure 4.8: Same as Fig. 4.7 but for the 2.5 s temporal resolution data.

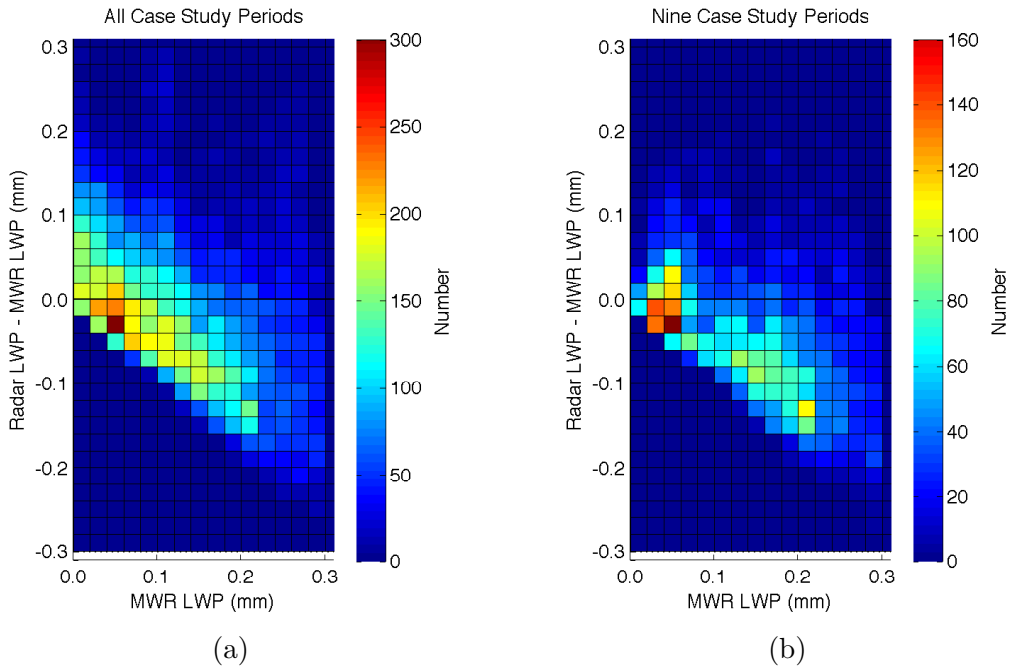

(a) (b)

Figure 4.9: Same as Fig. 4.7 but for the 5.0 s temporal resolution data.

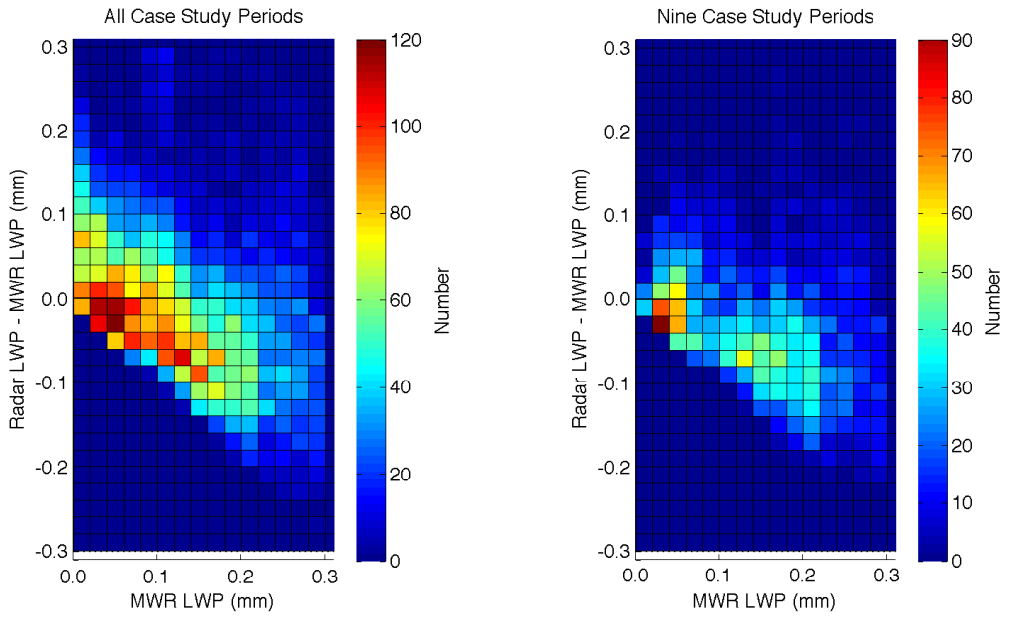

(a) (b)

Figure 4.10: Same as Fig. 4.7 but for the 10.0 s temporal resolution data.

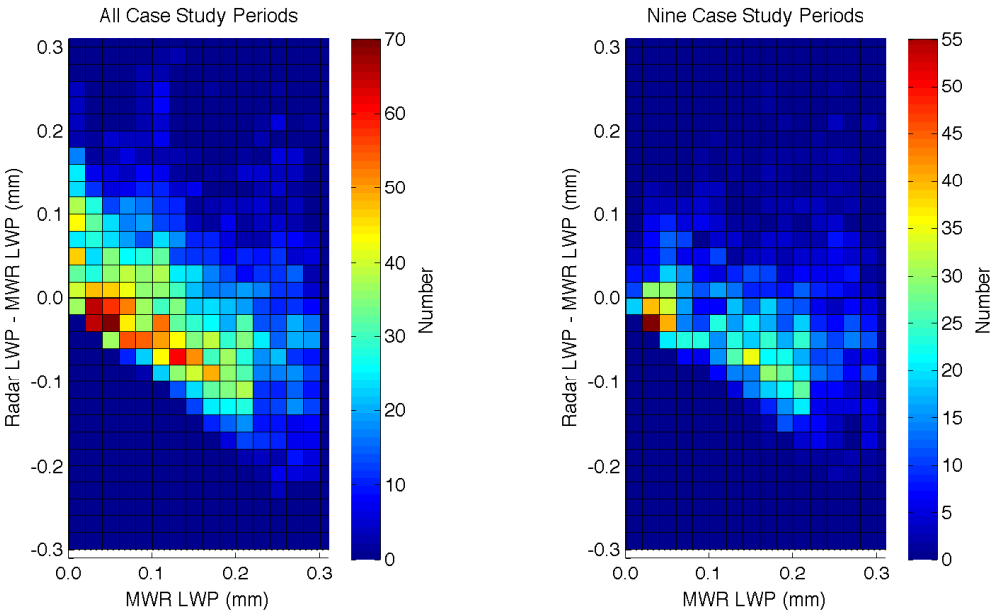

(a) (b)

Figure 4.11: Same as Fig. 4.7 but for the 20.0 s temporal resolution data.

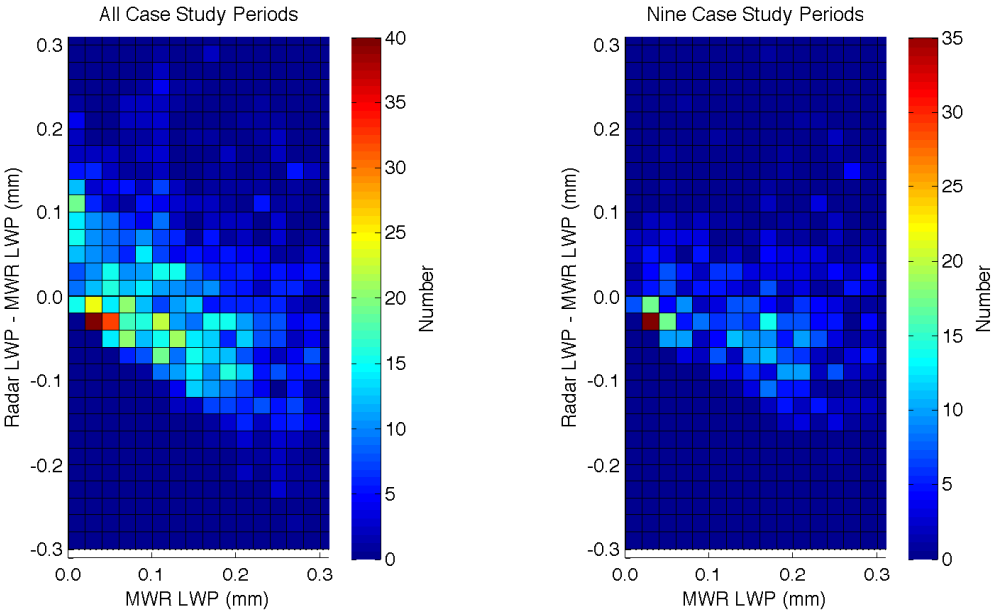

(a) (b)

Figure 4.12: Same as Fig. 4.7 but for the 60.0 s temporal resolution data.

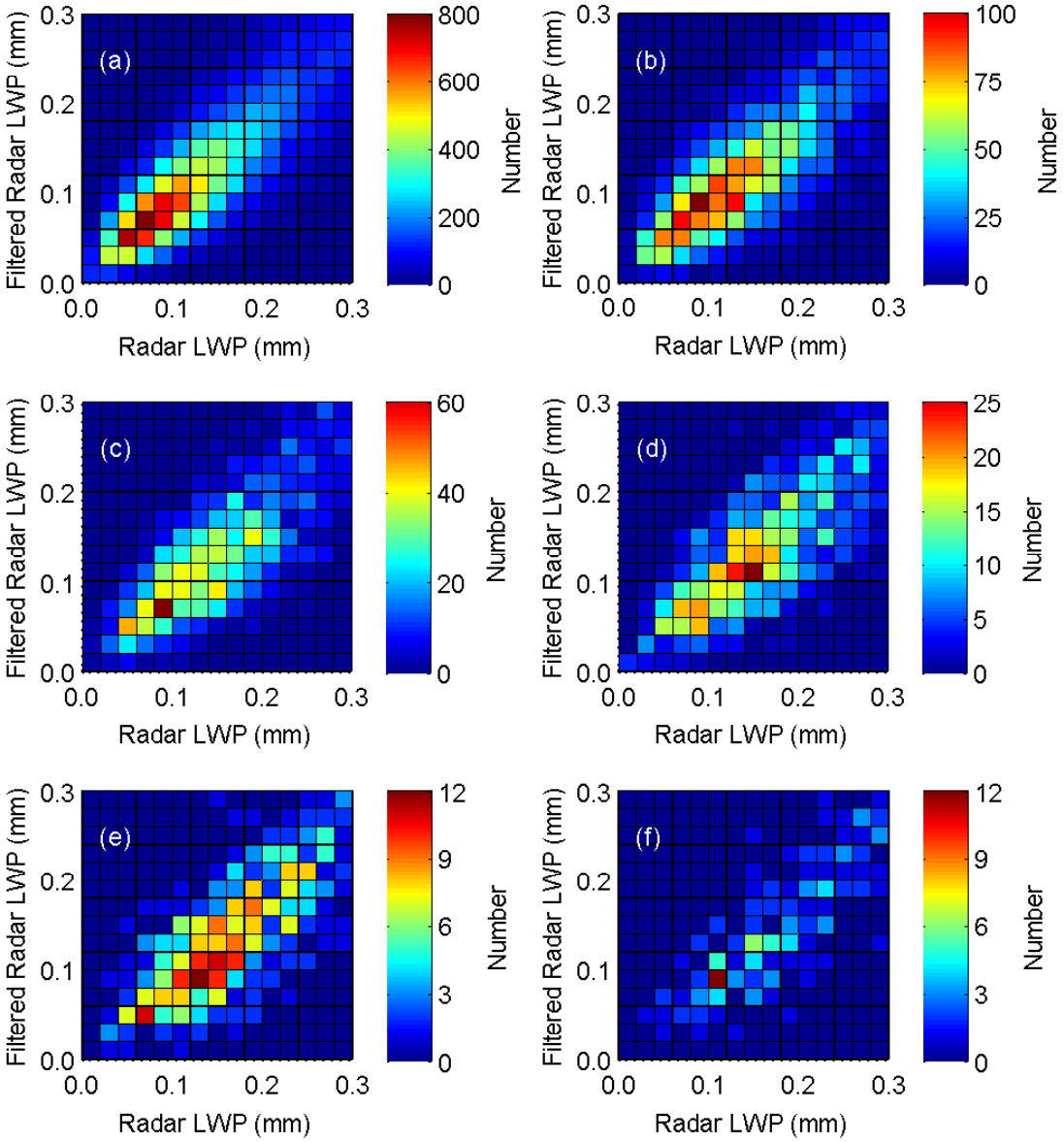

Figure 4.13: Frequency of occurrence histograms of radar-retrieved LWPs with spatial filtering versus those without filtering for time resolutions of (a) 0.4 s, (b) 2.5 s, (c) 5.0 s, (d) 10.0 s, (e) 20.0 s, and (f) 60.0 s.

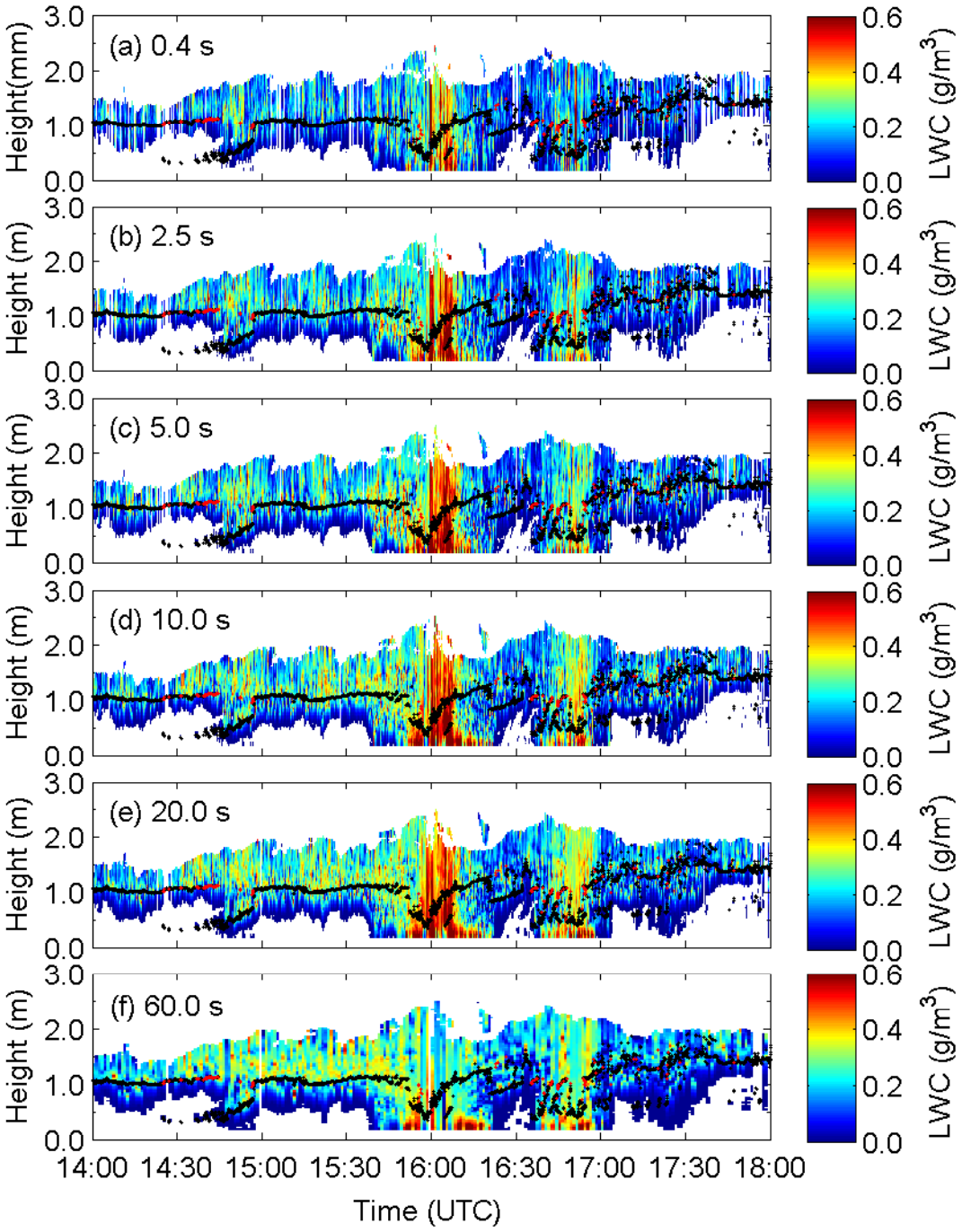

Figure 4.14: Same as Fig. A.1 but for the MAGIC period from 14:00-18:00 UTC on 26 November 2012. The black dotted line is the first cloud base height and the red dotted line is the second cloud base height retrieved from Vaisala ceilometer measurements.

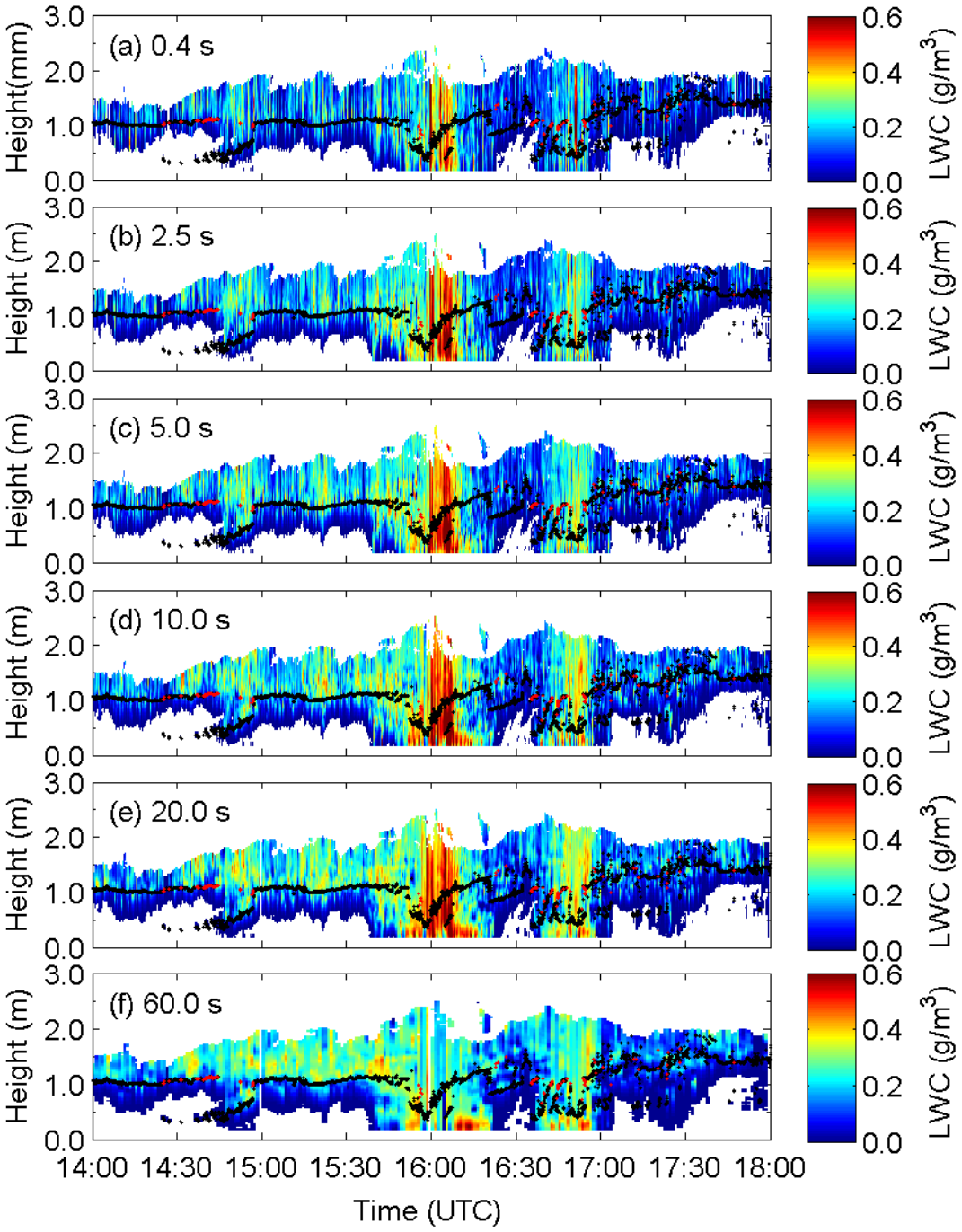

Figure 4.15: Same as Fig. A.1 but for the MAGIC period from 14:00-18:00 UTC on 26 November 2012 with the application of spatial filtering to DFR data. The black and red dotted lines are the first cloud base height and the second cloud base height, respectively, retrieved from Vaisala ceilometer measurements.

Chapter 5

Discussion and Conclusions

The 65 cases listed in Tables 3.1 and 3.2 were selected for this study to represent various cloud types and a large range of cloud LWPs from less than 0.05 mm to greater than 0.30 mm. Because clouds are often thin, potentially mixed phase, and sometimes broken, it can be very challenging to retrieve accurately their LWCs. Top of atmosphere and surface radiative fluxes of cloudy atmospheres are very sensitive to small changes in cloud LWP when the cloud LWP is small so a high degree of accuracy in LWP observations and modeling is needed to study them (Turner et al., 2007). Figure SBI in Turner et al. (2007) shows that the longwave fluxes are most sensitive to LWPs between 0.00 - 0.04 mm and the shortwave fluxes to LWPs from 0.00 mm out to about 0.10 mm. Therefore, for radiation studies LWP accuracies better than 0.01 mm are necessary for cloud LWPs less than 0.04 mm. As cloud LWPs extend beyond 0.04 mm, LWP accuracy requirements become much less severe for the same levels of accuracy in the associated radiation studies. For example, a 0.01-0.02 mm error in LWP for a value near 0.01 mm would be fatal for all radiation studies, but an error of 0.02-0.04 mm for a cloud LWP around 0.1 mm might be tolerable for many radiation studies.

The histogram in Fig. 4.5 shows the frequency of occurrence of differences between radar- and MWR-retrieved LWPs for all 65 cases. Huang et al. (2009) did a similar study using older ARM program radars that arrived at similar results for a single SGP case study period on 6 May 2006 (see their Fig. 1e). As both Huang et al. (2009) and our results indicate, the differences between radar- and MWR-retrieved LWPs generally fall between ± 0.3 mm. Interestingly, radar-

retrieved LWPs are biased high by 0.070 mm in Huang et al. (2009), whereas in our study they are biased low by 0.060 mm. Inspecting the frequency of occurrences of the radar- and MWR-retrieved LWP differences versus MWR-retrieved LWPs in Figs. 4.7-4.12, we find that the range of radar-retrieved LWP errors from low to high LWPs is approximately constant at 0.12 mm but with errors in radar-retrieved LWPs that move from a positive bias at low LWPs to a negative bias at large LWPs. These results suggest that the accuracies of radar-retrieved LWPs are not sufficient for radiative transfer studies at low LWPs but that they may be for some radiation studies at high LWPs.

The frequency of occurrence histograms (Figs. 4.6-4.12) of the radar- and MWR-retrieved LWP differences for the nine case study periods are similar to those for all 65 cases, demonstrating that the nine case study periods exhibit similar radar-retrieved LWP characteristics to all 65 case study periods. Therefore, we focus our detailed analysis on the nine four-hour case study periods and draw conclusions about radar retrieval algorithm performance from them.

5.1 Dual-frequency Radar Cloud LWC Retrieval Algorithm Performance

Over the nine case study periods, there were two times when significant precipitation reached the surface just before or during the times of the radar retrievals: the 20-min period centered on 16:00 UTC 26 November 2012 during MAGIC and throughout the period from 14:00-17:00 UTC 2 April 2013 at the SGP site. During both periods the MWR-retrieved LWPs are significantly higher than those from the radar retrieval. These high MWR-retrieved values are most likely the result of water on the MWR antenna window and are not to be trusted. The slow decay in the MWR-retrieved LWP from 16:00-16:07 UTC (Fig. 5.1b) is what one would expect for a MWR window that has liquid water on it that is slowly evaporating. This is not inconceivable given that the period from 15:50-16:10 UTC has precipitation reaching the surface (Fig. 4.4a,b). During this period both the radar- and MWR-retrieved LWPs may have substantial errors in them but for different reasons as will become clear below. While demonstrating the deleterious effects

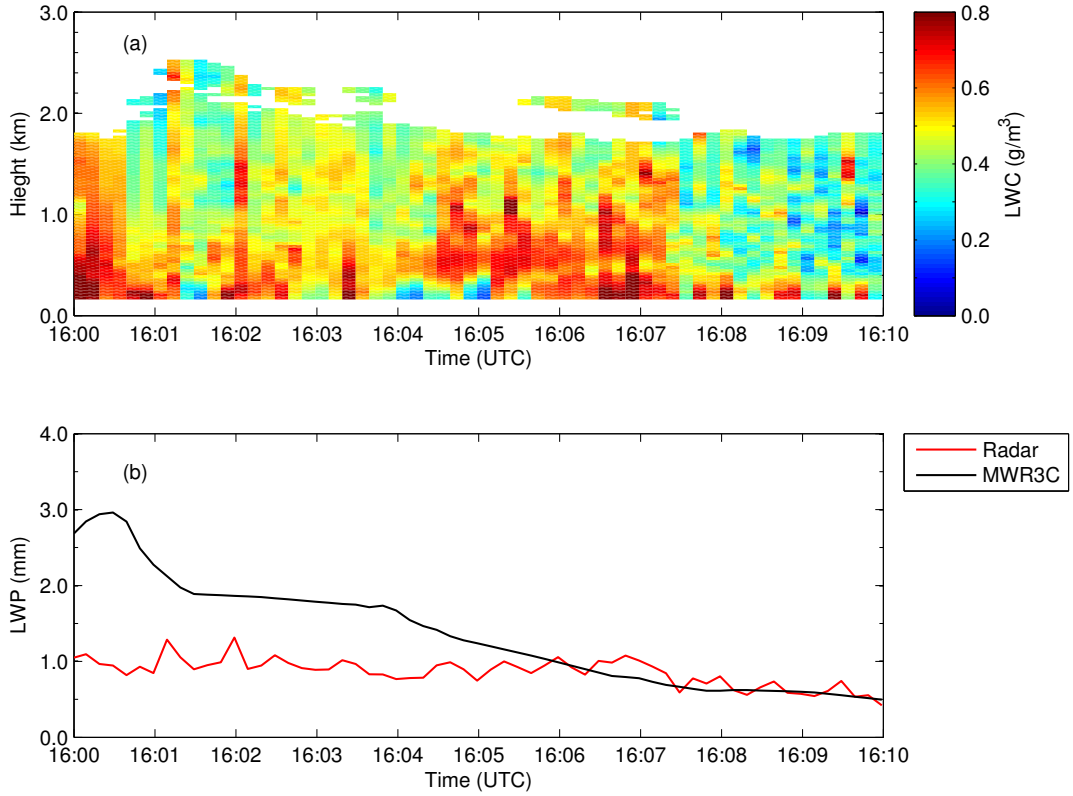

Figure 5.1: (a) LWC profiles from 16:00-16:10 UTC on 26 November 2012 during MAGIC using 10-s time resolution. (b) Radar- and MWR-retrieved LWPs for the same time period as in (a).

of precipitation on MWR LWP retrievals, these two periods are only a small part of the dataset and will not impact significantly our statistical comparisons that incorporate them.

One of the most noticeable features in all of the radar-retrieved LWCs is the common occurrence of high frequency oscillations in radar-retrieved LWPs whose amplitudes decrease with temporal averaging. These high frequency oscillations in the radar-retrieved LWPs are the result of the retrieval operating on noisy radar data. Consider the possibility that beam-pointing differences between the two radars are a possible cause of the high frequency oscillations. During MAGIC, the KAZR was not placed on a stabilized platform, like the MWACR, and rocked with the ship, which caused known beam-pointing differences between the two radars. However, the rocking of the ship during MAGIC leads to imperceptible

changes in LWP compared to those from the retrieval itself. Figures 5.2 and 5.3 show a complete lack of correlation between the high frequency LWP oscillations and rocking of the ship. Therefore, the beam angle offset of the KAZR from the MWACR was not a direct cause of the significant oscillations in the radar-retrieved LWPs. The decrease in amplitudes of the oscillations with increasing temporal averaging of the radar reflectivities can be seen in the second of three consecutive figures in each set of three from Fig. A.1 to Fig. A.27 as the 60-s time resolution results have the smallest amplitude high frequency oscillations. Because the high frequency oscillations in the radar-retrieved LWPs are radar independent but depend on temporal averaging of the radar data, their source lies in the retrieval algorithm itself.

The observed DFR data, here represented as a vertical column of values b at a single time, are used to determine the double-sided constraint in the retrieval algorithm via an a priori estimate of the vertical column of LWC values x_{b}. In the current retrieval x_{b} is taken to be constant with height but with values of zero below cloud base and for heights at which the radar reflectivity factor is below -35 dBZ. To produce x_{b}, the DFR data is first filtered by removing missing data and values in regions of high variability. The values that remain are differenced by subtracting the value at the first height from that at the second height, that at the second from the third, all the way up to the last height. Differences that are below and above minimum and maximum threshold values are set to these values to form a vertical column of values df that are summed to produce a LWP estimate. This LWP estimate is subsequently divided by the number of elements in b to arrive at the fixed LWC values in x_{b}.

The 10-s profiles of observed b (in arbitrary units), df (in the same units as b), first-guess LWC profiles x_{b} (in g m^{-3}), and retrieved LWCs (in g m^{-3}) from 16:01-16:02 UTC on 26 November 2012 during MAGIC are shown in Figs. 5.4. In Fig. 5.4a, x_{b} has a noticeable jump from 0.3-0.4 g m^{-3} at 16:01:00 UTC to more than 0.5 g m^{-3} at 16:01:10 UTC and then down to a value less than 0.5 g m^{-3} at 16:01:20 UTC. The respective LWC profiles jump in a similar fashion leading to an obvious temporal discontinuity in the radar-retrieved LWC profiles. Similar discontinuities in the radar-retrieved LWC profiles and high frequency oscillations in the radar-retrieved LWPs are seen throughout all cases. These first-guess LWC

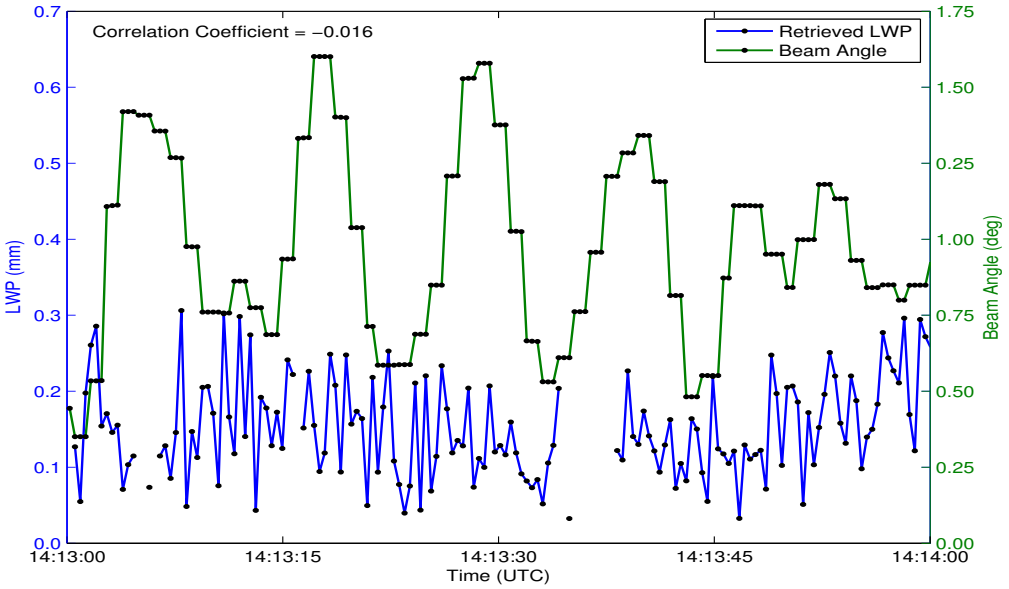

Figure 5.2: Retrieved LWP (in blue) and the beam angle offset of the KAZR from vertical (in green) with each data point plotted in black for the MAGIC case from 14:13-14:14 UTC on 26 November 2012.

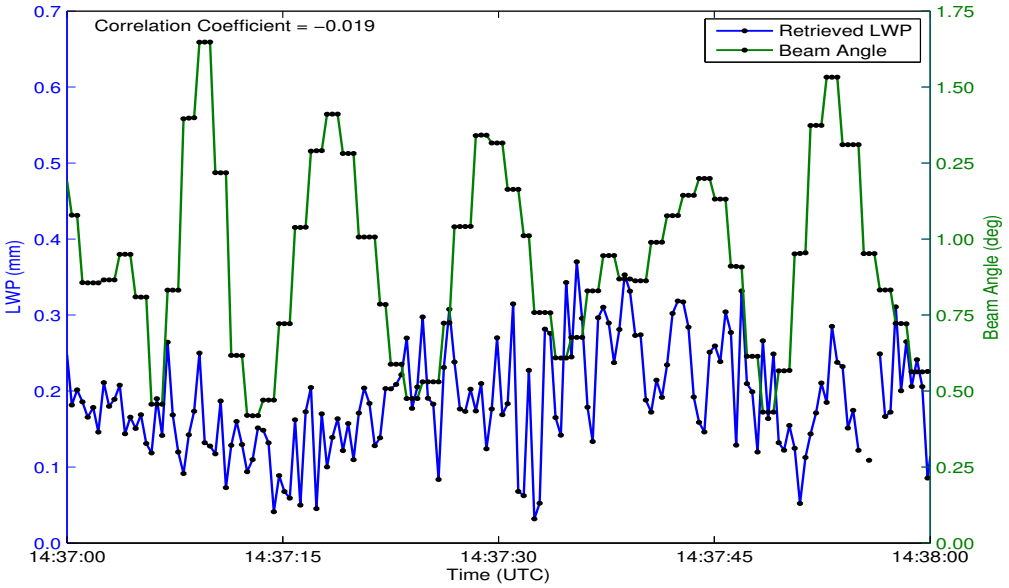

Figure 5.3: Same as Fig. 5.2 but from 14:37-14:38 UTC on 26 November 2012.

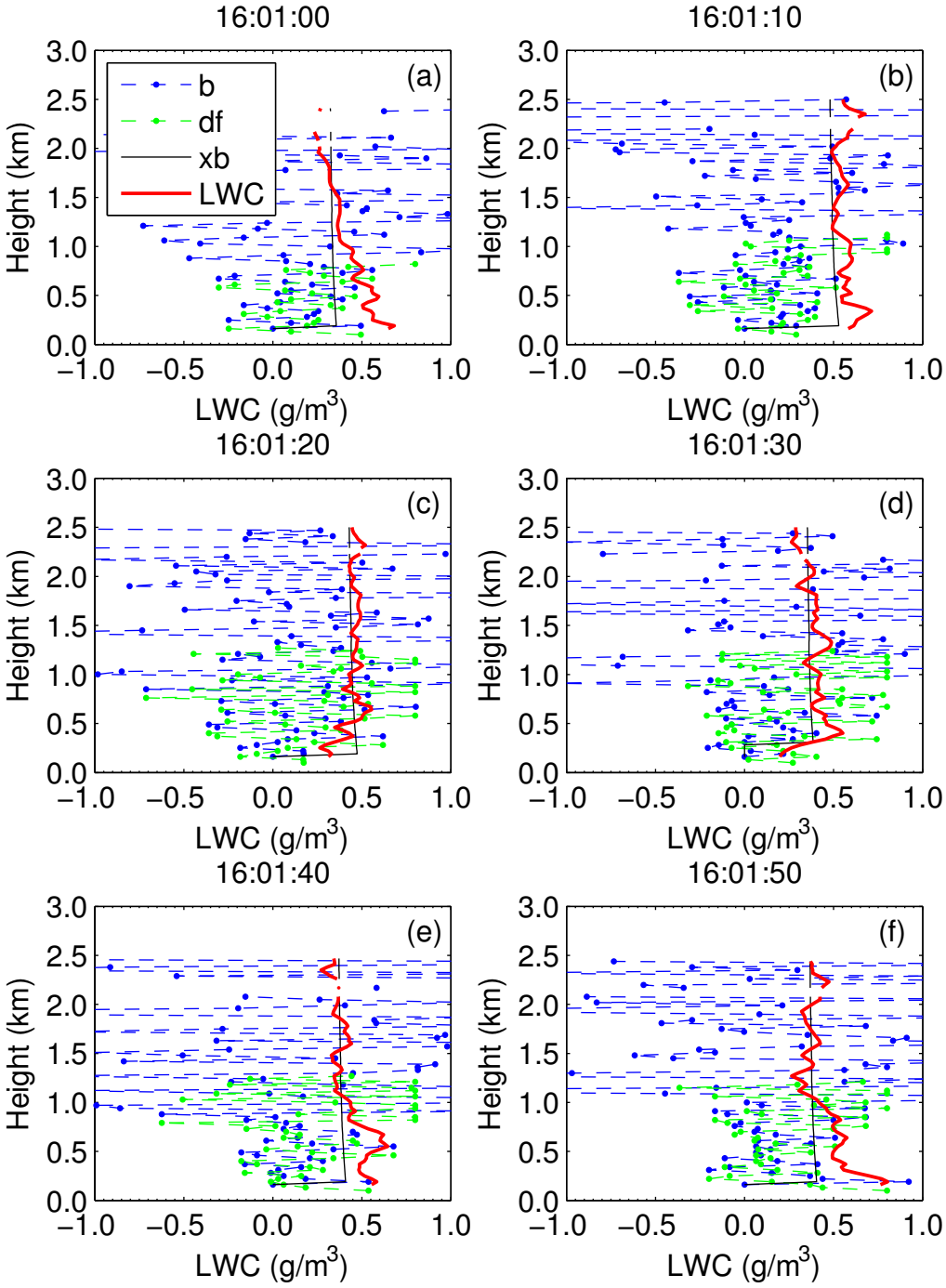

Figure 5.4: The observed b (blue lines), the filtered vector df (green lines), the first-guess LWC profiles x_{b} (black lines), and the retrieved LWCs (red lines) for each 10-s profile from 16:01-16:02 UTC on 26 November 2012 during MAGIC. Note that x_{b} and LWC are expressed in g m^{-3} whereas b and df are expressed in arbitrary units and must be multiplied by $1000/2[\Delta h(\kappa_{95} - \kappa_{35})]$, or approximately 5.21, to convert them to g m^{-3}.

profiles seem to be a strong constraint on the retrieval and significant changes in them from one profile to the next are a main cause of the high frequency oscillations in the radar-retrieved LWPs.

For MAGIC, the magnitudes of the radar-retrieved LWPs generally increase with increasing temporal averaging of the radar reflectivities. This can be seen in the second of three consecutive figures in each set of three from Fig. A.20 to Fig. A.27 as the 60-s time resolution LWP results show the highest values of retrieved LWP. Overall, the radar-retrieved LWPs with the lowest temporal resolution best agree with those from the MWRs. This increasing trend can also be seen in the 10-s, 20-s, and 60-s profiles of b, df, x_{b}, and retrieved LWCs in Figs. 5.5-5.6 as the x_{b} and retrieved LWCs visually increase with decreasing temporal resolution. Calculations of the mean of x_{b} and radar-retrieved LWP at each time resolution from 15:25-15:35 UTC on 26 November 2012 during MAGIC are displayed in Fig. 5.7. Notice that these means exhibit similar features as a function of temporal resolution, indicating that the a priori estimates of the LWC profiles are again exhibiting a strong influence on the retrieved LWC profiles. For this case, averaging of the data before application of the retrieval leads to DFR values that better approximate a monotonically increasing function with height, leading to a concomitant rise in the a priori LWC profile. This is particularly evident in Fig. 5.6d for which the 60-s values of df generally increase with height and the a priori LWCs are the highest of temporal resolutions.

Interestingly, during periods of high reflectivity, temporal averaging of the radar reflectivities actually leads to a decrease in the radar-retrieved LWPs. We attribute this decrease to beam mismatching between the dual-frequency radars leading to different populations of drops within the two beams during periods of spatially heterogeneous precipitation. Beam mismatching can cause large positive and negative swings in the DFR values which average towards zero with temporal averaging in some cases. In these cases information on differential absorption between the two frequencies is lost. This can be seen around 14:00-15:00 UTC in Figs. A.1 - A.3, 13:00-17:00 UTC in Figs. A.10 - A.12, and around 16:00 UTC in Figs. A.22 - A.24. DFR values should always be positive and increase with height if two radar beams are perfectly matched in beam pointing and beam width, as explained in Chap. 2. As such, negative DFR values can either be caused by mismatched beams

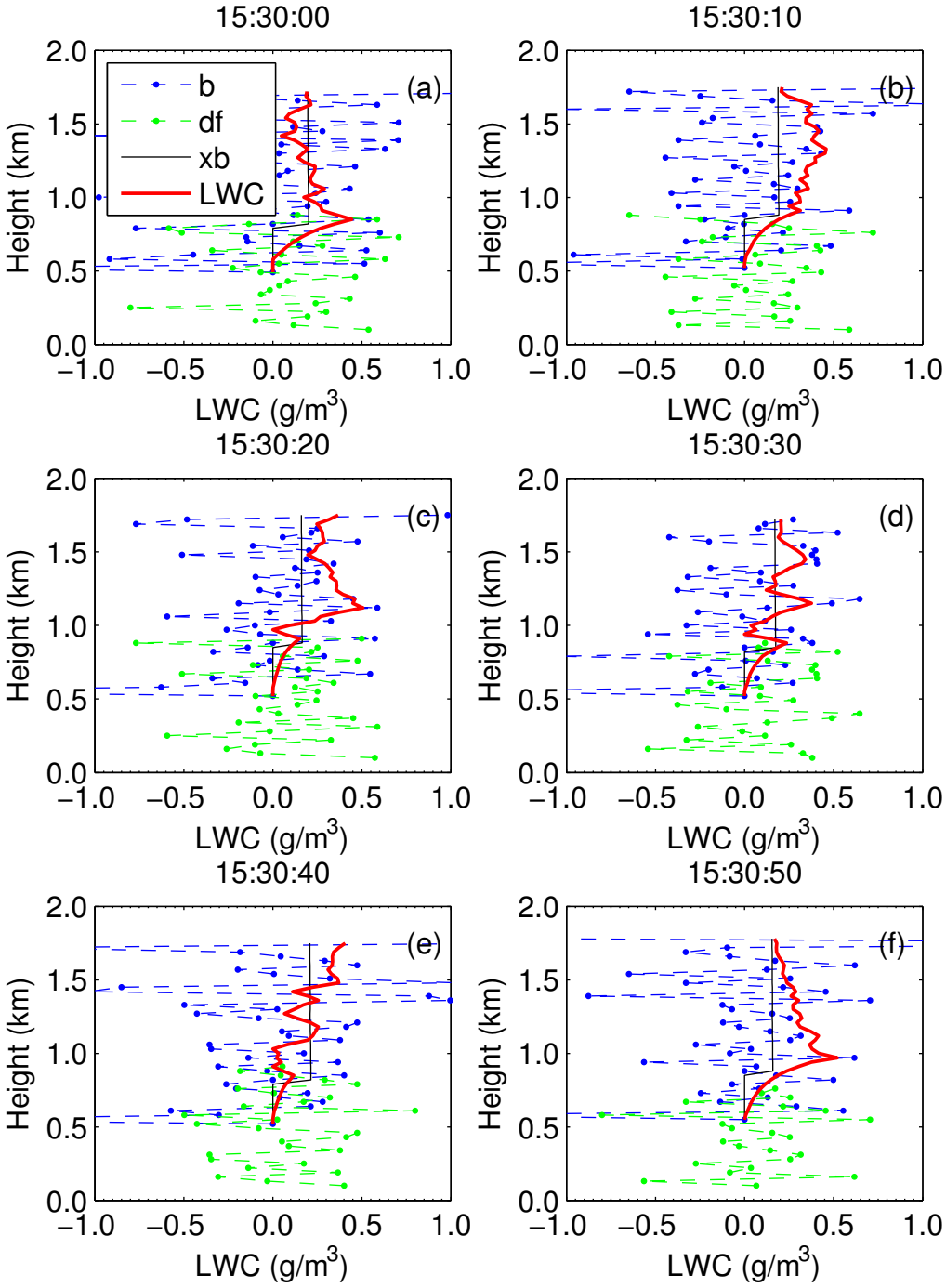

Figure 5.5: Same as Fig. 5.4 but from 15:30-15:31 UTC on 26 November 2012 during MAGIC.

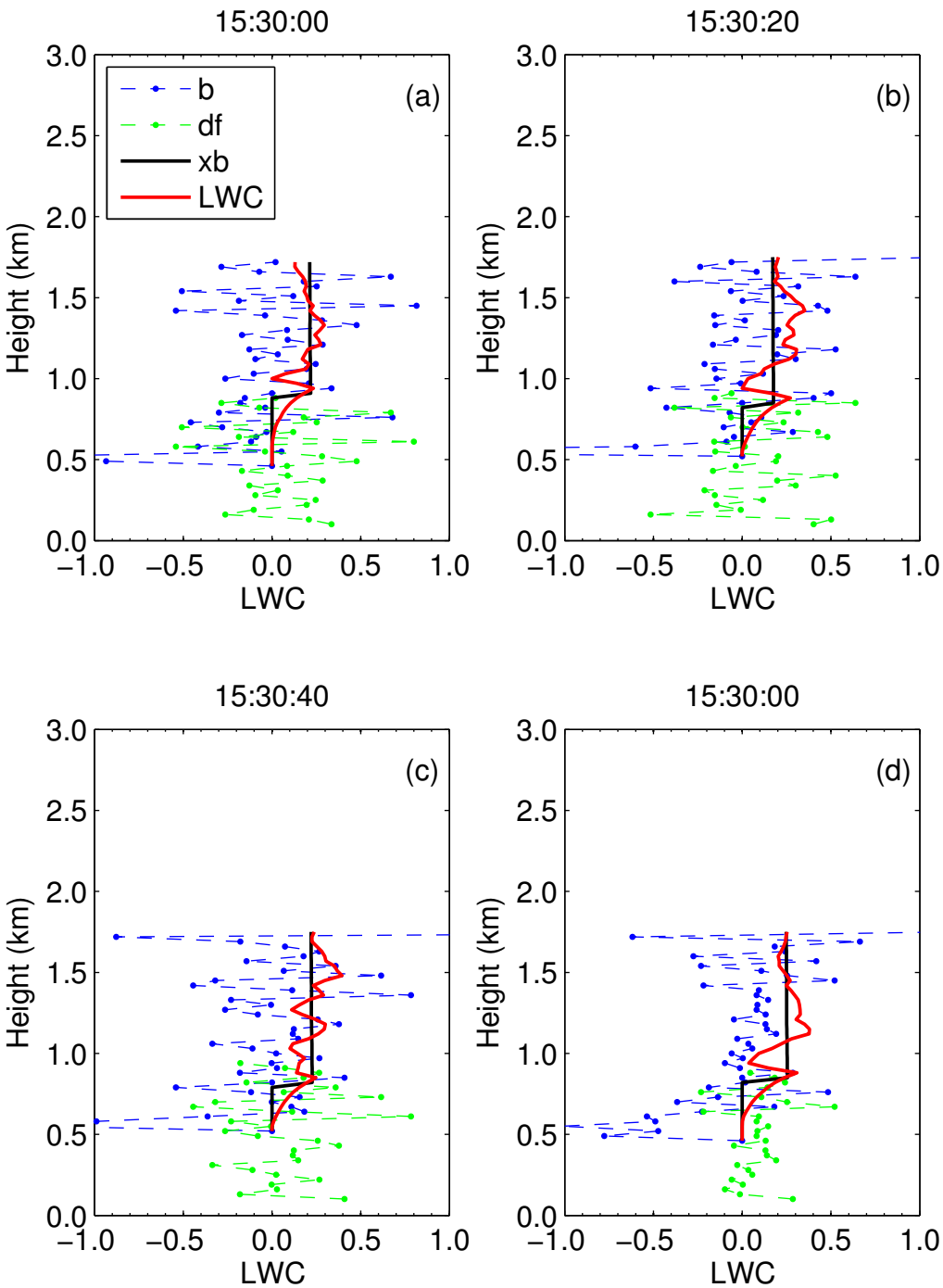

Figure 5.6: Same as Fig. 5.4 but from 15:30-15:31 UTC on 26 November 2012 during MAGIC and for a-c) the 20-s data and d) the 60-s data.

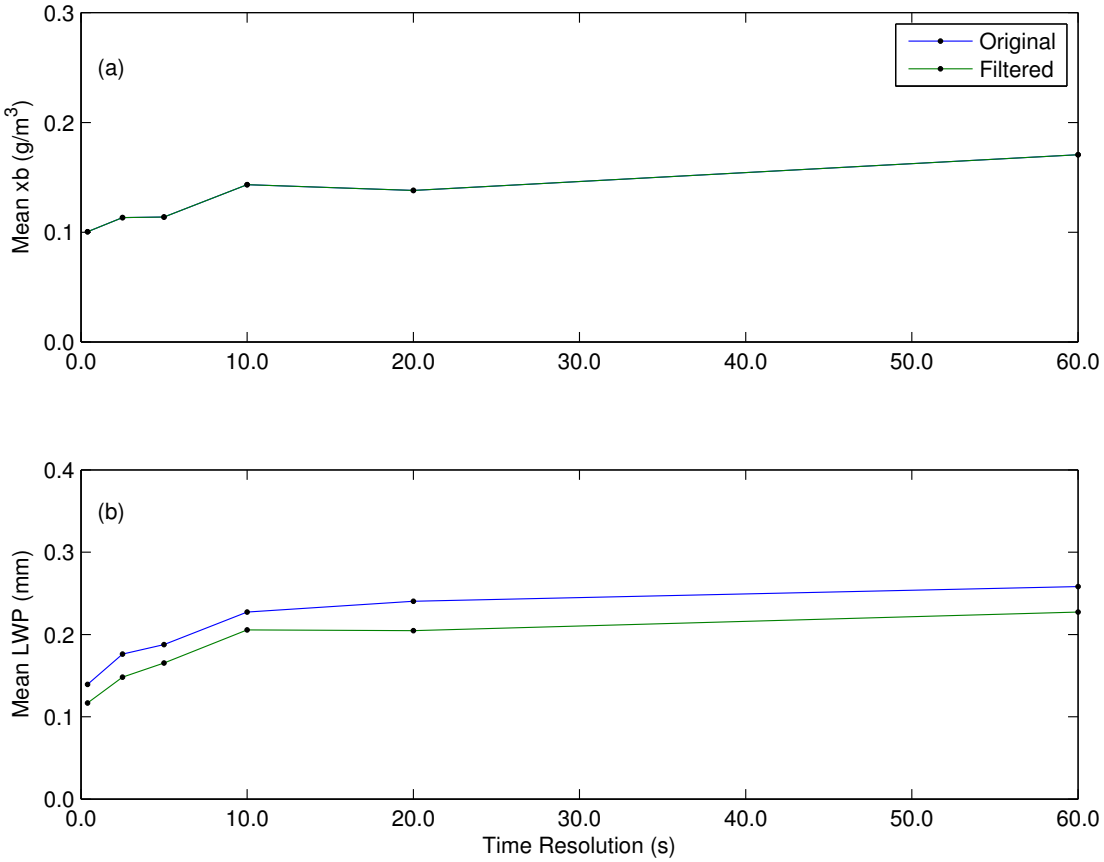

Figure 5.7: (a) Means of the first guess LWC profiles x_{b} and (b) the radar-retrieved LWPs versus temporal resolution for the original (blue) and spatially filtered (green) DFR data from 15:25-15:35 UTC on 26 November 2012 during MAGIC.

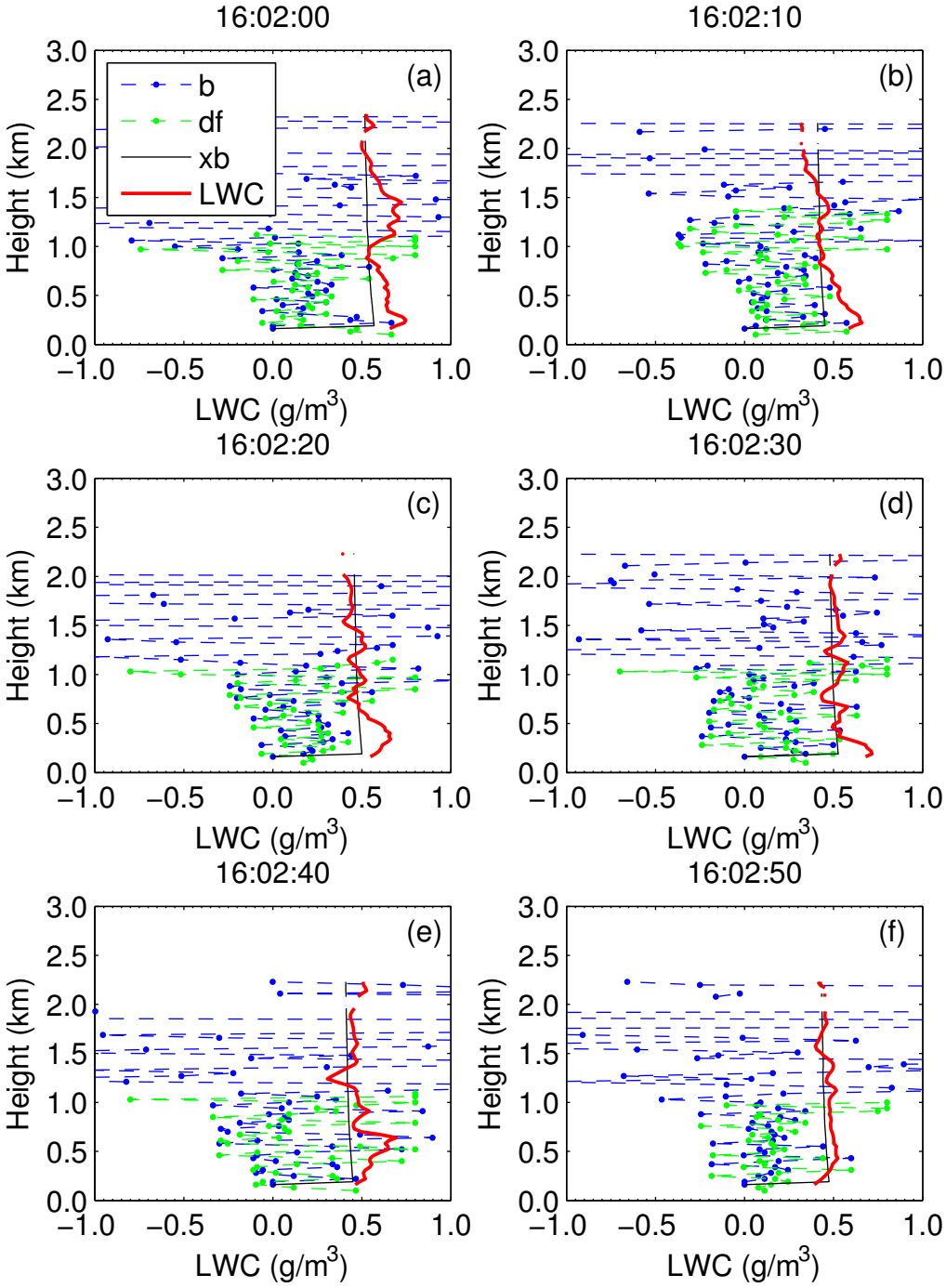

Figure 5.8: Same as Fig. 5.4 but from 16:02-16:03 UTC on 26 November 2012 during MAGIC.

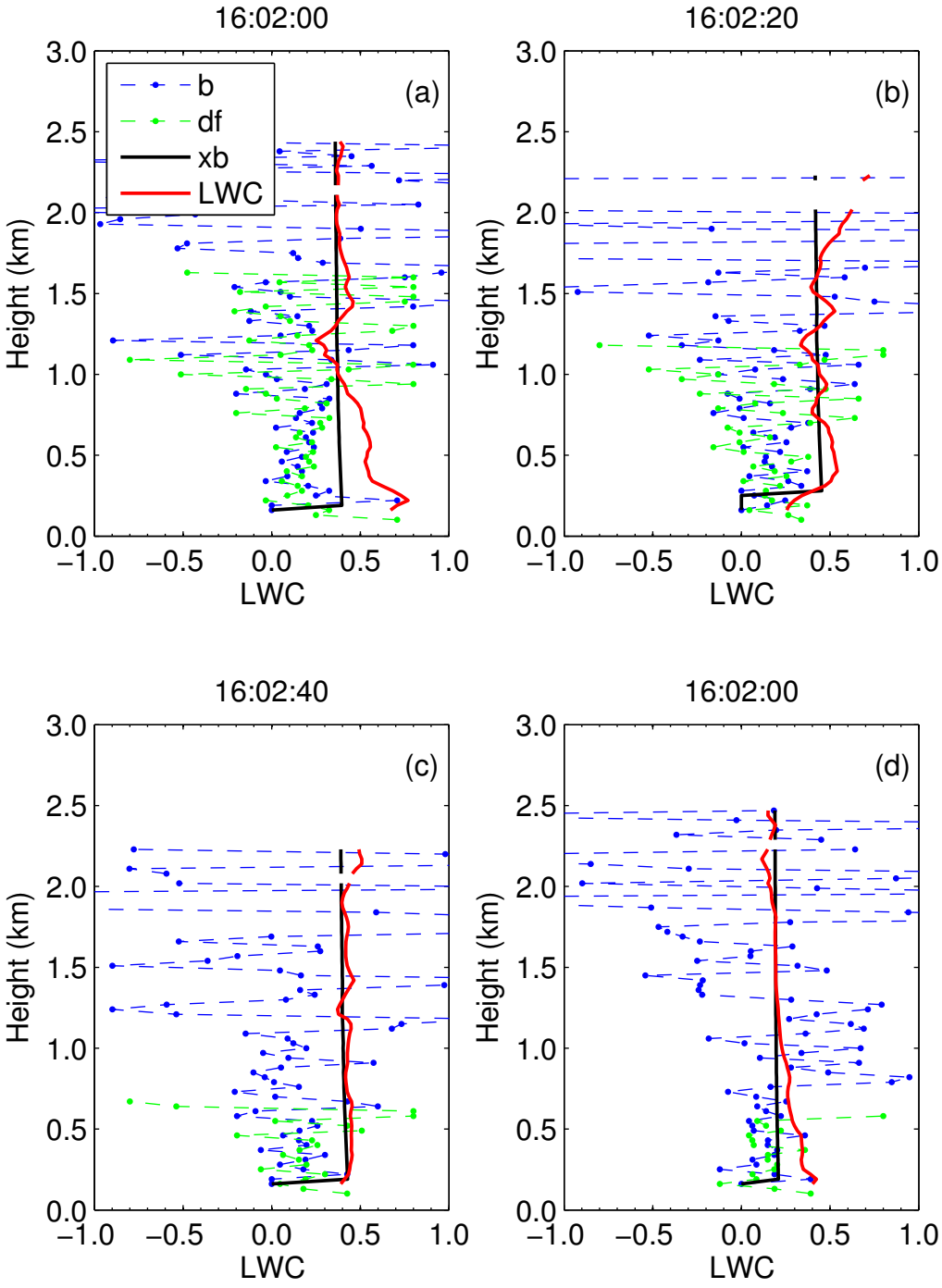

Figure 5.9: Same as Fig. 5.6 but from 16:02-16:03 UTC on 26 November 2012 during MAGIC.

or random fluctuations in the radar noise, with the most egregious negative values caused by beam mismatches. This decreasing trend can also be seen in the 10-s, 20-s, and 60-s profiles of b, df, x_{b}, and retrieved LWCs in Figs. 5.8-5.9 as the x_{b} and retrieved LWCs visually decrease with decreasing temporal resolutions. We illustrate this result further through calculations of mean x_{b} and radar-retrieved LWP at each time resolution from 16:00-16:10 UTC on 26 November 2012 during MAGIC (Fig. 5.10).

The application of spatial filtering to the DFR data increased the correlation between radar- and MWR-retrieved LWPs for all time resolutions during the MAGIC period on 26 November 2012 (Figs. A.28-A.30) but the increases were not substantial. For the ten-minute period from 15:25-15:35 UTC the spatial filtering of the DFR data had little effect on the average x_{b}, whereas the LWPs dropped slightly (Fig. 5.7). During the ten-minute period from 16:00-16:10 UTC these same results are found (Fig. 5.10). These examples are illustrative of the results throughout the entire period.

The LWCs in Figs. 4.14 and 4.15 show that the radar retrieval with and without the application of spatial filtering can, in fact, produce LWC enhancements at cloud base heights identified in Vaisala ceilometer observations. During most drizzling periods for this case, there is a visible increase in LWC at cloud base height and the LWC profiles seem to coincide with the cloud base height measurements reasonably well throughout.

5.2 Sources of Error in the Dual-frequency Radar Cloud LWC Retrieval Algorithm

We have found that the dual-frequency radar cloud LWC retrieval algorithm requires that reflectivity measurements originate from the same target volume and have high precision. If the radars are separated by a measureable distance, have beam pointing errors, beam width differences, or range gate offsets, significant errors can arise as a result that are cloud-type dependent. Despite the pointing differences between the various W- and Ka-band radars used at the SGP and NSA ACRFs, as well as the TCAP and MAGIC AMFs, the radar-retrieved LWPs

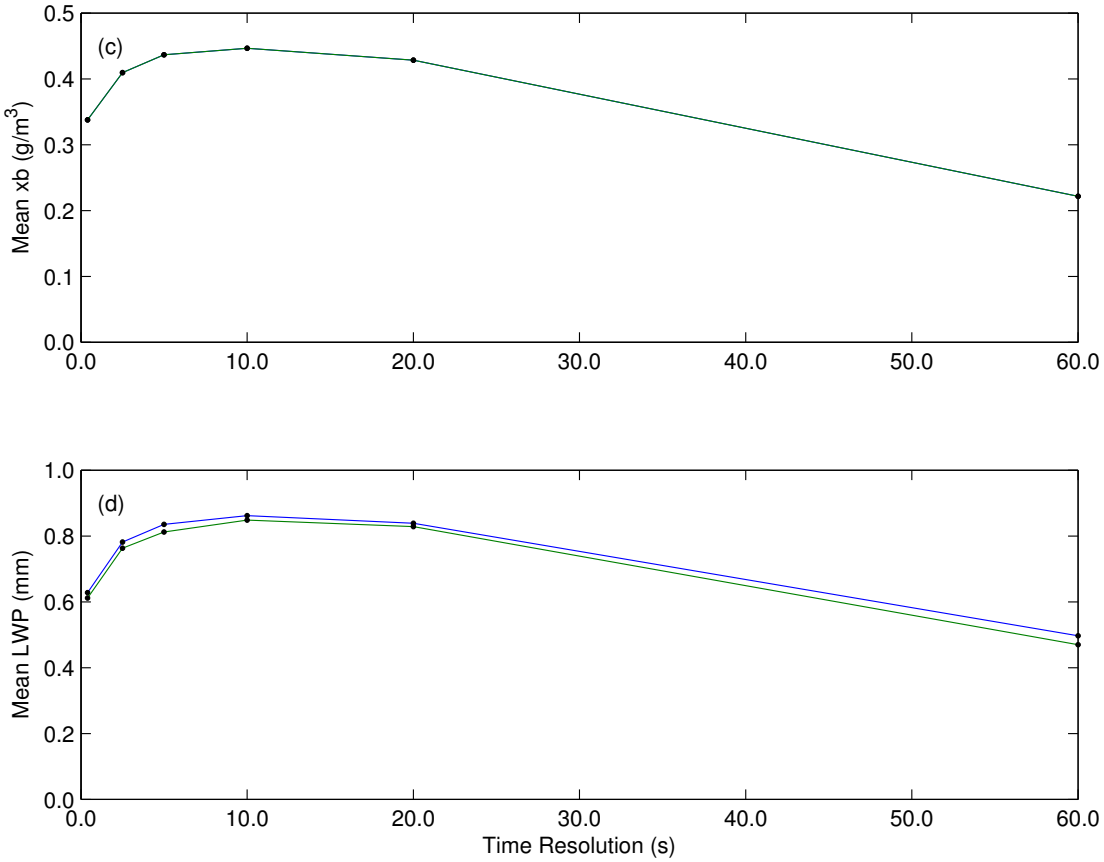

Figure 5.10: Same as Fig. 5.7 but from 16:00-16:10 UTC on 26 November 2012 during MAGIC.

generally have strong correlations with those retrieved from the MWRs, illustrating that there is skill in the radar retrieval. However, to reach accuracies necessary for radiation studies at low LWPs, the beam pointing and beam widths of the radars need to be matched to much higher levels of precision than is currently the case with the DOE ACRF radars.

The radar retrieval is dependent on air temperature, relative humidity, and pressure obtained from SONDEs at each ARM facility. Because SONDE data were not often available at the exact time of each radar profile in the current data set, errors arise from estimating these quantities at one time from measurements at other times. We utilize gas absorption models and liquid water absorption models comparable to those used in MWR retrievals of LWP in the radar retrieval of LWC. Therefore, these models do not play a significant role in creating differences between radar- and MWR-retrieved LWPs. The beam widths of the MWRs and the radars differing by more than a factor of 10 and we are uncertain as to the contribution of this difference to the results that we obtained.

Chapter 6

Summary and Future Work

Proper characterization of the impact of clouds on global climate requires accurate quantification of cloud microphysical and radiative properties, including the two key cloud microphysical parameters of cloud liquid water content and cloud liquid water path. Reliable retrievals of cloud liquid water path have increased in accuracy with the deployment of the new three-channel microwave radiometers at the Atmospheric Radiation Measurement program Climate Research Facilities around the world. However, cloud liquid water content retrievals remain uncertain and unreliable, even though many methods have been developed in retrieving these values. The current method, the dual-frequency radar cloud liquid water content retrieval algorithm, is based on the principle that attenuation of radiation by liquid water drops, provided they are approximately one third or less than the wavelength of the radiation, is directly proportional to the cloud liquid water content and increases with frequency in known ways. Studies by Sekelsky (2000) and Hogan et al. (2005) showed that this method is highly dependent on the accuracy and precision of reflectivity measurements of Ka- and W-band radars.

The retrieval algorithm evaluated here was developed by Huang et al. (2009) and is based on the method proposed by Hogan et al. (2005) but includes total variation regularization techniques, explained in Huang et al. (2008a) and Chap. 2. These techniques are commonly used in image processing and many other applications to decrease variability in noisy data. Huang et al. (2009) showed that these technique decreased retrieved cloud liquid water content uncertainties caused by radar noise without degrading the spatial or temporal resolution of the

retrievals when applied to a single period of data from the Atmospheric Radiation Measurement program Southern Great Plains Climate Research Facility.

We applied the dual-frequency radar retrieval algorithm developed by Huang et al. (2009) to 65 cases spread over about two years and four Atmospheric Radiation Measurement Program Climate Research Facilities. Various temporal and spatial averaging were applied to the observational data before implementing the retrieval and the retrieved cloud liquid water paths were compared to those from microwave radiometers. Of all the different time resolutions tested on the observational data, the temporal resolutions of 10-20 s for the radar reflectivities produced the most accurate results in the comparisons to the microwave radiometer retrievals. These results showed the least variability and cloud liquid water paths closest to those from the microwave radiometers.

The retrieval works to the accuracy stated in Huang et al. (2009) with the retrieved cloud liquid water contents accurate to within 0.10-0.15 g m^{-3}. For radiation studies involving thin clouds with cloud liquid water paths as low as 0.01-0.04 mm, which are nonetheless radiatively important, the current radar retrievals are not sufficiently accurate. Improvements in beam pointing with matched beam widths are perhaps the most easily implemented going forward, though deploying two radars with perfectly matched beam pointing to remote sites is not easy.

Going forward, it is important to develop a better first-guess cloud liquid water content profile to input into the retrieval in order to remove temporal striping from the retrieved cloud liquid water content profiles. Instead of using an algorithm with one first-guess estimate of cloud liquid water content, an iterative algorithm that uses successive estimates of cloud liquid water content profiles as subsequent first-guess inputs to the retrieval would be the next logical step in retrieval development. Huang et al. (2008a) suggested this approach and we think that it is a viable one based on our results. Another possibility is to use the cloud liquid water paths retrieved from the microwave radiometers to build the first-guess profiles. However, this approach would remove the microwave radiometer retrievals as a source of assessment data for the radar retrievals.

More studies should also be done on how spatial filtering of the observational data before applying the retrieval affects the retrievals. We applied a simple smoothing scheme that replaces each DFR data point with the calculated me-

dian of a 3 by 3 box centered on it before applying the retrieval. There was some improvement between these results and those without spatial filtering. Larger spatial averaging or applying this averaging many times should be done and analyzed. Another possibility is to average some number of consecutive retrieved cloud liquid water content profiles while computing the variances in the liquid water contents at each height. These averaged profiles together with their variance as a function of height could then be used as subsequent first-guess profiles in the radar retrieval algorithm.

The major finding of this study is that the a priori profile of cloud liquid water content is a strong constraint on the retrieval. The question that follows is how strongly are the retrieved liquid water contents constrained by the a priori values. To answer this question we recommend that a second set of a priori liquid water content profiles be used to initialize the retrieval. For this second set the liquid water contents are not constant with height within the cloud as for the first set; rather, they follow an adiabatic cloud liquid water content profile from cloud base to cloud top. Both sets of a priori liquid water contents should be used to initialize the retrieval and then the retrieval with each set as an input should be iterated until retrieved liquid water contents are obtained. If the retrieved liquid water contents obtained from these two different sets of a priori constraints are more similar to each other than their a priori estimates, then the retrieval would not be overly constrained by these a priori estimates. However, if the retrieved cloud liquid water contents obtained from these two different sets of a priori constraints are more similar to their a priori estimates than to each other, then perhaps the retrieval is overly constrained by the a priori estimates, leaving additional, unquantified uncertainties in the retrieved values.

Finally, given that we see many negative DFR values from the Ka- and W-band radar pairs, particular attention must be paid to matching beam pointing and beam widths of the radars that form a pair. The new DOE ARM program Scanning ARM Cloud Radars 2nd generation (SACR2s) slated to be deployed at Oliktok Point and the Azores in the near future are critical to future radar retrievals of cloud liquid water contents. Enhancements in regards to matched beam pointing, matched beam widths, and matched collection of samples in time and height should lead to markedly improved cloud liquid water content profiles retrieved using the Huang

et al. (2009) retrieval algorithm. Once reliable cloud liquid water contents can be retrieved, more accurate radiation closure studies may be performed, leading to further improvements in observed and modeled estimates of cloud and radiation interactions.

Appendix A

Figures

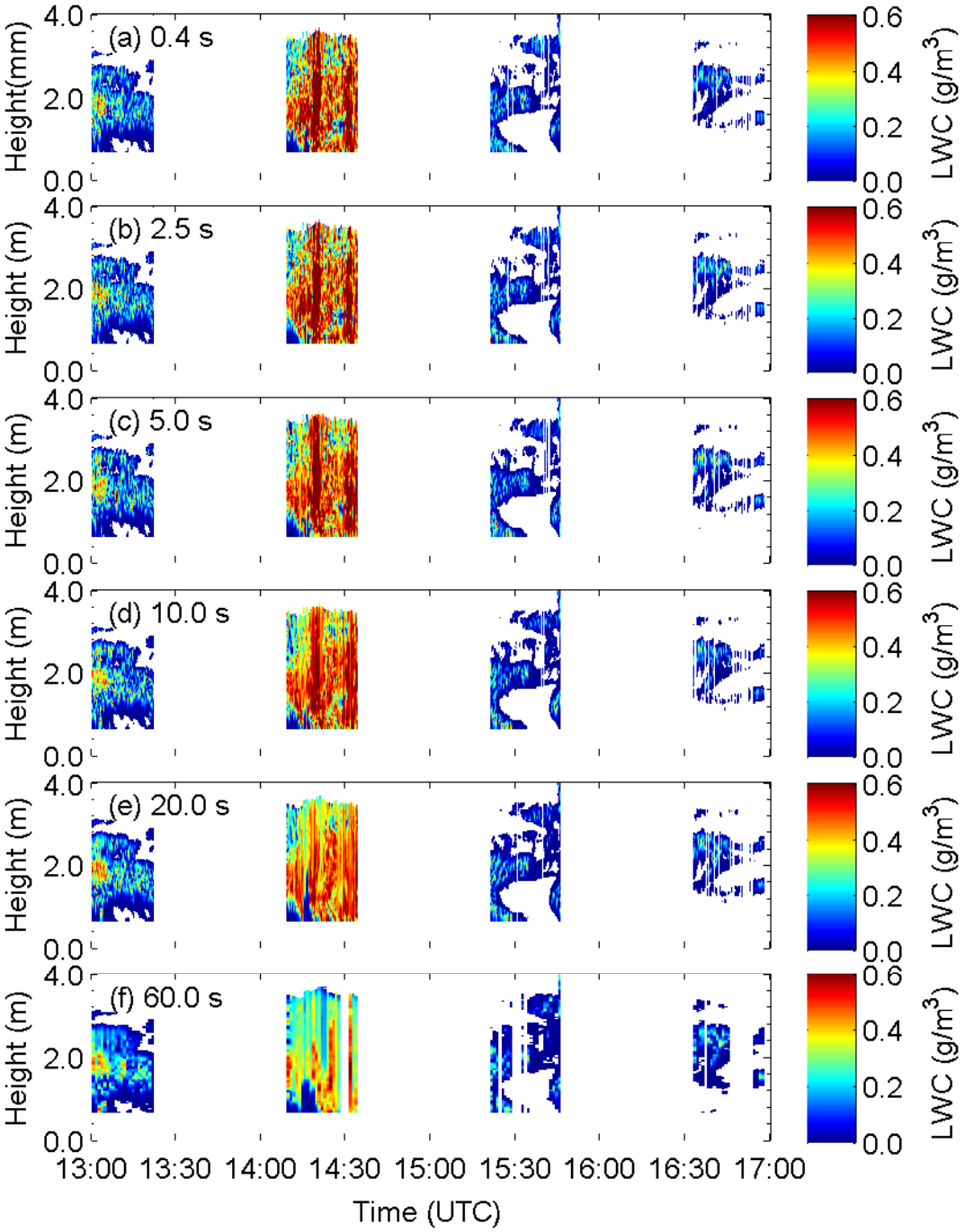

Figure A.1: TCAP LWC fields for the case study period from 13:00-17:00 UTC on 4 September 2012.The black and red lines are the MWR-retrieved LWPs and radar-retrieved LWPS, respectively.

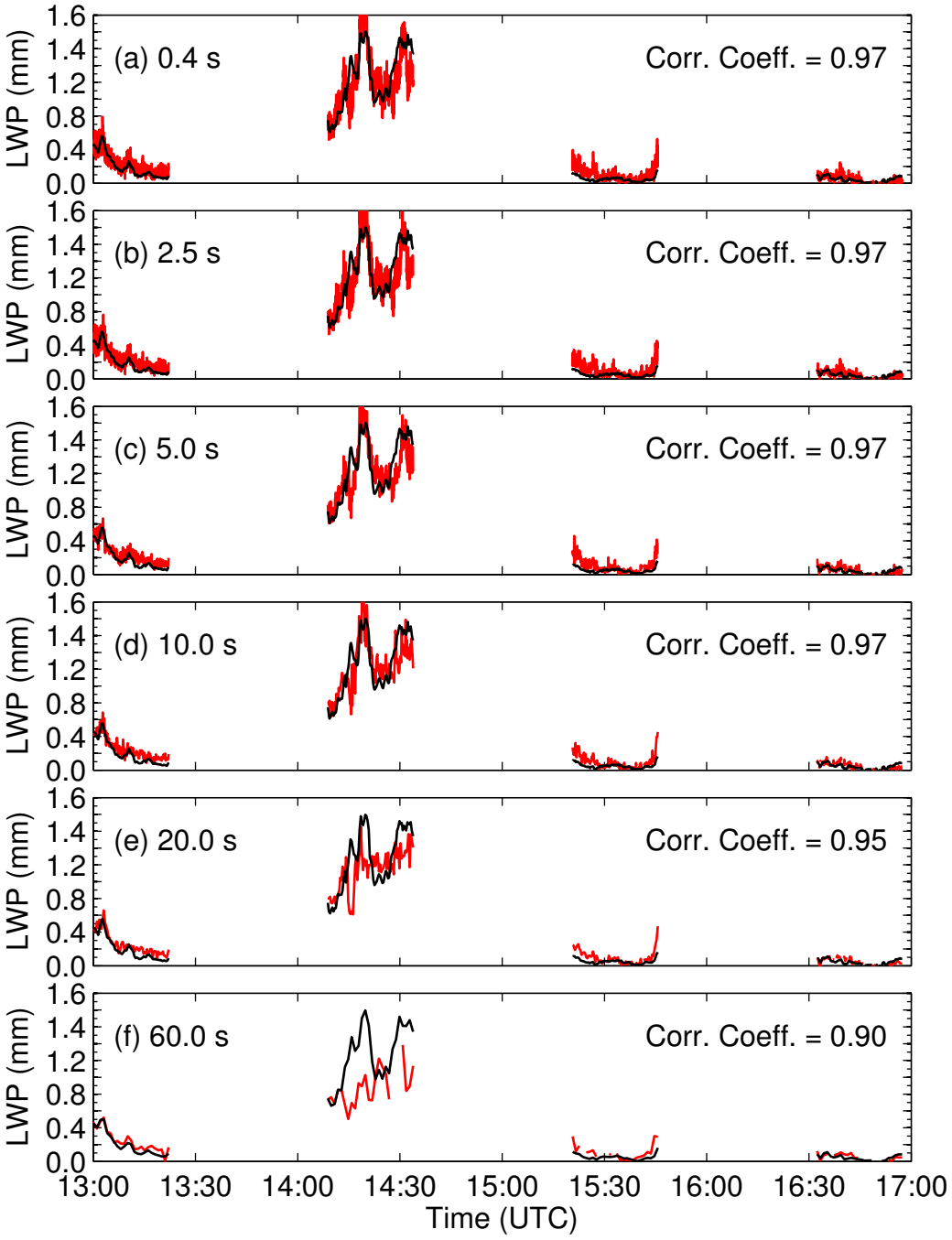

Figure A.2: TCAP time series of radar- and MWR-retrieved LWPs for the case study period from 13:00-17:00 UTC on 4 September 2012.

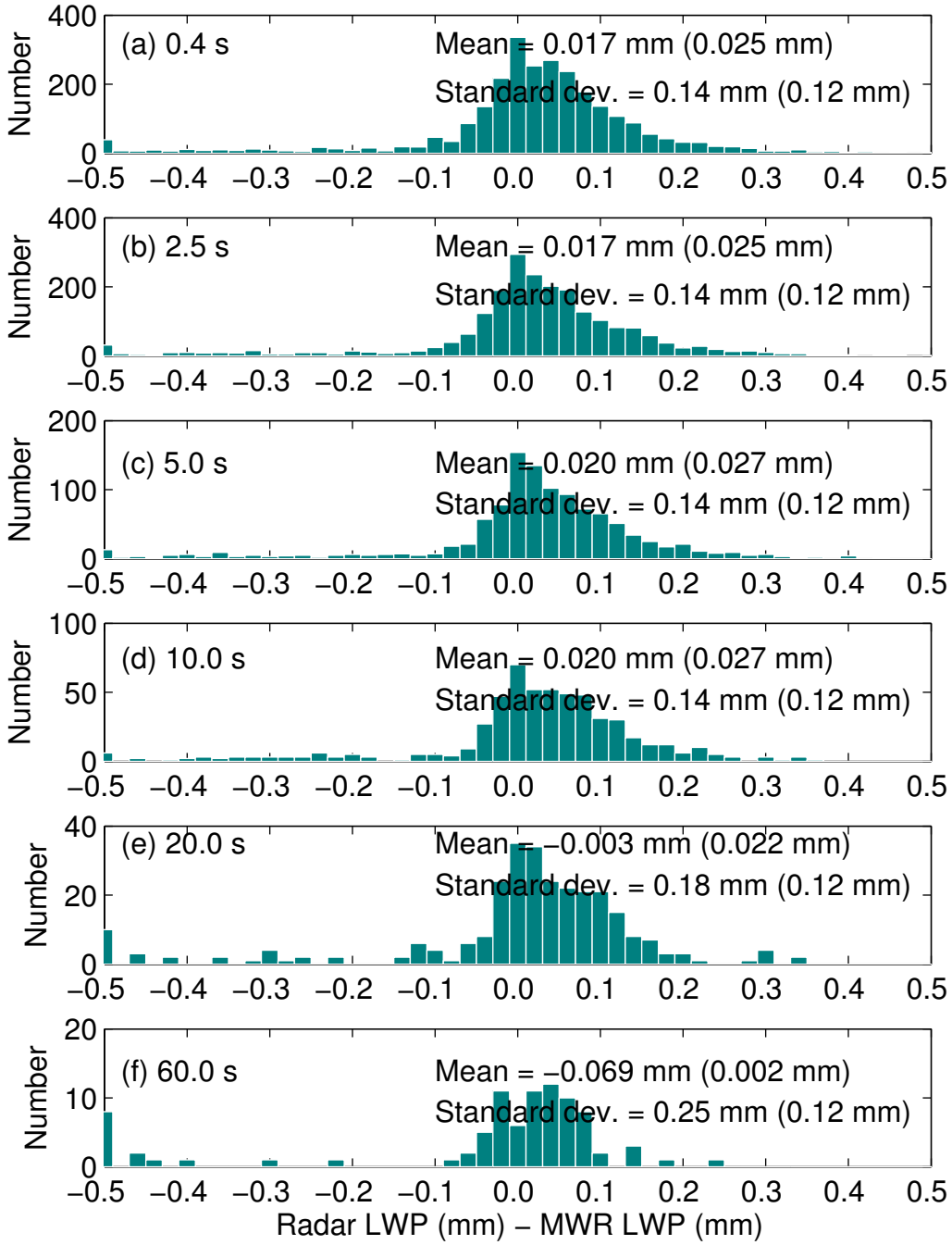

Figure A.3: TCAP histogram of differences between the radar- and MWR-retrieved LWPs for the case study period from 13:00-17:00 UTC on 4 September 2012.

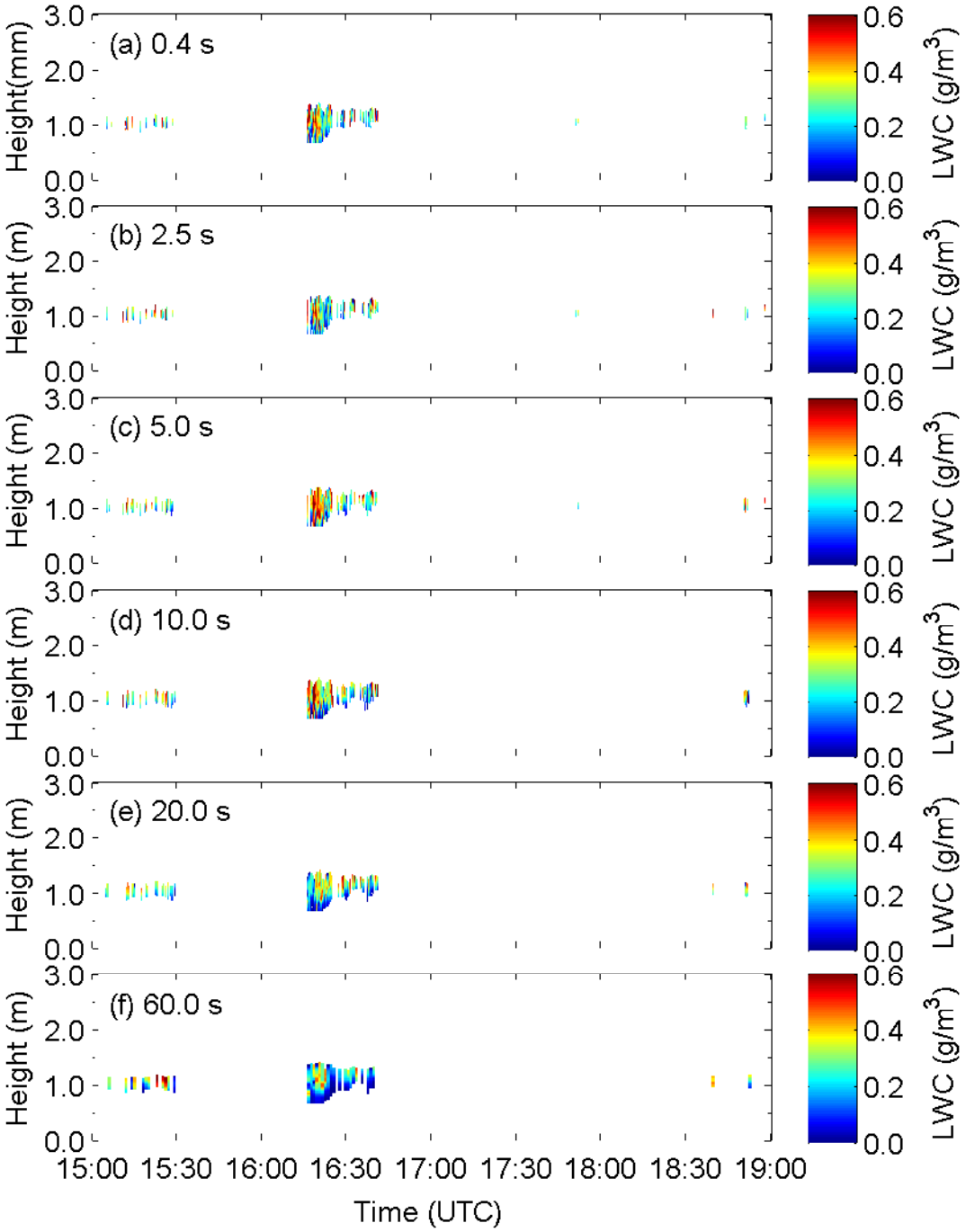

Figure A.4: Same as Fig. A.1 but for the TCAP period from 15:00-19:00 UTC on 14 November 2012.

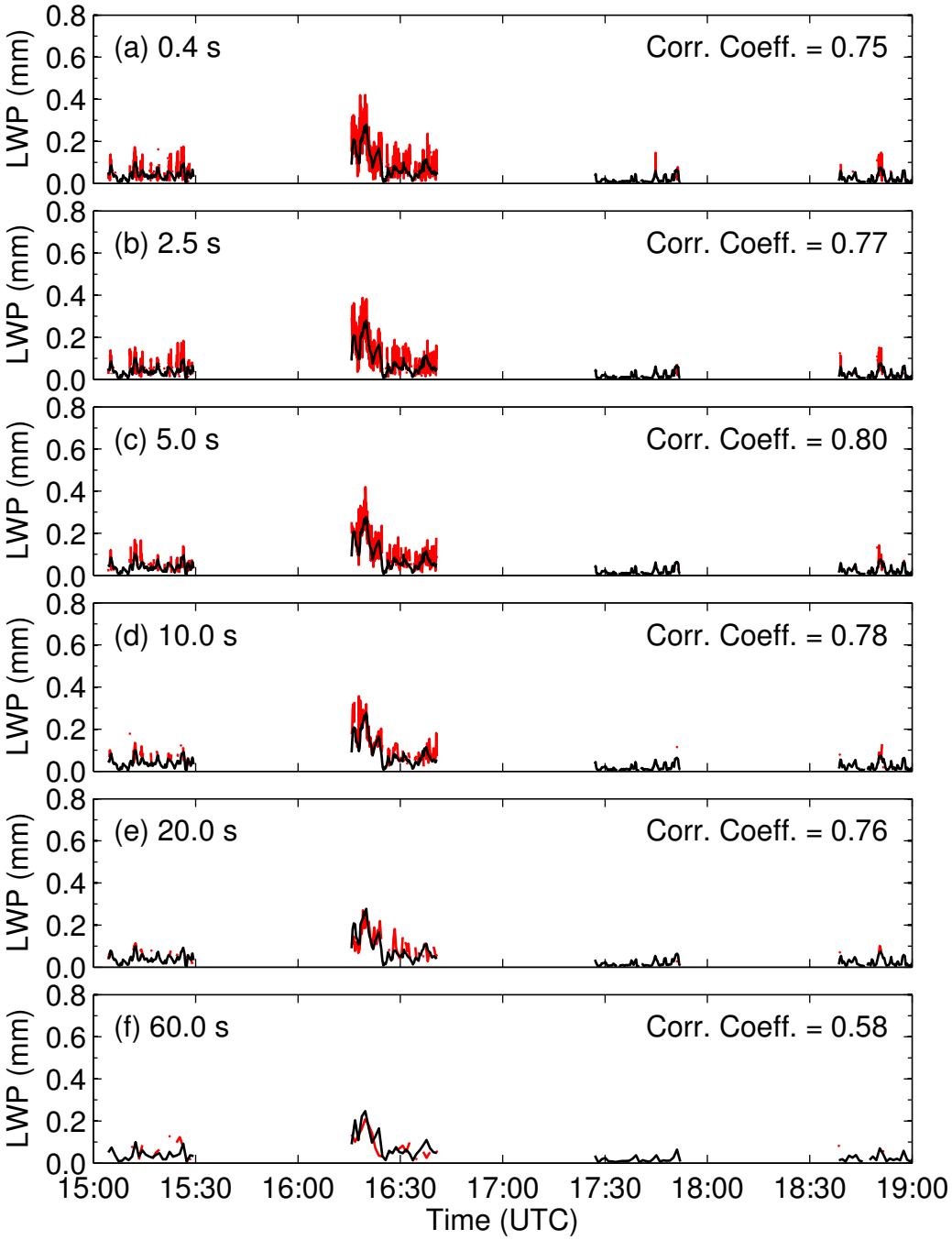

Figure A.5: Same as Fig. A.2 but for the TCAP period from 15:00-19:00 UTC on 14 November 2012.

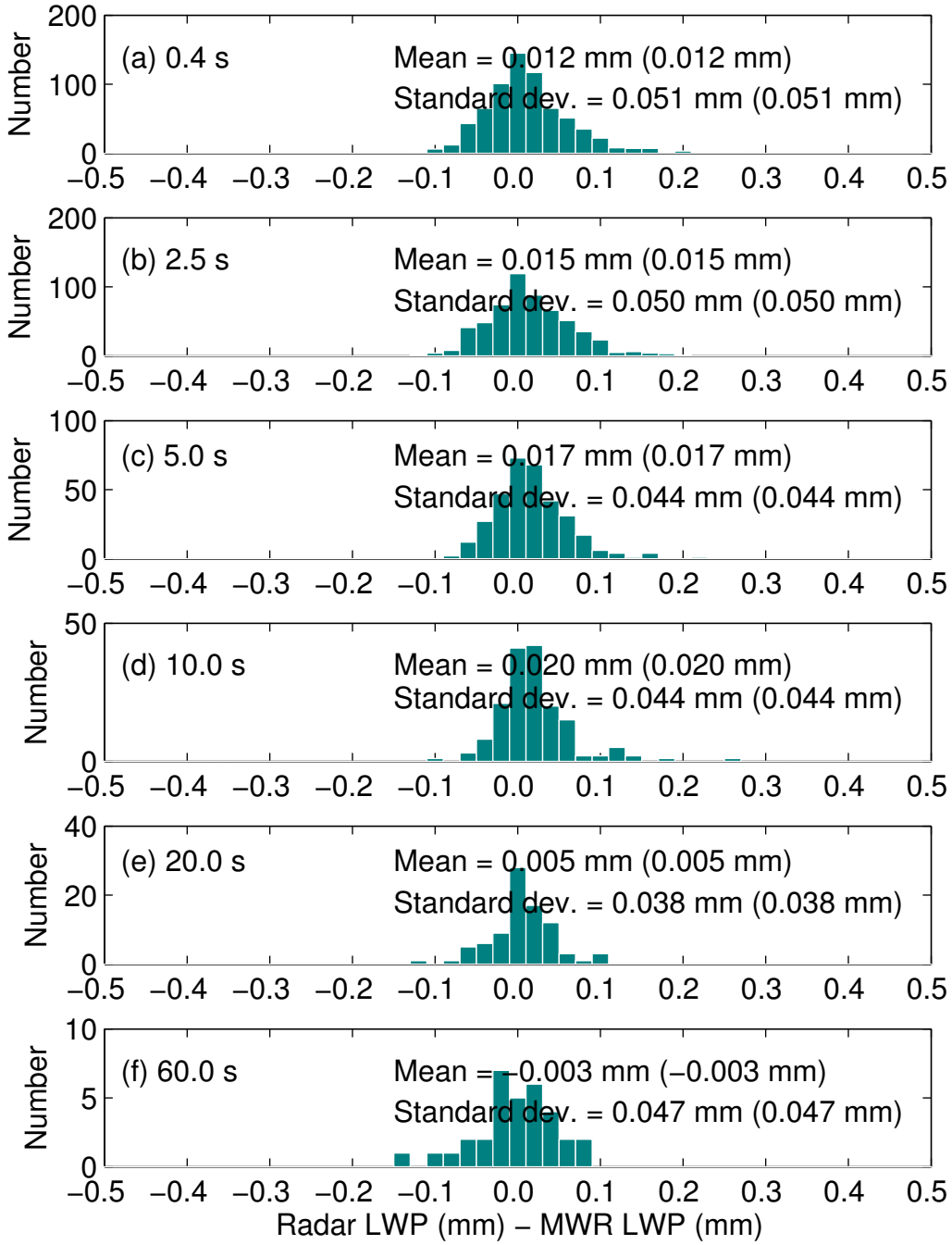

Figure A.6: Same as Fig. A.3 but for the TCAP period from 15:00-19:00 UTC on 14 November 2012.

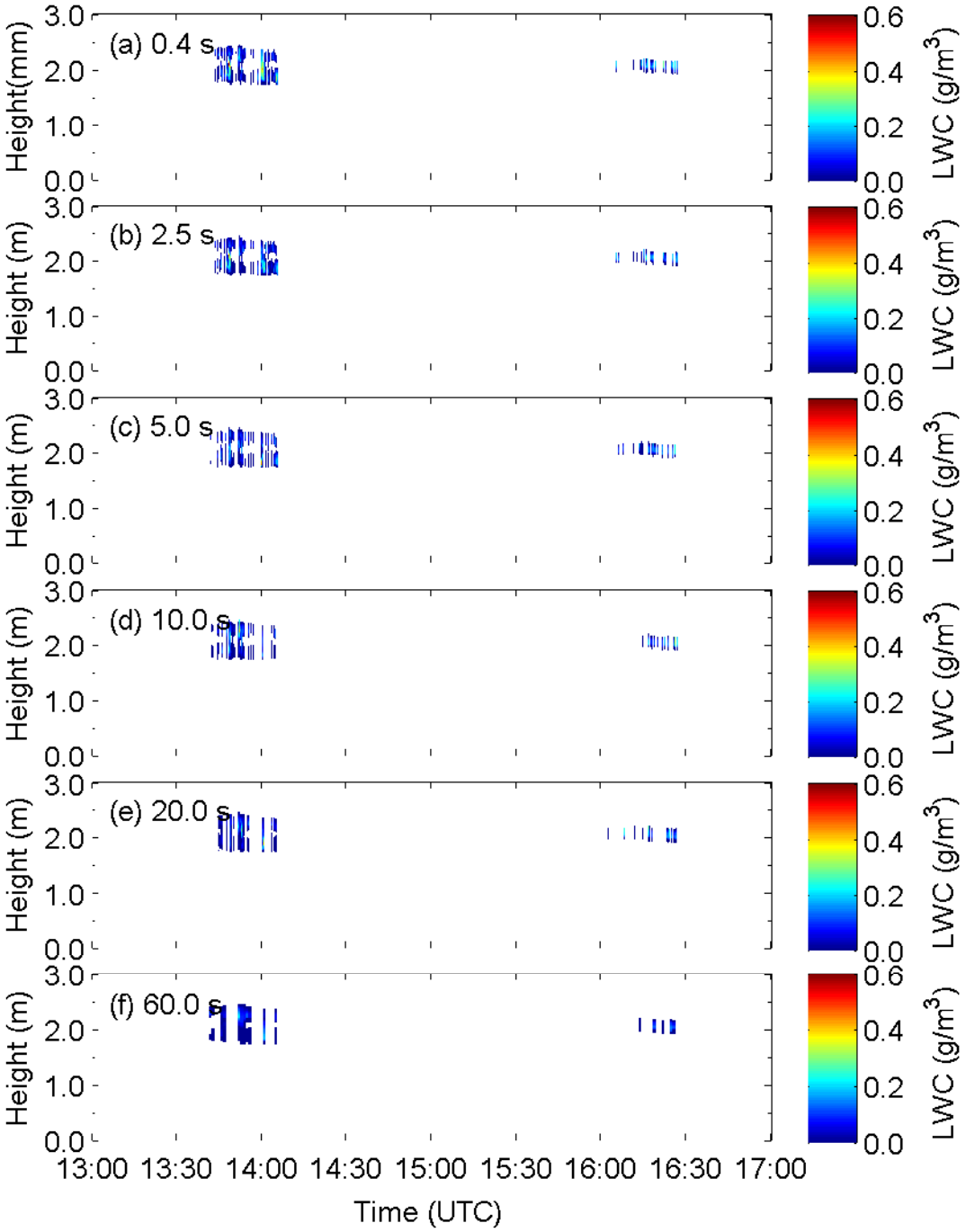

Figure A.7: Same as Fig. A.1 but for the SGP period from 13:00-17:00 UTC on 5 October 2012.

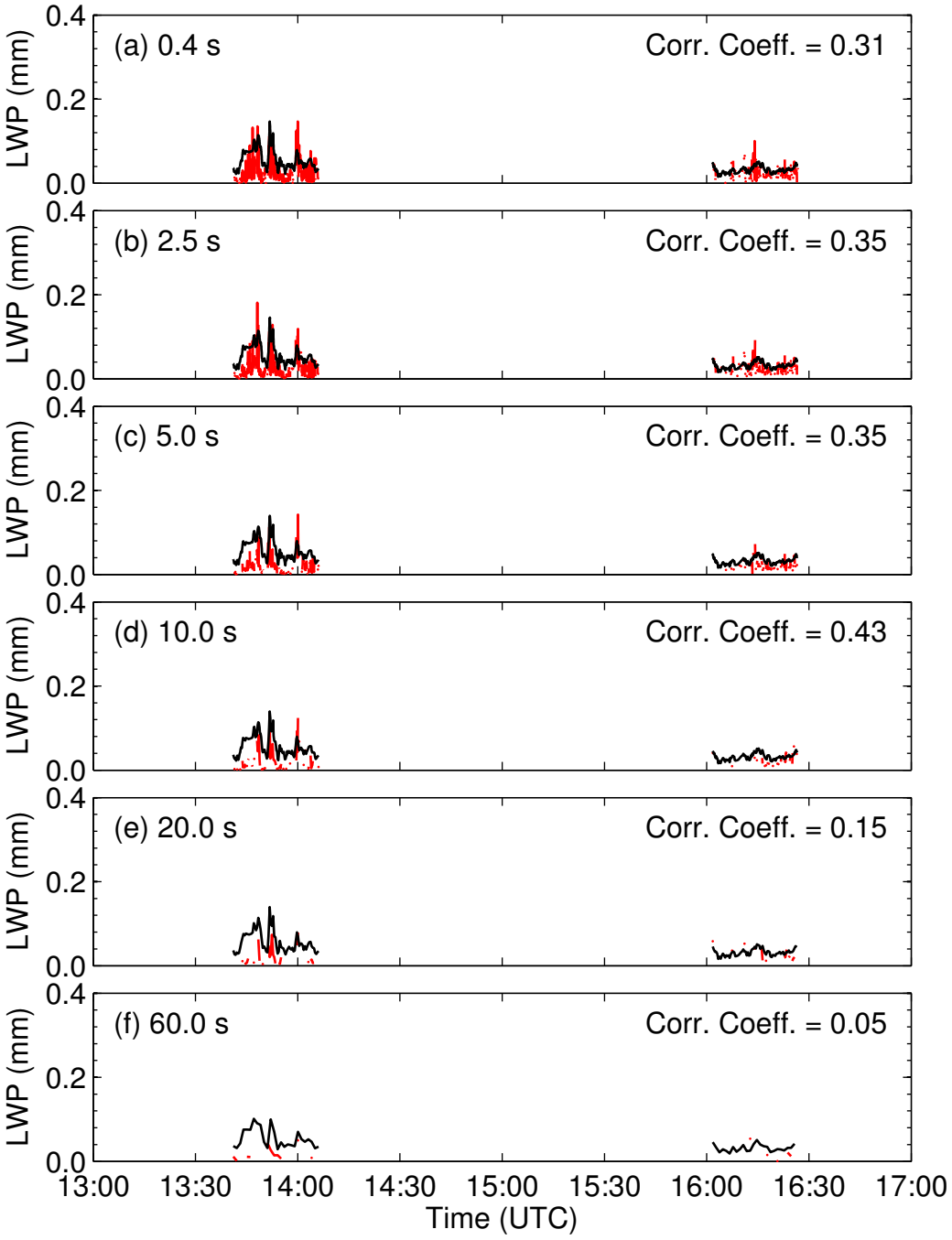

Figure A.8: Same as Fig. A.2 but for the SGP period from 13:00-17:00 UTC on 5 October 2012.

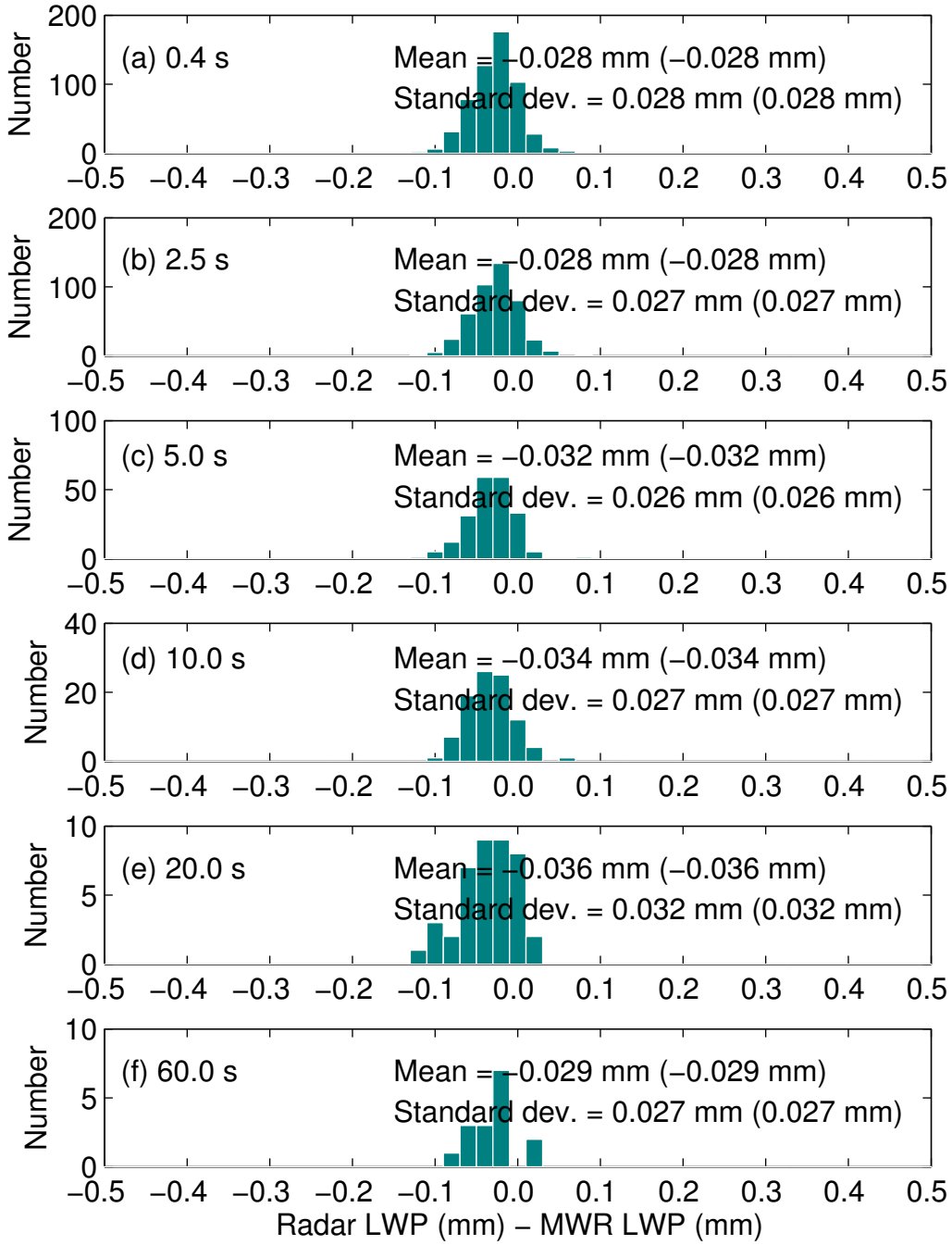

Figure A.9: Same as Fig. A.3 but for the SGP period from 13:00-17:00 UTC on 5 October 2012.

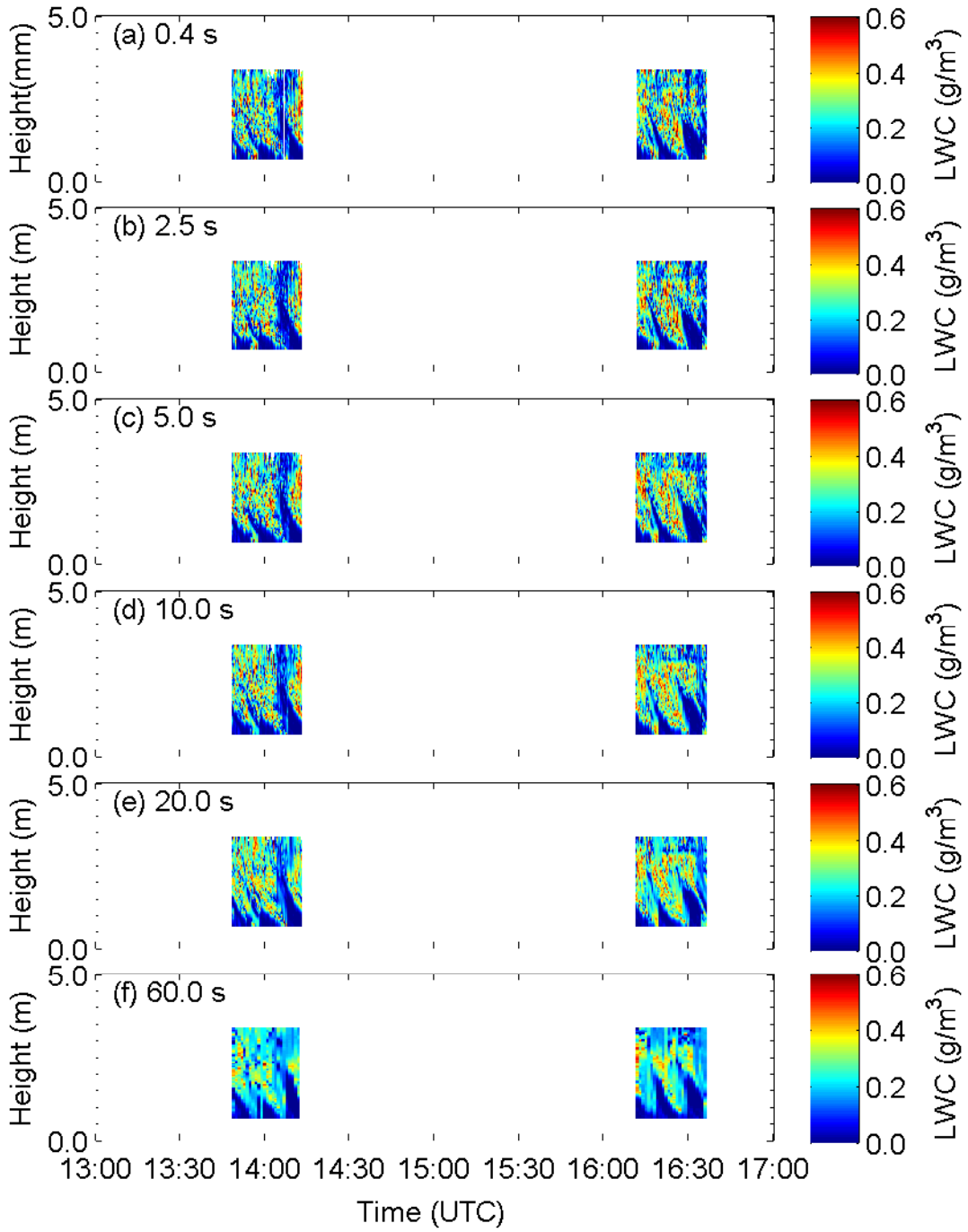

Figure A.10: Same as Fig. A.1 but for the SGP period from 13:00-17:00 UTC on 2 April 2013.

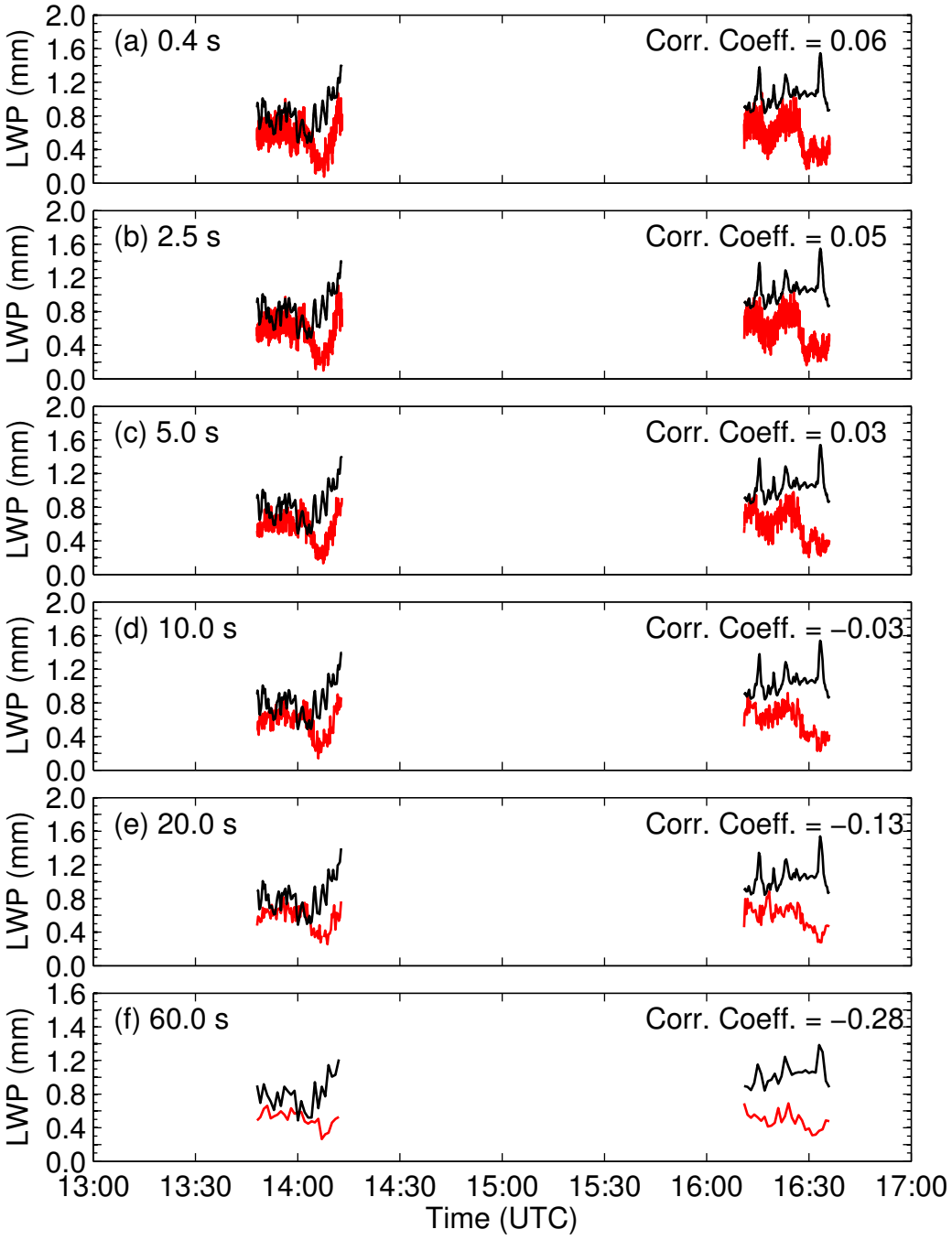

Figure A.11: Same as Fig. A.2 but for the SGP period from 13:00-17:00 UTC on 2 April 2013.

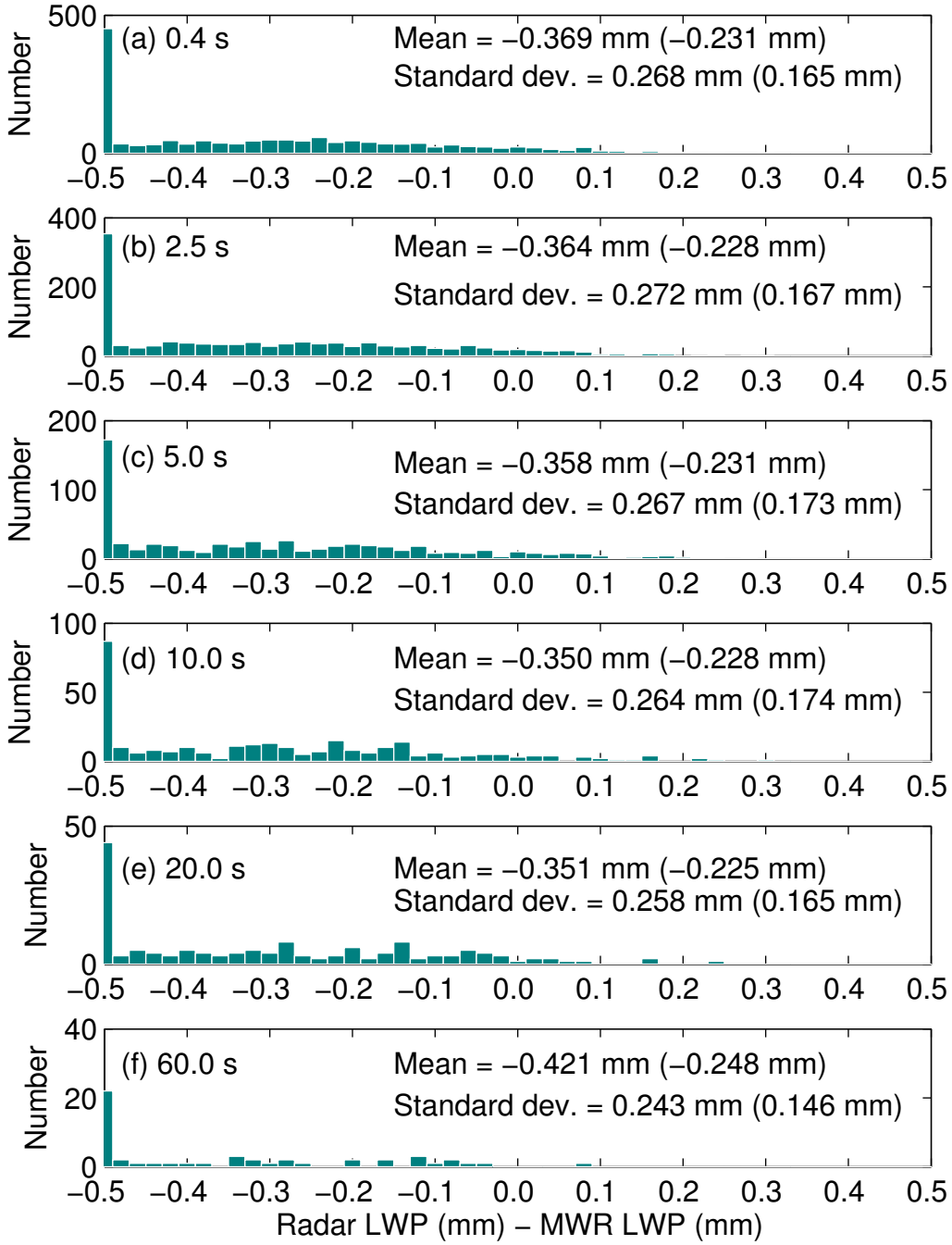

Figure A.12: Same as Fig. A.3 but for the SGP period from 13:00-17:00 UTC on 2 April 2013.

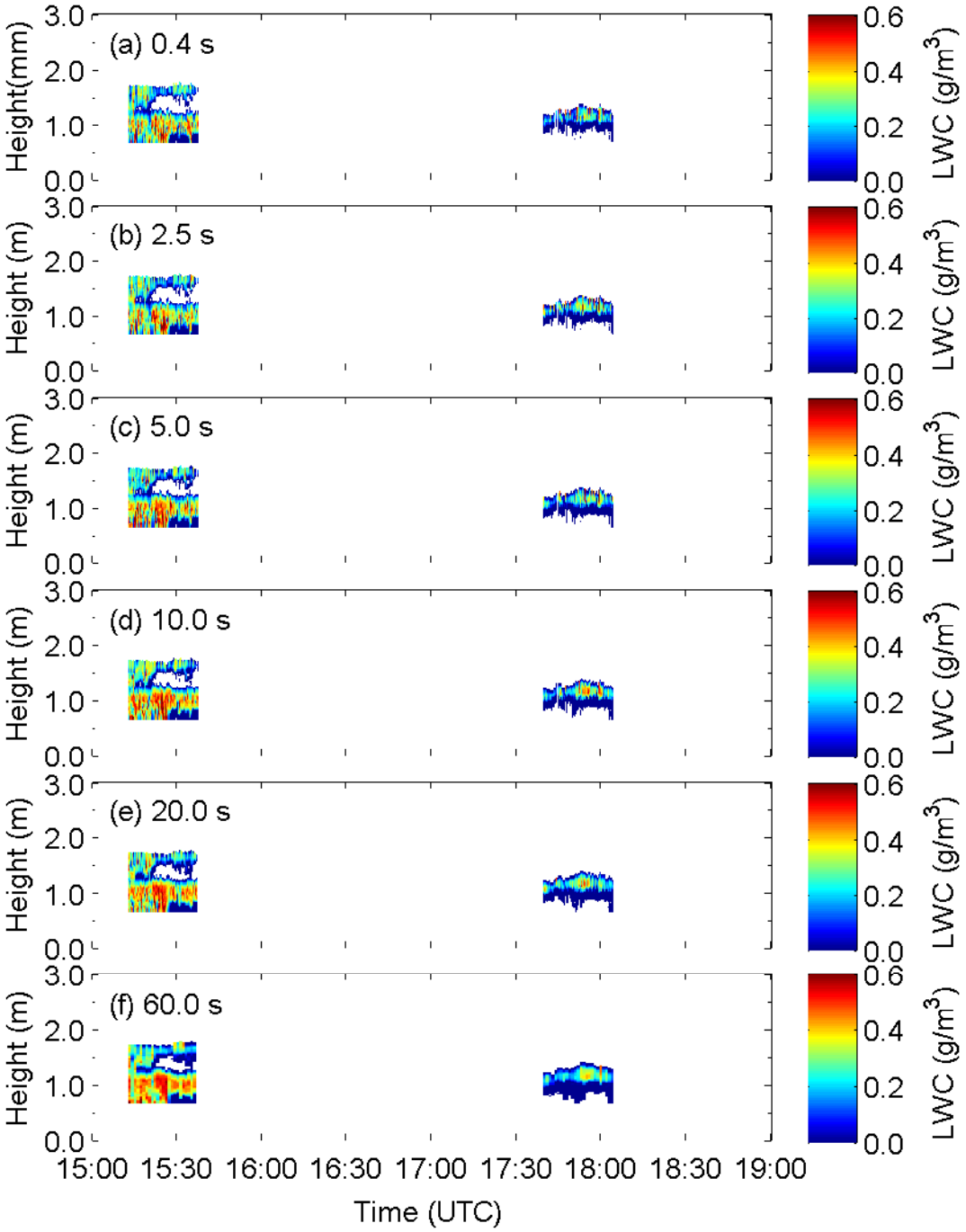

Figure A.13: Same as Fig. A.1 but for the SGP period from 15:00-19:00 UTC on 18 April 2013.

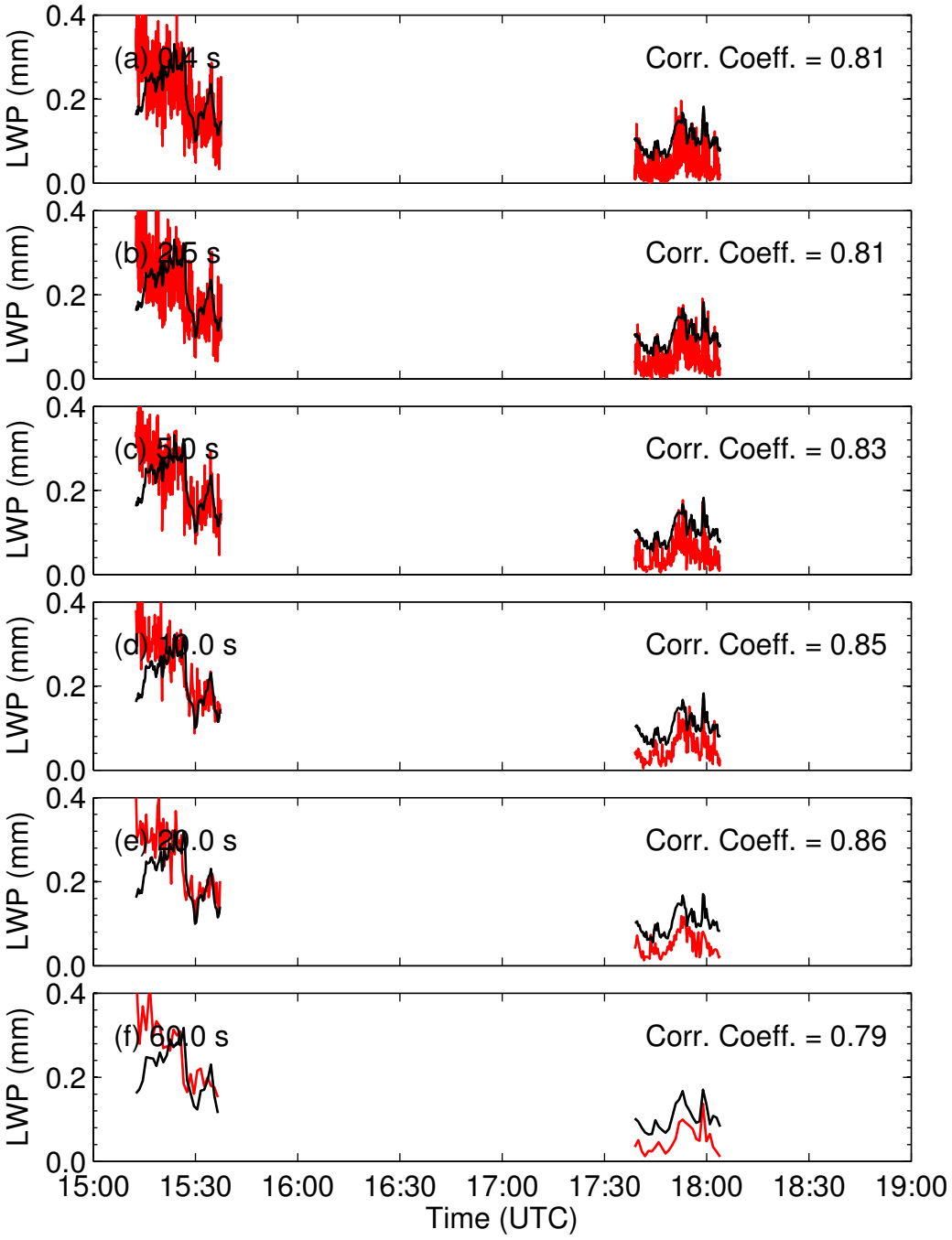

Figure A.14: Same as Fig. A.2 but for the SGP period from 15:00-19:00 UTC on 18 April 2013.

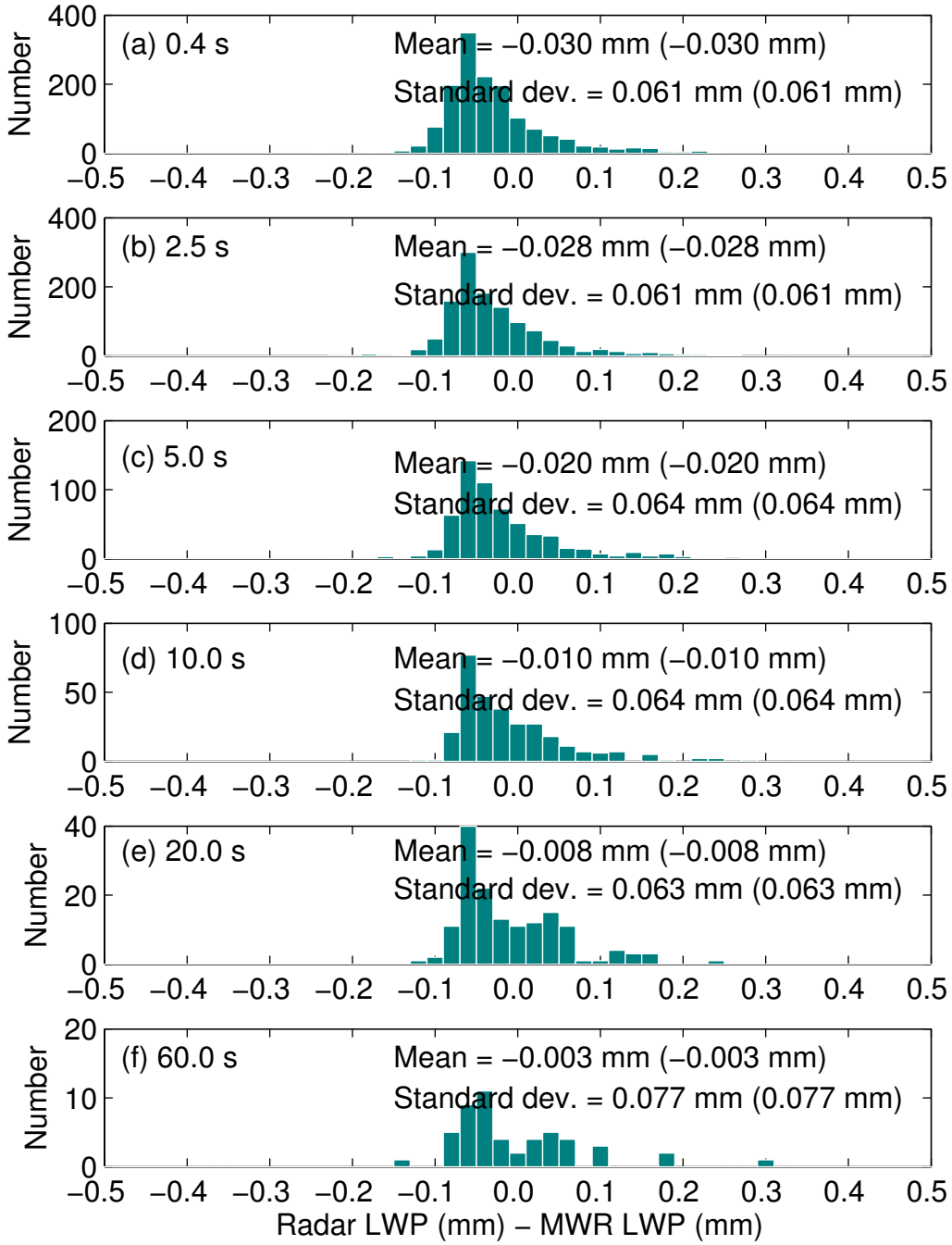

Figure A.15: Same as Fig. A.3 but for the SGP period from 15:00-19:00 UTC on 18 April 2013.

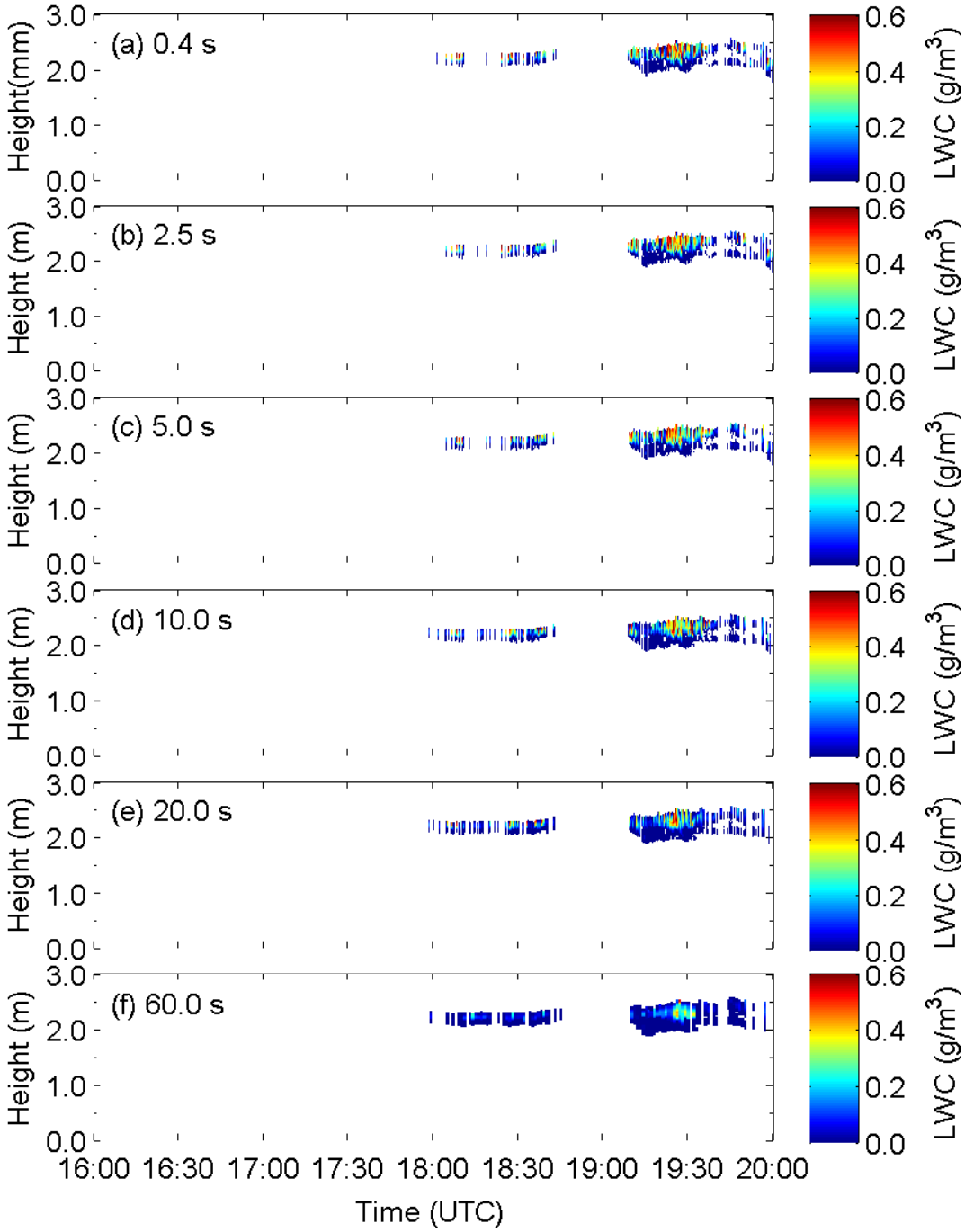

Figure A.16: Same as Fig. A.1 but for the NSA period from 16:00-20:00 UTC on 25 July 2012.

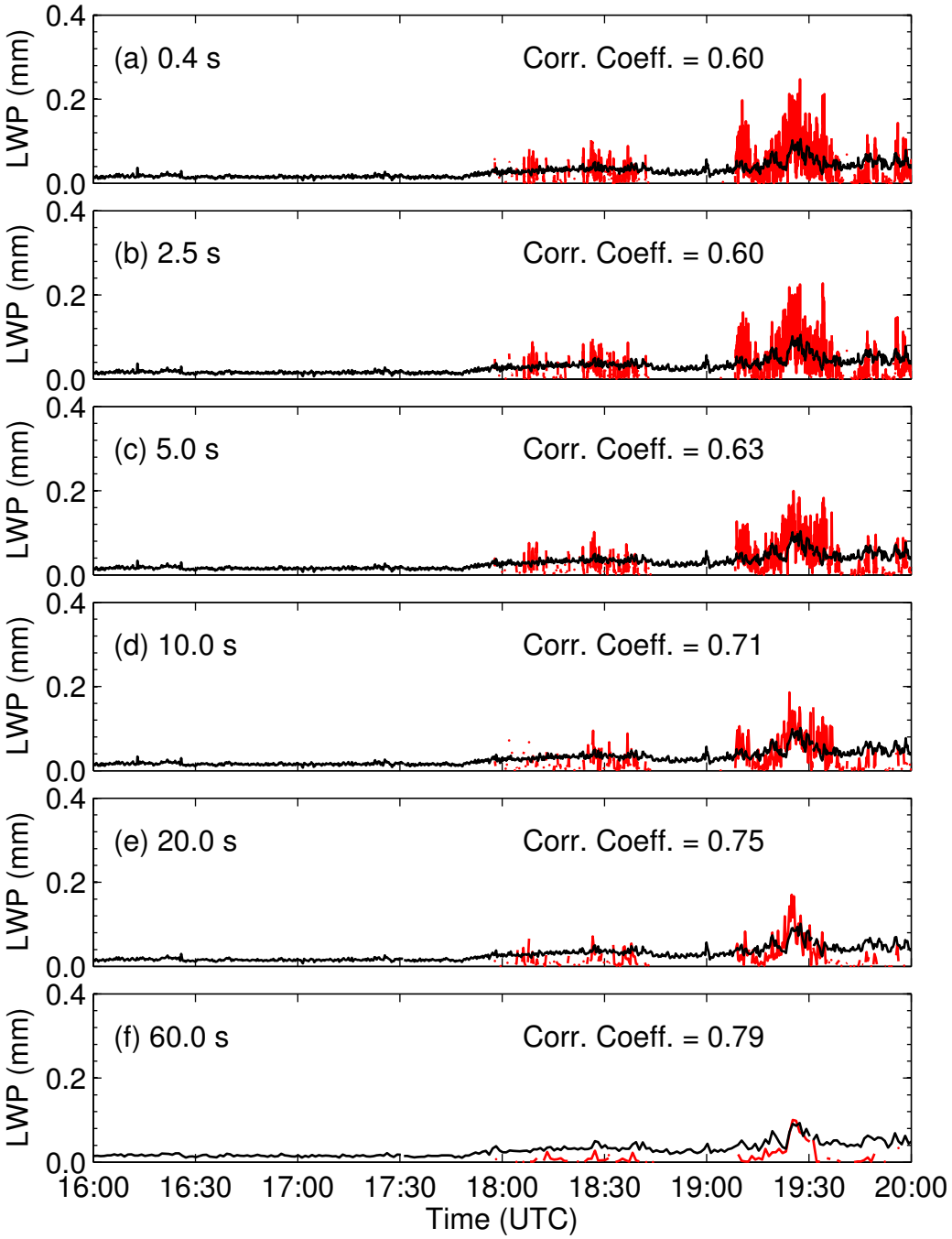

Figure A.17: Same as Fig. A.2 but for the NSA period from 16:00-20:00 UTC on 25 July 2012.

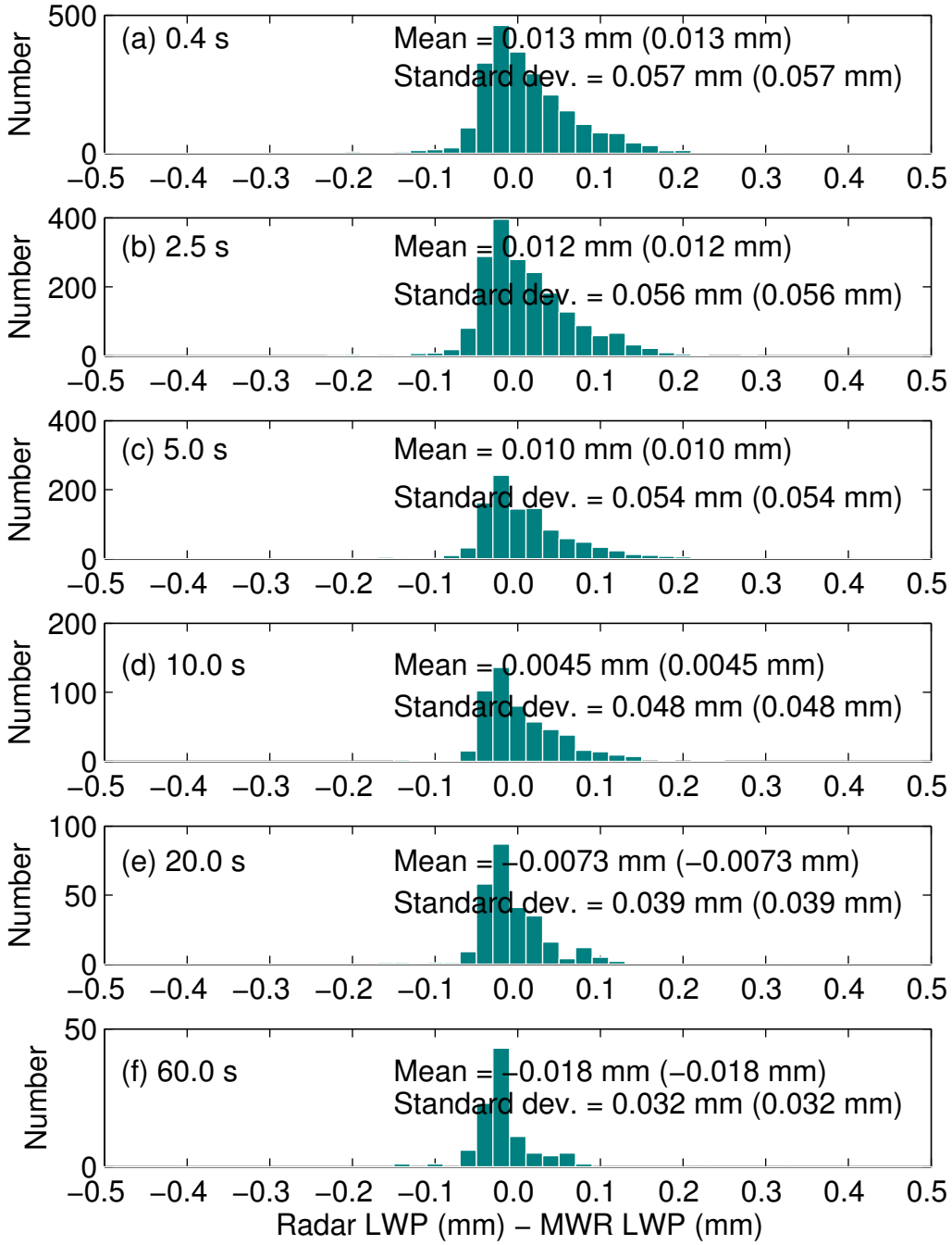

Figure A.18: Same as Fig. A.3 but for the NSA period from 16:00-20:00 UTC on 25 July 2012.

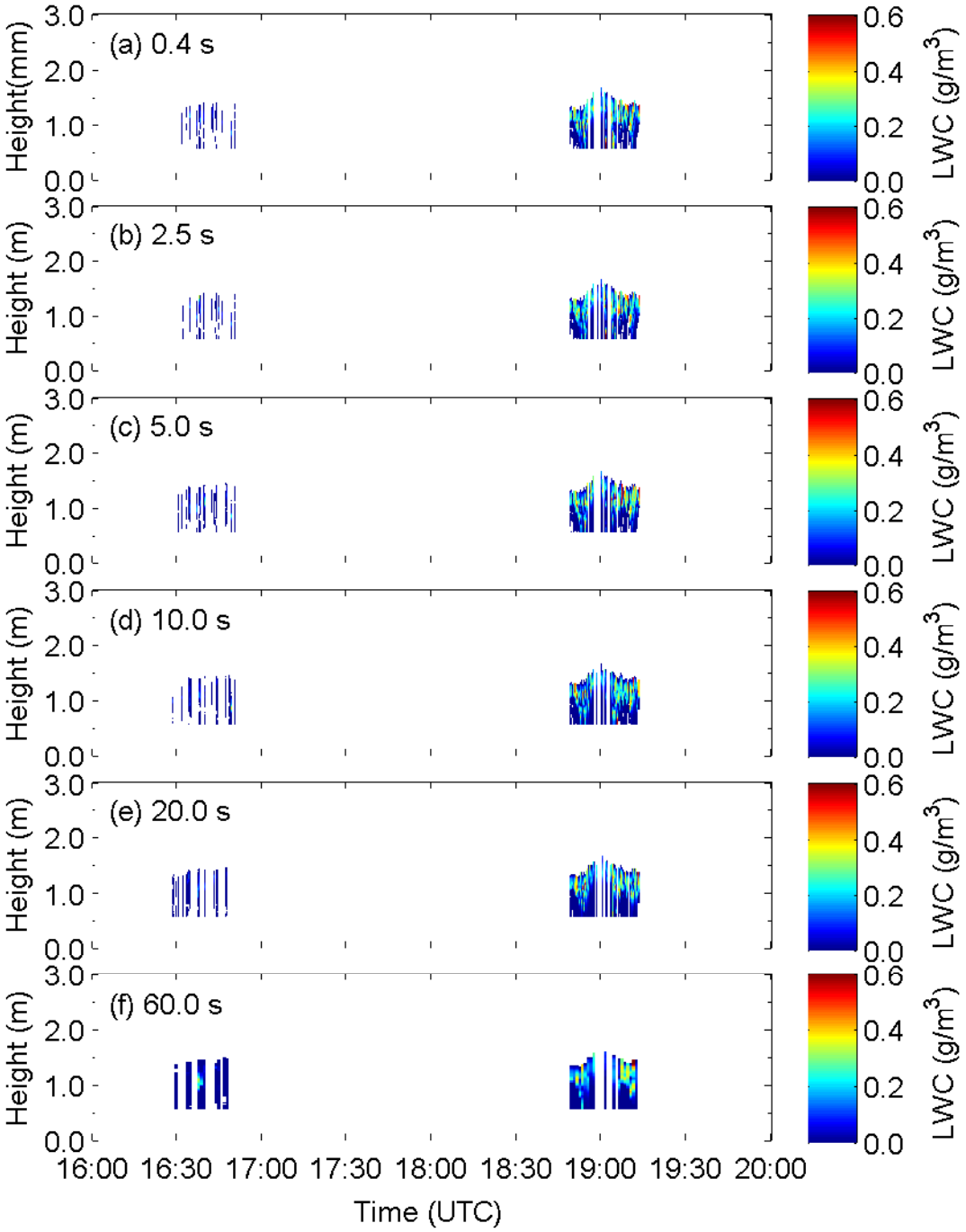

Figure A.19: Same as Fig. A.1 but for the NSA period from 16:00-20:00 UTC on 18 October 2012.

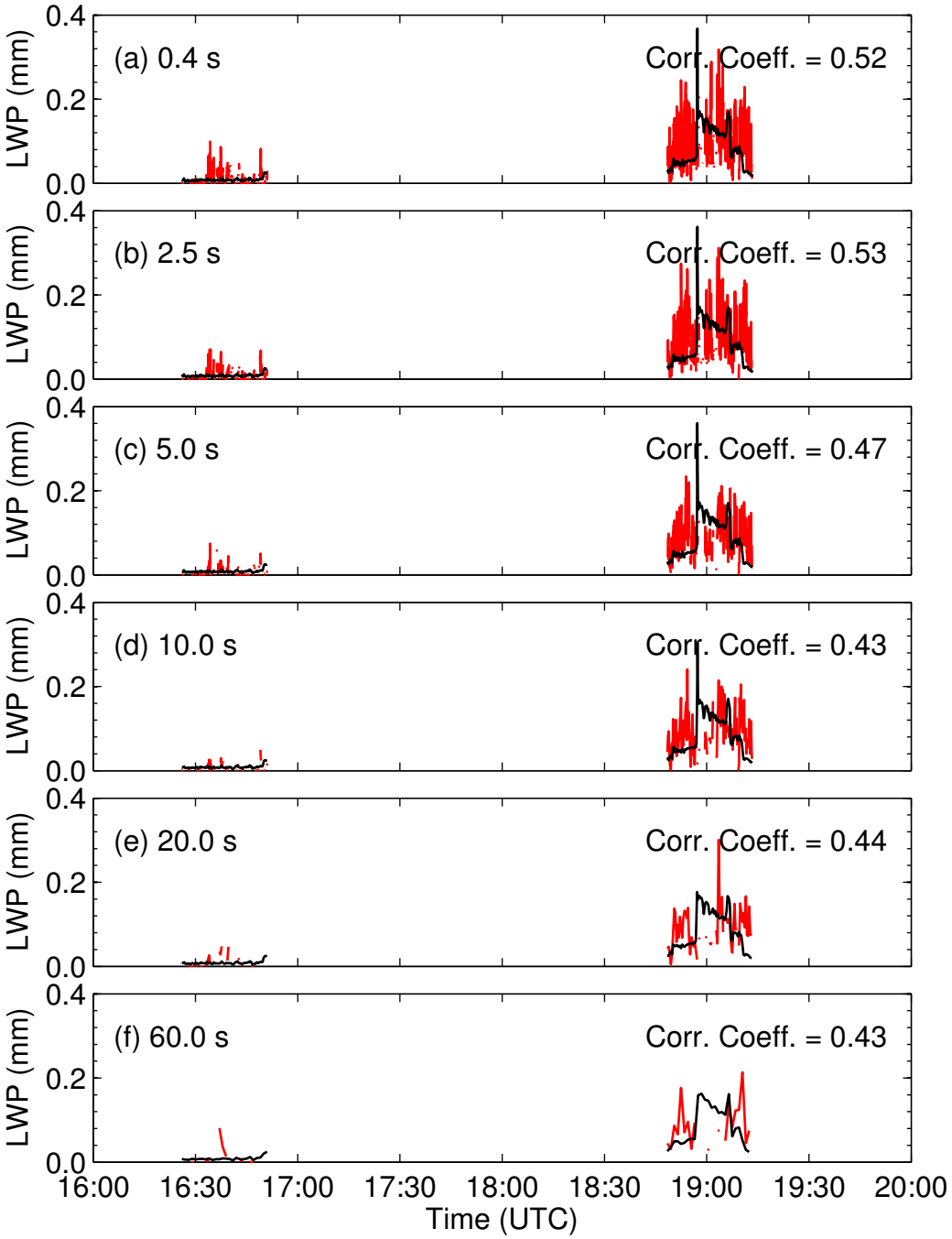

Figure A.20: Same as Fig. A.2 but for the NSA period from 16:00-20:00 UTC on 18 October 2012.

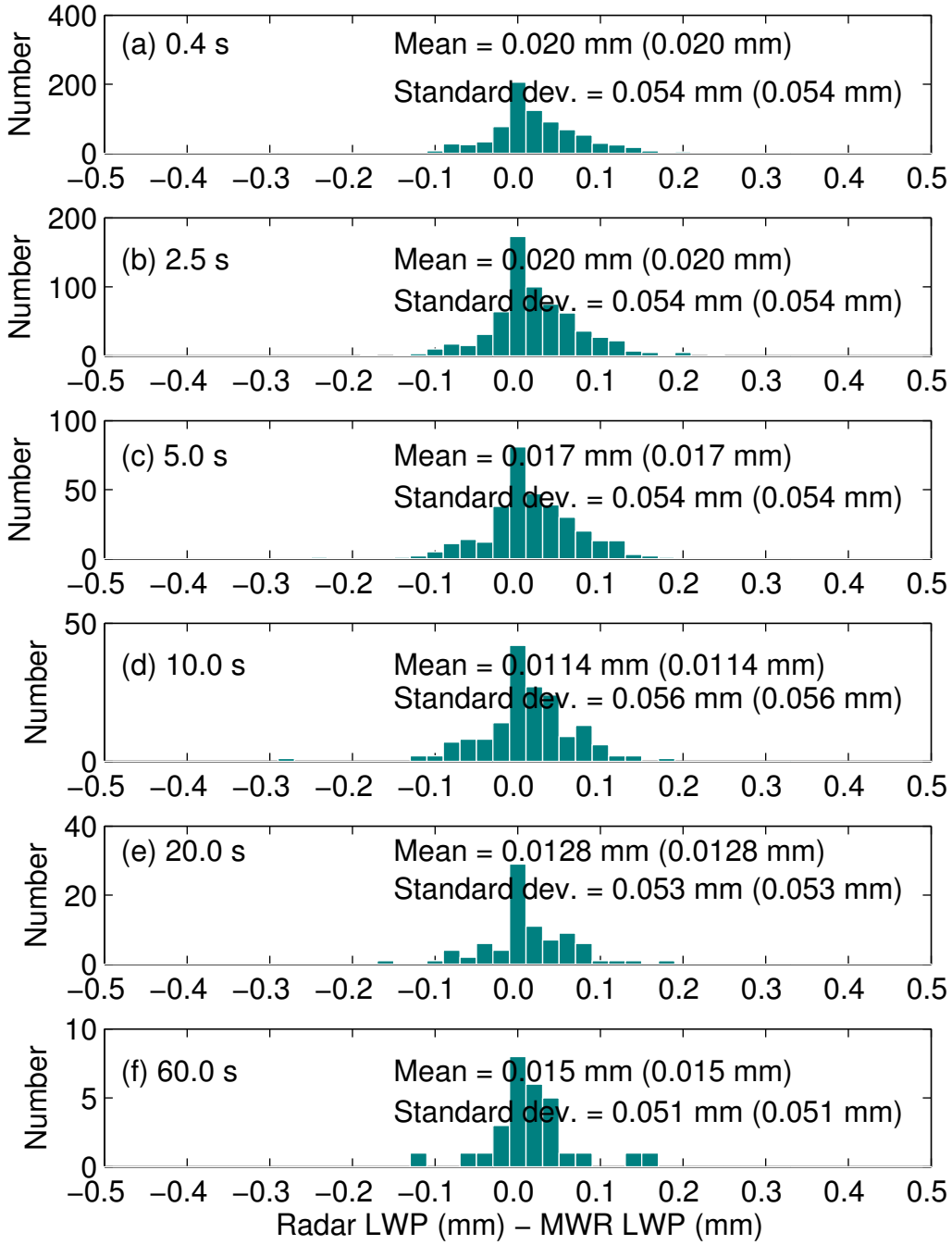

Figure A.21: Same as Fig. A.3 but for the NSA period from 16:00-20:00 UTC on 18 October 2012.

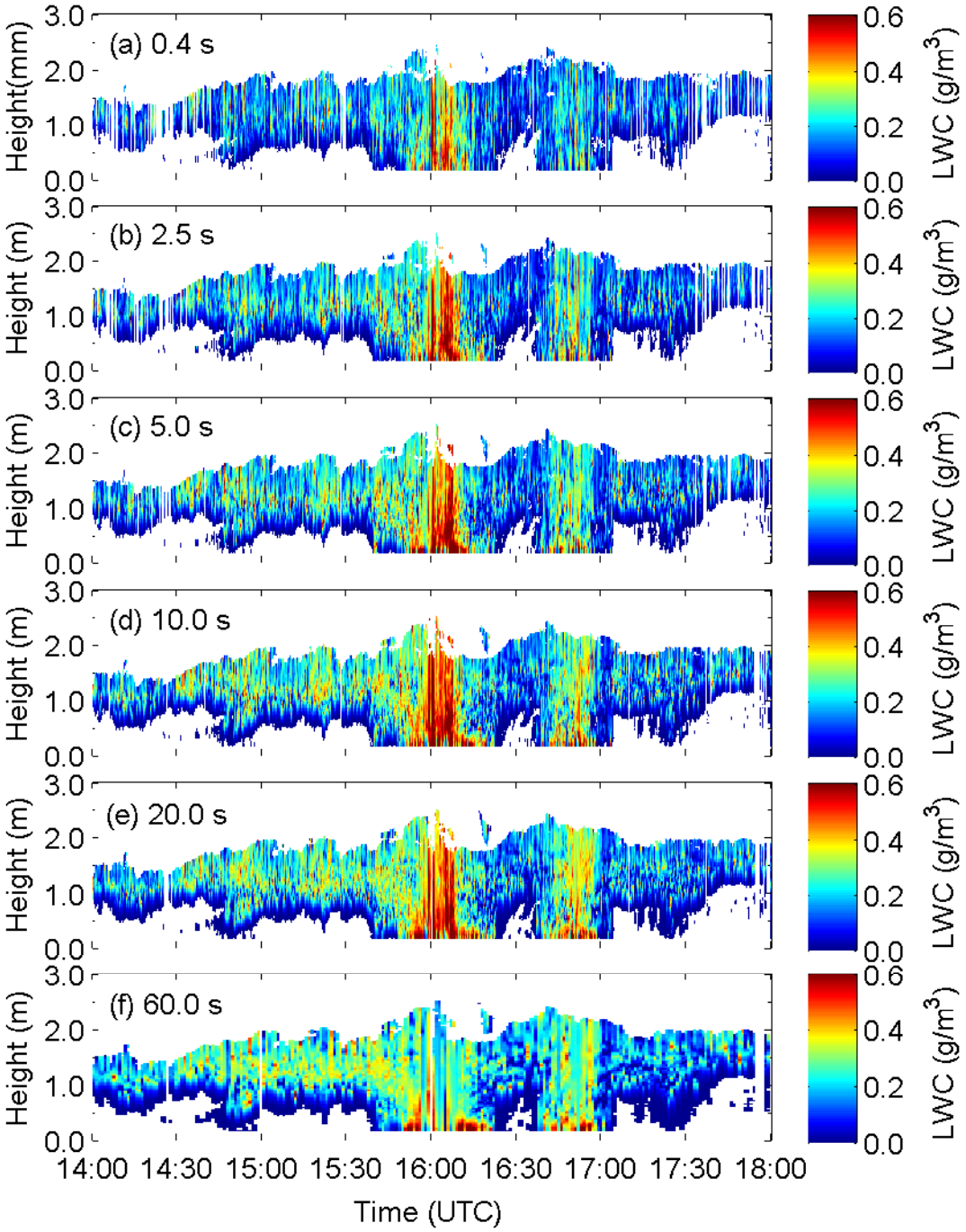

Figure A.22: Same as Fig. A.1 but for the MAGIC period from 14:00-18:00 UTC on 26 November 2012.

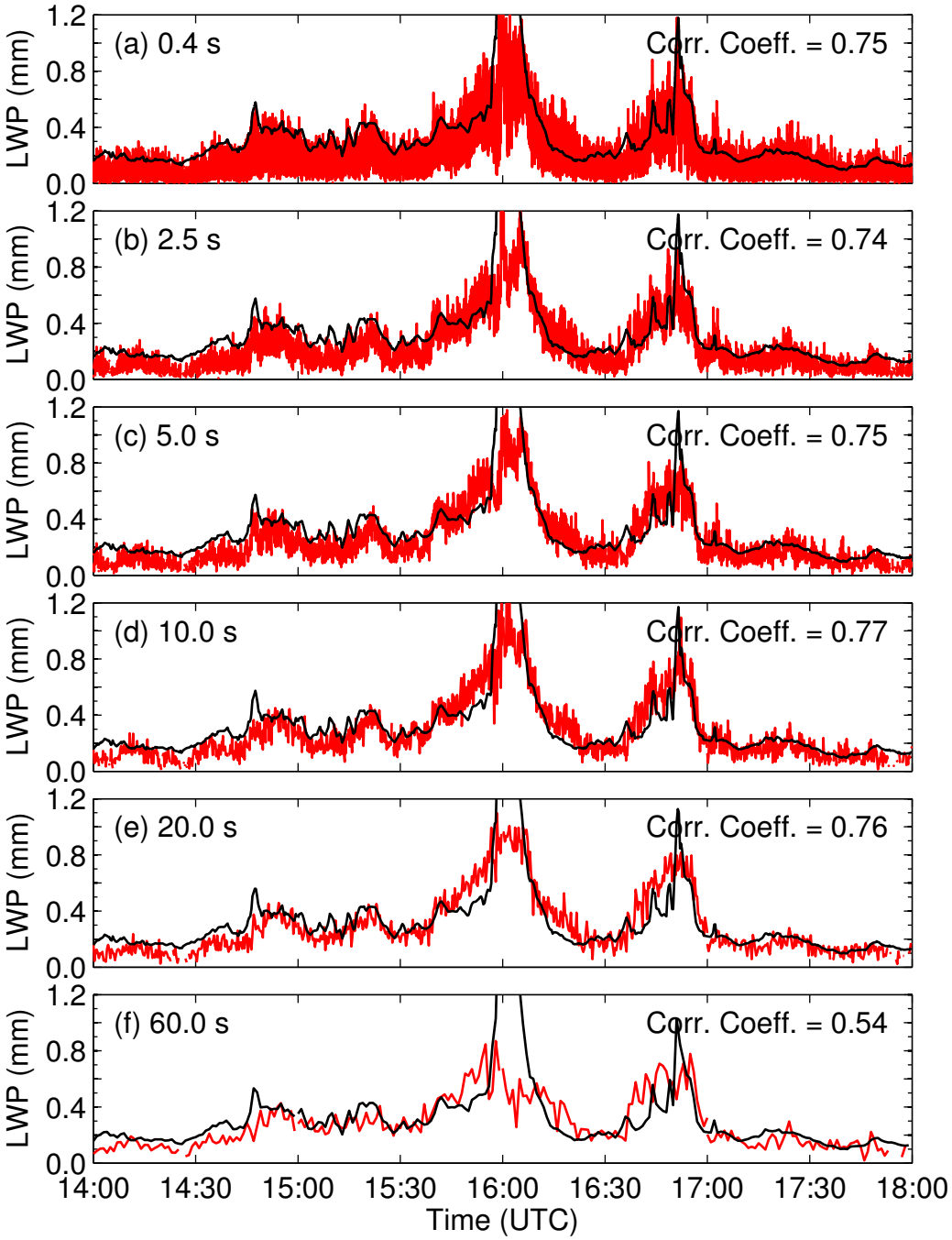

Figure A.23: Same as Fig. A.2 but for the MAGIC period from 14:00-18:00 UTC on 26 November 2012.

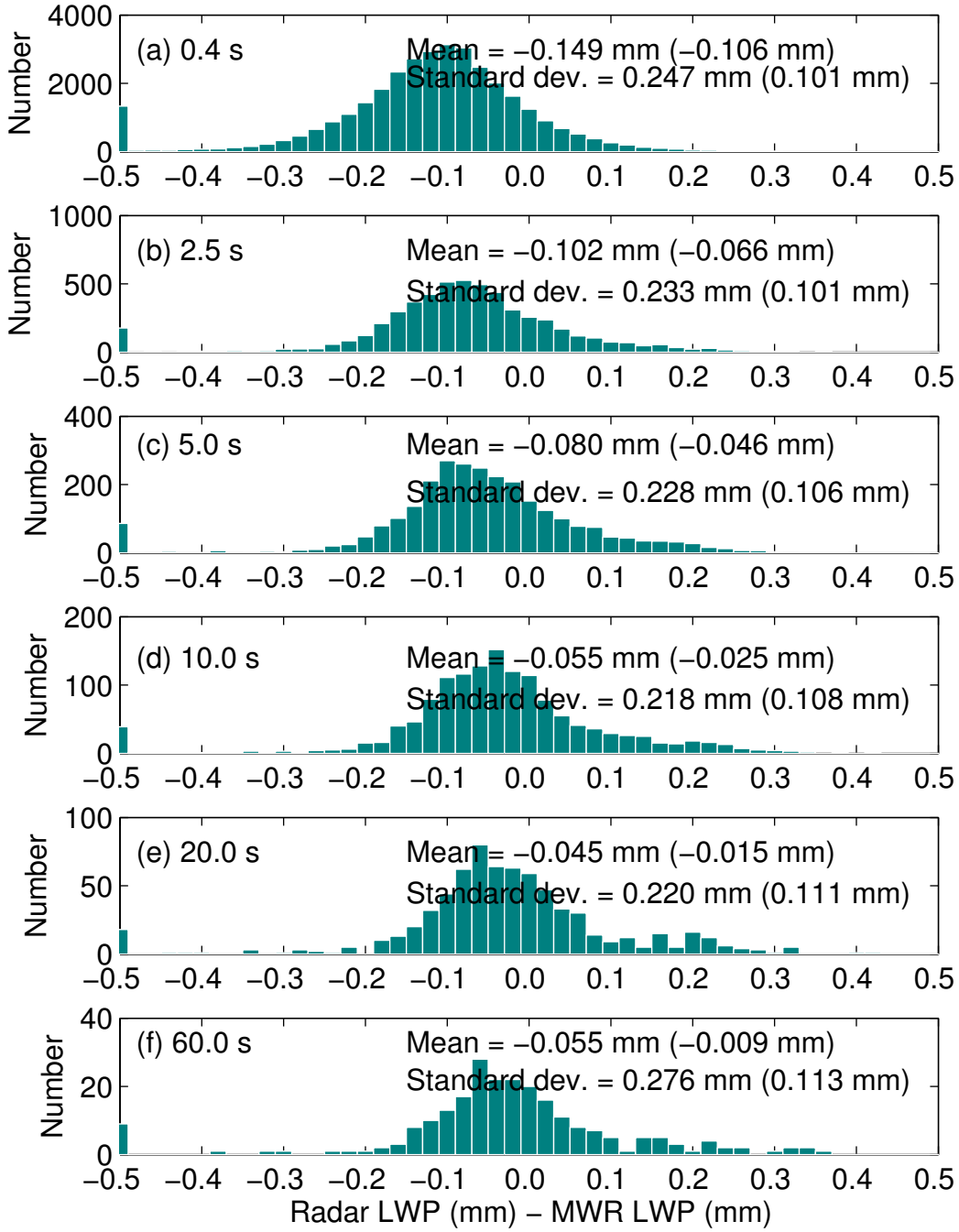

Figure A.24: Same as Fig. A.3 but for the MAGIC period from 14:00-18:00 UTC on 26 November 2012.

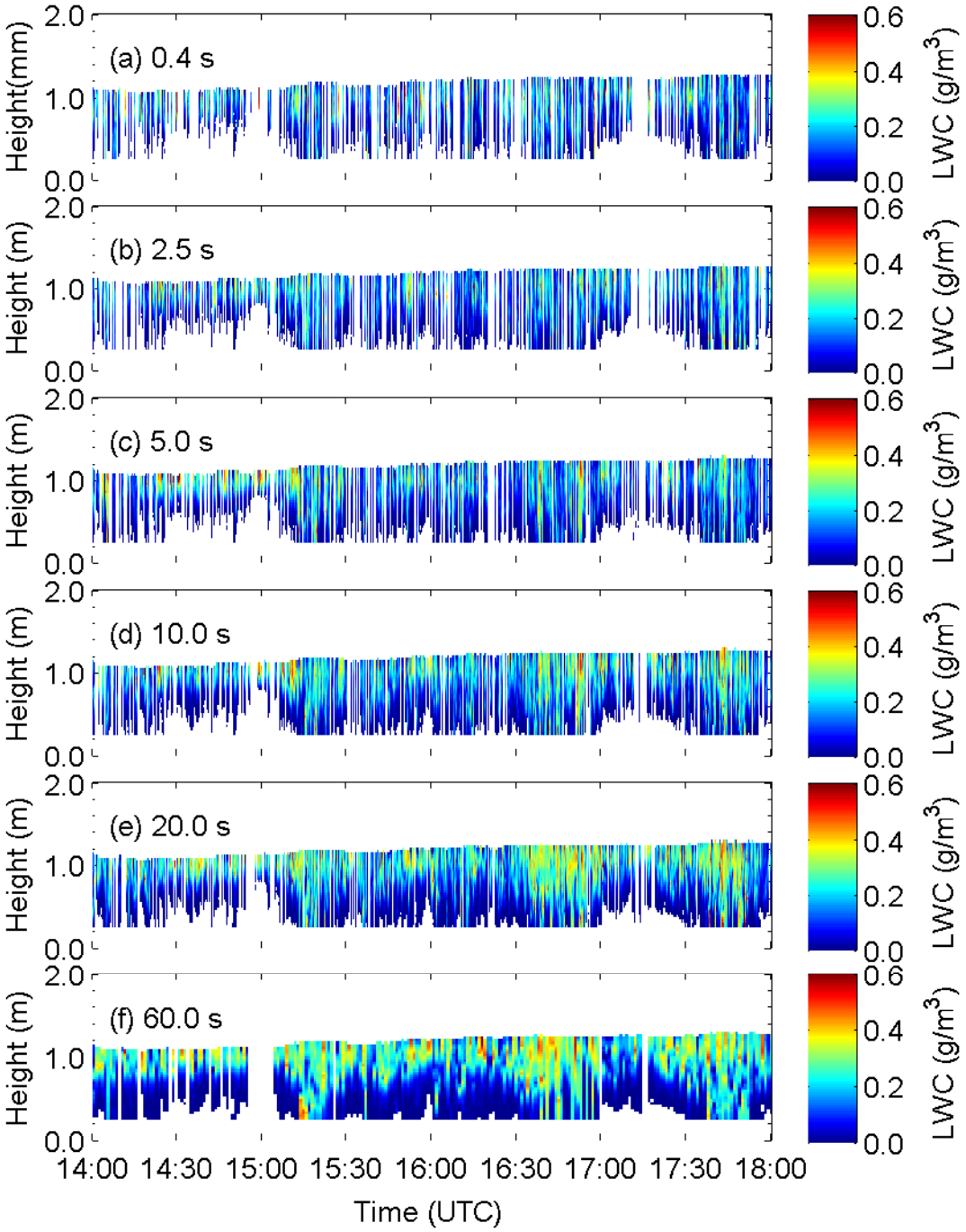

Figure A.25: Same as Fig. A.1 but for the MAGIC period from 14:00-18:00 UTC on 8 July 2013.

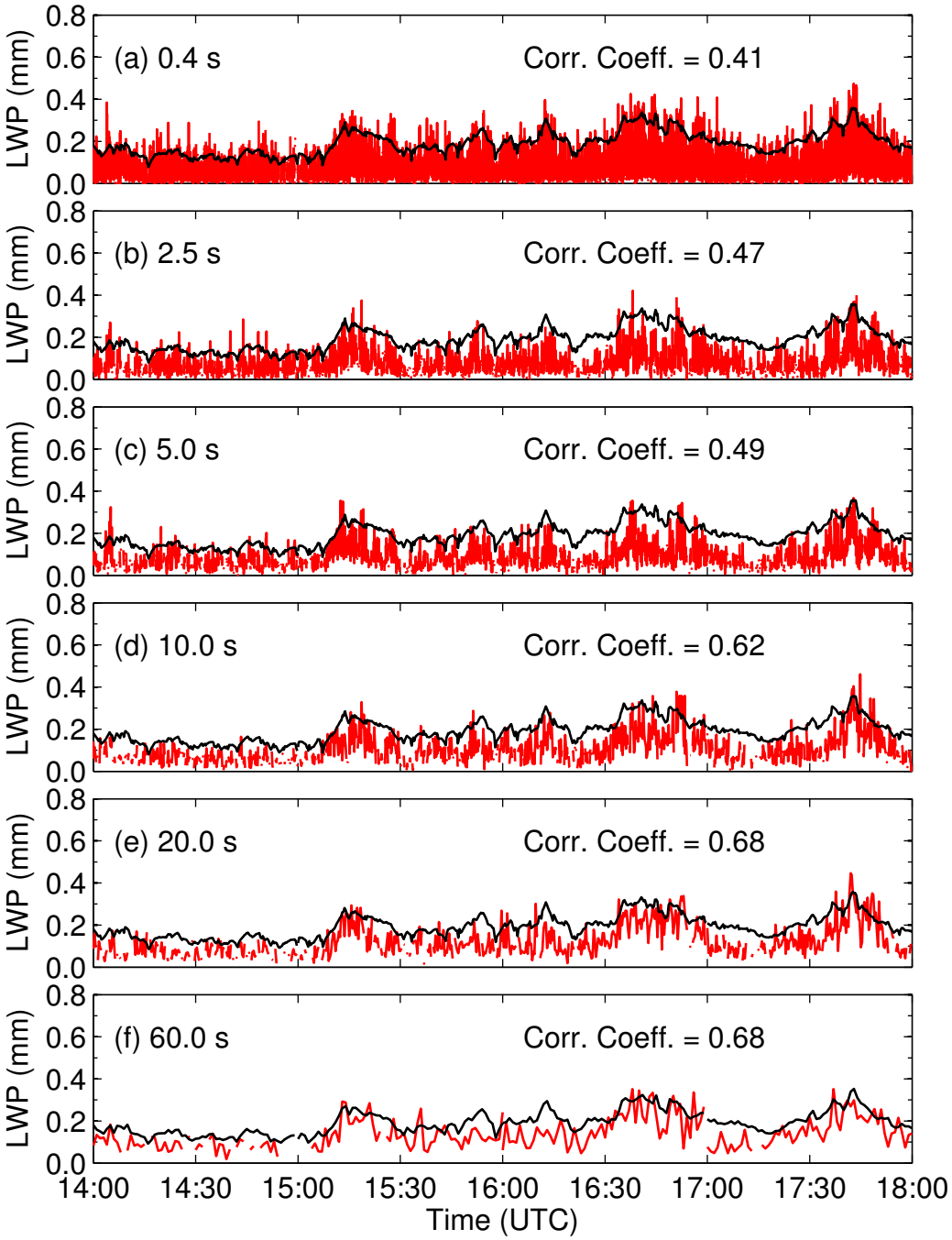

Figure A.26: Same as Fig. A.2 but for the MAGIC period from 14:00-18:00 UTC on 8 July 2013.

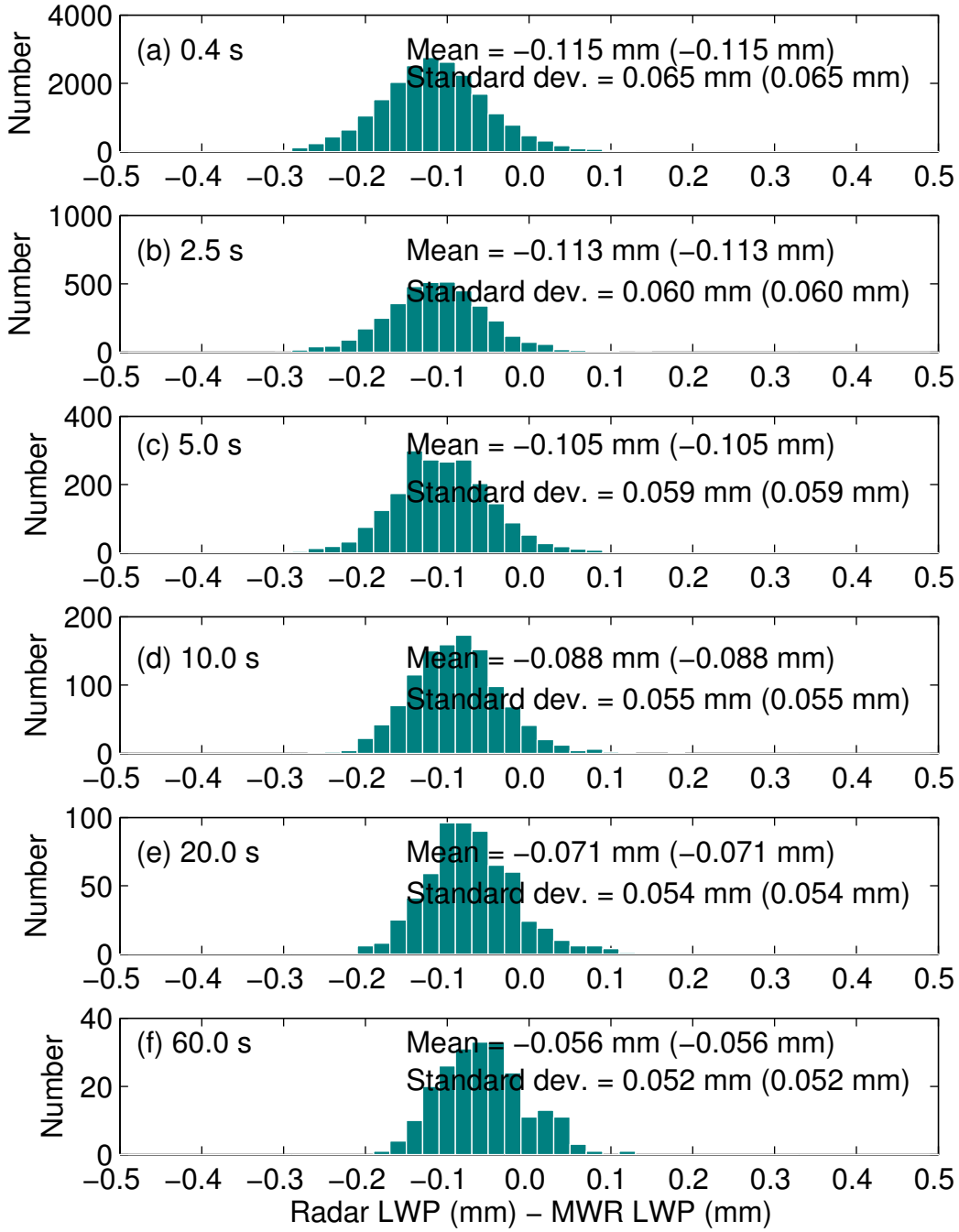

Figure A.27: Same as Fig. A.3 but for the MAGIC period from 14:00-18:00 UTC on 8 July 2013.

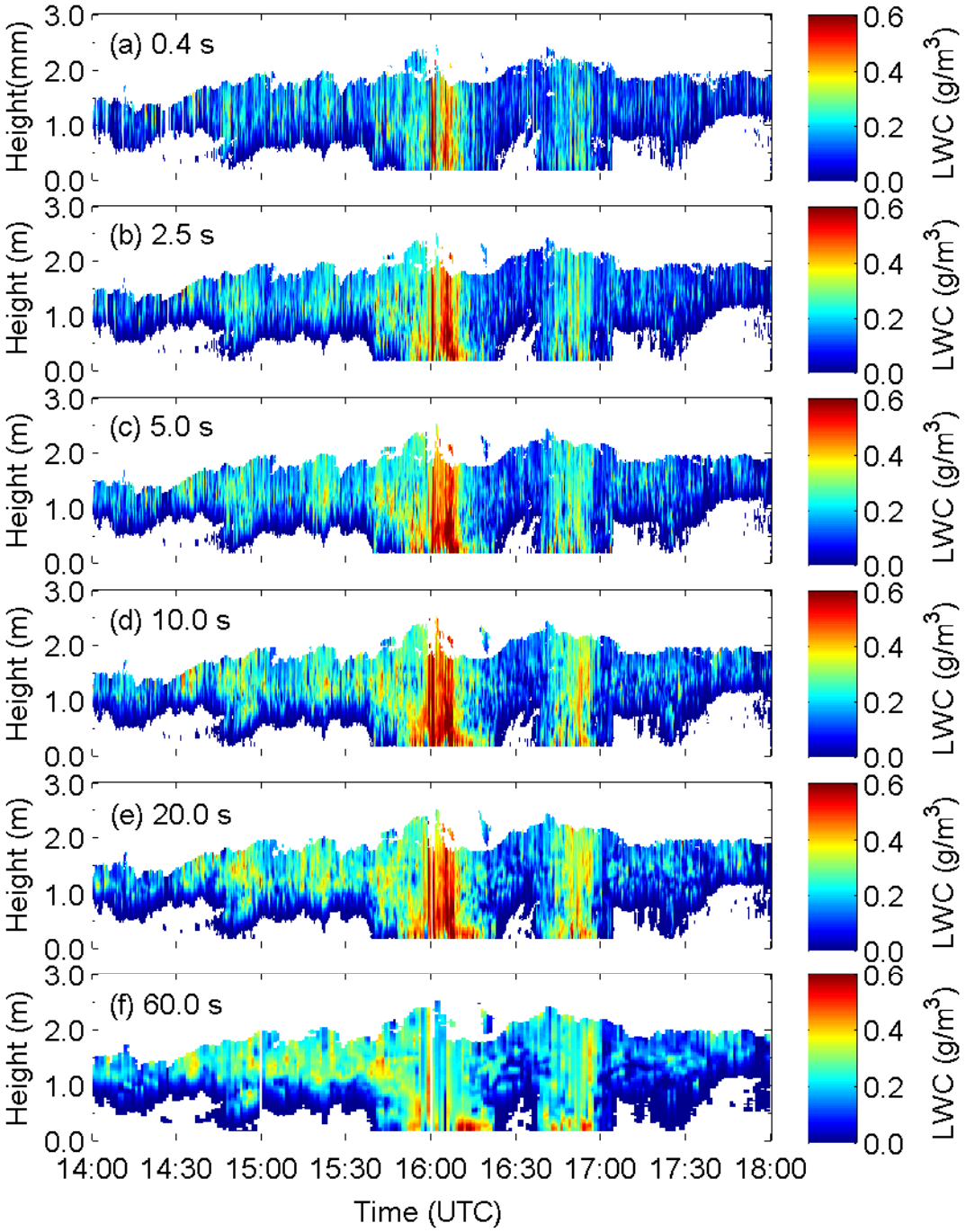

Figure A.28: Same as Fig. A.1 but for the MAGIC period from 14:00-18:00 UTC on 26 November 2012 with the application of spatial filtering to DFR data.

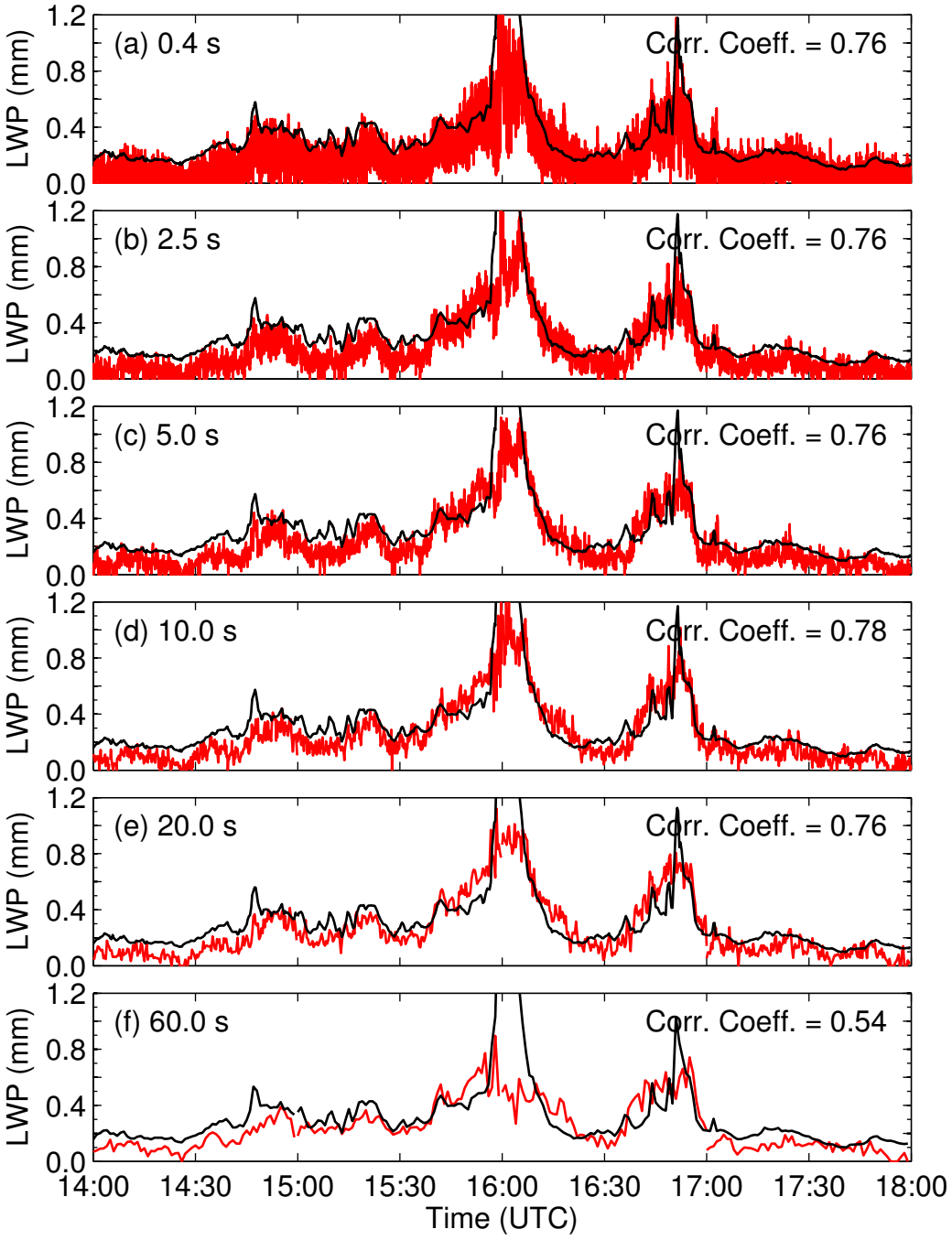

Figure A.29: Same as Fig. A.2 but for the MAGIC period from 14:00-18:00 UTC on 26 November 2012 with the application of spatial filtering to DFR data.

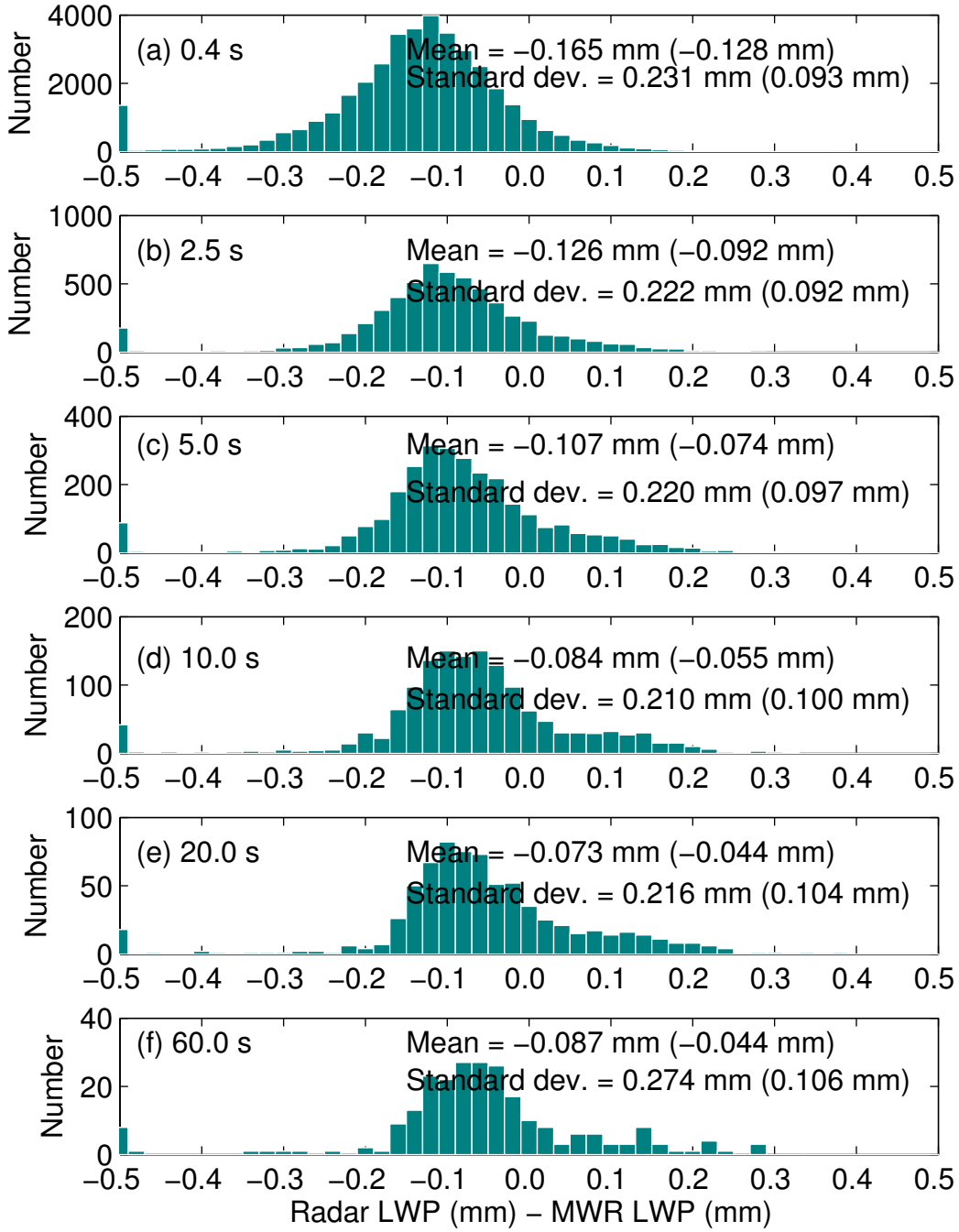

Figure A.30: Same as Fig. A.3 but for the MAGIC period from 14:00-18:00 UTC on 26 November 2012 with the application of spatial filtering to DFR data.

Bibliography

D. Atlas. The estimation of cloud parameters by radar. *Journal of Meteorology*, 11:309–317, 1954.

M. P. Cadeddu and D. D. Turner. Evaluation of water permittivity models from ground-based observations of cold clouds at frquencies between 23 and 170 ghz. *IEEE Transactions on Geoscience and Remote Sensing*, 49(8):2999–3008, August 2011.

M. P. Cadeddu, J. C. Liljegren, and A. L. Pazmany. Measurements and retrievals from a new 183-ghz water-vapor radiometer in the arctic. *IEEE Transactions on Geoscience and Remote Sensing*, 45(7):2207–2215, July 2007.

M. P. Cadeddu, J. C. Liljegren, and D. D. Turner. The atmospheric radiation measurement (arm) program network of microwave radiometers: instrumentation, data, and retrievals. *Atmospheric Measurement Techniques*, 6:2359–2372, 2013.

W. Ellison. *Thermal Microwave Radiation: Application for Remote Sensing*. Number 52 in Electromagnetic Waves. The institution of Engineering and Technology (IET), 2006.

A. S. Frisch, G. Feingold, C. W. Fairall, T. Uttal, and J. B. Snider. On cloud radar and microwave radiometer measurements of stratus cloud liquid water profiles. *Journal of Geophysical Research*, 103(D18):23195–23197, 1998.

R. Hogan, N. Gaussiat, and A. Illingworth. Stratocumulus liquid water content

from dual-wavelength radar. *Journal of Atmospheric and Ocean Technology*, 22: 1207–1218, 2005.

D. Huang, Y. Liu, and W. Wiscombe. Cloud tomography: Role of constraints and a new algorithm. *Journal of Geophysical Research*, 113:D23203, 2008a.

D. Huang, Y. Liu, and W. Wiscombe. Determination of cloud liquid water distribution using 3d cloud tomography. *Journal of Geophysical Research*, 113: D13201, 2008b.

D. Huang, K. Johnson, Y. Liu, and W. Wiscombe. High resolution retrieval of liquid water vertical distributions using collocated ka-band and w-band cloud radars. *Geophysical Research Letters*, 36, 2009.

C. L. Lawson and R. J. Hanson. *Solving Least Squares Problems*, page 337, 1974.

H. J. Liebe, G. A. Hufford, and T. Manabe. A model for the complex permittivity of water at the frequencies below 1 thz. *Int. J. Infrared Millim. Waves*, 12(7): 659–675, 1991.

H. J. Liebe, G. A. Hufford, and M. G. Cotton. Propagation modeling of moist air and suspended water/ice particles at frequencies below 1000 ghz. *Proc. AGARD*, 542:1–10, 1993.

J. C. Liljegren, E. E. Clothiaux, G. G. Mace, S. Kato, and X. Dong. A new retrieval for cloud liquid water path using a ground-based microwave radiometer and meausrements of cloud temperature. *Journal of Geophysical Research*, 106 (D13):14485–14500, 2001.

J. E. Pierce and B. W. Rust. *SIAM Journal of Statistical Computing*, 6:670–683, 1985.

P. W. Rosenkranz. Water vapor microwave continuum absorption: A comparison of measurements and models. *Radio Science*, 33(4):919–928, 1998.

S. M. Sekelsky. Multifrequency radar observation of liquid clouds. In *International Geoscience and Remote Sensing*, volume I–VI. IEEE 2000 International Geoscience and Remote Sensing (IGARS) Symposium, 2000.

S. M. Sekelsky and R. E. McIntosh. Cloud observations with a polarimetric 33 ghz and 95 ghz radar. *Meteorological Atmospheric Physics*, 59(123–140), 1996.

A. P. Strogryn, H. T. Bull, K. Rubayi, and S. Iranvanchy. The microwave permittivity of sea and fresh water. In *The microwave permittivity of sea and fresh water*, Aerojet Rep., Azusa, CA, 1995. GenCorp Aerojet.

A. N. Tikhonov. Solution of incorrectly formulated problems and the regularization method. *Solv. Math. Dorkl.*, 4:1035–1038, 1963.

D. D. Turner. Improved ground-based liquid water path retrievals using a combined infrared and microwave approach. *Journal of Geophysical Research*, 112 (D15204):1–15, 2007.

D. D. Turner, A. M. Vogelmann, R. T. Austin, J. C. Barnard, K. Cady-Pereira, J. C. Chui, S. A. Clough, C. Flynn, M. M Khaiyer, J. C. Liljegren, K. Johnson, B. Lin, C. Long, A marshak, S. A. McFarlane, M. Miller, Q. Min, P. Minnis, W. O'Hirok, Z. Wang, and W. Wiscombe. Thin liquid clouds: Their importance and our challenge. *Bulletin of the American Meteorological Society*, 88(2):117–190, Febuary 2007.

D. D. Turner, M. P. Cadeddu, U. Löhnert, S. Crewell, $Memberof\ IEEE$, and A. M. Vogelmann. *IEEE Transactions on Geoscience and Remote Sensing*, 47 (10):3326–3337, 2009.